UNIVERSITÀ DEGLI STUDI DI NAPOLI
"FEDERICO II"

Scuola Politecnica e delle Scienze di Base

Area Didattica di Scienze Matematiche Fisiche e Naturali

Dipartimento di Fisica "Ettore Pancini"

Laurea Magistrale in Fisica

Study of neutrino interactions at SND@LHC

Relatori:
Prof. Giovanni De Lellis
Prof.ssa Antonia Di Crescenzo
Dott. Antonio Iuliano

Candidato:
Fabio Alicante
Matr. $N94000696$

Anno Accademico 2021/2022

CERN-THESIS-2023-206
22/05/2023

Contents

Introduction

SND@LHC (Scattering and Neutrino Detector at the LHC) is a compact and stand-alone experiment, designed to perform measurements with high energy neutrinos produced at the LHC (CERN) in an unexplored pseudo-rapidity region of $7.2 < \eta < 8.4$, complementary to all the other experiments at the LHC. The experiment is located $480\,\mathrm{m}$ downstream of the ATLAS interaction point, in the unused TI18 tunnel. The detector is composed of a hybrid system based on a $830\,\mathrm{kg}$ target mass of tungsten plates, interleaved with nuclear emulsion and electronic trackers, also acting as an electromagnetic calorimeter, followed downstream by an hadronic calorimeter and a muon identification system. Such configuration allows all three neutrino flavours to be efficiently distinguished, thus opening a unique opportunity to probe physics of heavy flavour production at the LHC in a pseudo-rapidity region which is not accessible to the current LHC detectors.

This region is of particular interest also for future circular colliders and for predictions of very high-energy atmospheric neutrinos. Moreover, the operation of the detector will provide an important test of neutrino reconstruction in a high occupancy environment in view of a possible experiment at HL-LHC (High Luminosity LHC). In addition, the detector design also makes SND@LHC sensitive to Feebly Interacting Particles (FIPs) by means of scattering off atoms in the detector target. The direct-search strategy gives the experiment sensitivity in a region of the FIPs mass-coupling parameter space that is complementary to other indirect searches. SND@LHC was installed in TI18 in 2021 during the Long Shutdown 2 and it has seen its first data in July 2022. In the first phase the experiment plans to operate the detector throughout LHC Run 3, in order to collect a total integrated luminosity of about $250\,\mathrm{fb}^{-1}$ in 2022-25. The experiment has been taking data successfully during the proton physics run of 2022.

The primary focus of this thesis is the reconstruction and the analysis of emulsion data acquired at the beginning of LHC Run 3. The whole emulsion reconstruction procedure will be described in-depth to provide a complete understanding of each step. Notably, the analysis concerns the study of the tracks

and vertices reconstructed in the very first emulsion target exposure. The ultimate objective aims to match data from both nuclear emulsions and electronic detectors so as to reconstruct and identify the neutrino interactions. After the performance evaluation of such procedure based on Monte Carlo simulation, the algorithms will be applied to the Run3 real data in the near future.

I have widely attempted at the scanning operations in the Naples University microscopy laboratory, and I have been personally involved in the first emulsion data reconstruction. Furthermore, I had the extraordinary opportunity to complete my thesis work at CERN, the European Organization for Nuclear Research, one of the world's largest and most respected centres for scientific research. This allowed me to take part in the whole procedure of data taking, such as the emulsion assembly and installation in the detector, besides proving myself to be self-reliant in handling the scanning station's procedures. Moreover, I have worked in contact with experts, thus learning many aspects of the detector and the data analysis that were important for my work.

The main physics goals of SND@LHC experiment are presented in Chapter 1; Chapter 2 gives an overview of the detector design and performance; the designing and the beautifying of the two-dimensional event display of the experiment is described in Chapter 3; emulsion data reconstruction is addressed in Chapter 4; Chapter 5 focuses on vertex reconstruction and background suppression with a MVA approach; the first attempt to match emulsion and electronic data with Monte Carlo samples is reported in Chapter 6.

Chapter 1

Physics motivation

The SND@LHC experiment, proposed in August 2020 by the SND@LHC Collaboration [57], aims to conduct, together with the FASERν experiment [53], the first measurements of high-energy neutrinos produced at particle colliders. SND@LHC is designed to investigate leptonic universality in the neutrino sector and probe heavy flavour physics at the LHC in the very forward region, where a significant fraction of neutrinos originate from charmed-hadron decays. The data taking started in July 2022 and in the first phase the experiment plans to operate the detector throughout LHC Run 3 and measure the $pp \to \nu X$ cross-section in the $7.2 < \eta < 8.4$ range for all three neutrino flavours, collecting a total integrated luminosity of $250\,\mathrm{fb}^{-1}$ in 2022-25. The off-axis location is well-suited to exploring heavy-quark production in a pseudo-rapidity range that current LHC experiments cannot reach. On the longer term, the collaboration foresees to continue detector R&D on an advanced version of the SND@LHC detector for the HL-LHC (High Luminosity LHC).

Neutrinos are unique exploratory tools in particle physics. They only couple to other particles through the weak interaction, which is well determined in the Standard Model (SM) of particle physics. For this reason, neutrino scattering measurements can be used as a probe to measure many of the SM parameters [6, 11, 26] or to look beyond the SM for indications of new physics [36, 55]. Additionally, astrophysical neutrinos provide unique insights into the most energetic non-thermal sources in the Universe [46], not accessible through the observation of other messengers. Despite observations of cosmic rays, which reach energies that are ten million times higher than those achievable in the Large Hadron Collider, observations of γ-rays and astrophysical neutrinos, we do not yet know where or how these particles are accelerated. Neutrino astronomy is a key to discover how particles are accelerated to these extreme energies. Due to their low cross sections, neutrinos can escape dense astrophysical environments that are opaque to photons. Their special propagation properties make them a

penetrating probe into the far structure of the Universe and a precious instrument to peek into the dark sectors of the cosmos. In contrast to γ-rays, neutrinos travel almost unimpeded through the Universe, allowing direct observation of their sources. Unlike cosmic rays, neutrinos are not deflected in magnetic fields and can be observed in spatial and temporal coincidence with photons and gravitational waves, which is a key prerequisite to reap the scientific rewards of multi-messenger astronomy. In addition, neutrinos come in different flavors — electron, muon, and tau neutrinos (ν_e, ν_μ, ν_τ) — and the flavor ratios observed at Earth give insight into the environment of cosmic-ray sources.

Over the past few decades, neutrino interactions have mostly been measured in the energy regime below 350 GeV for neutrino oscillation studies. Recently, however, the IceCube collaboration reported detecting a few tens of events in the energy range of 10 TeV - 1 PeV [43]. Nonetheless, as shown in Figure 1.1, the region between 350 GeV and 10 TeV remains unexplored [50].

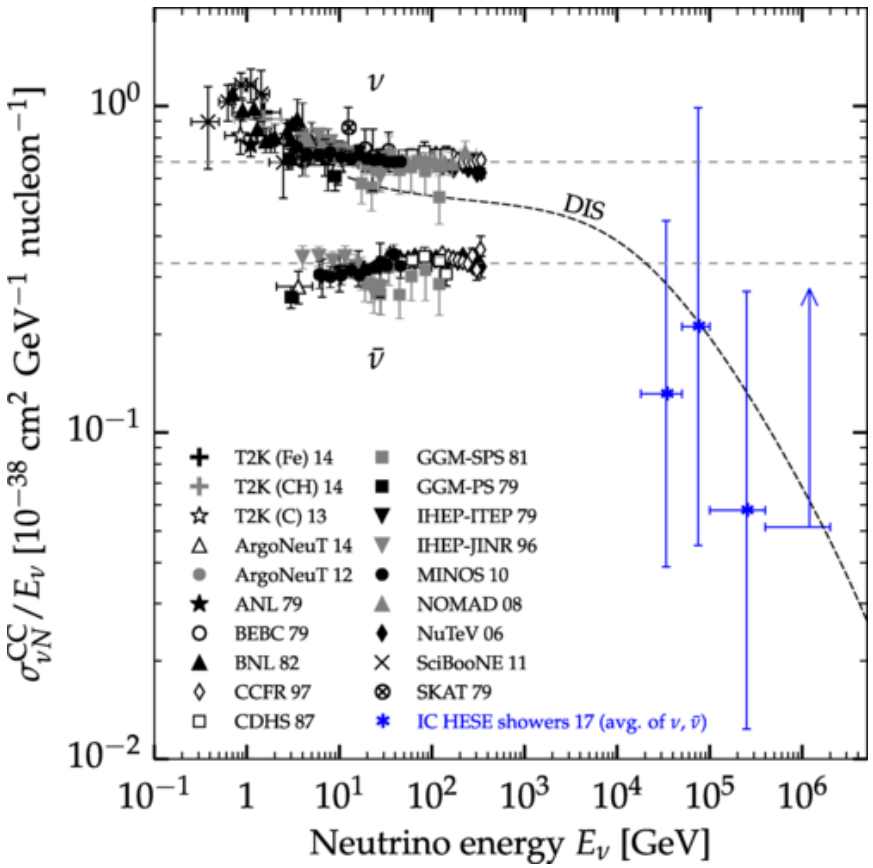

Figure 1.1: Available measurements of the neutrino cross-section [50]. The thick dashed curve shows the predicted rate of Deep Inelastic Scattering interactions.

LHC neutrinos provide a unique opportunity to observe neutrino interactions in the unexplored energy range of a few hundred GeV to a few TeV in a laboratory. Additionally, the τ flavour contributes significantly to the LHC neutrino flux. The idea of using the LHC as a neutrino factory was first considered about 30 years ago [1, 4, 5], also for the then undiscovered ν_τ. Today, the high intensity of proton-proton collisions at the LHC results in a large neutrino flux in the forward direction, and the high neutrino energies lead to relatively large neutrino cross-sections. Consequently, there has been great interest in placing a compact neutrino detector in one of the existing underground areas near the LHC tunnel [58], which promises significant physics potential. After evaluating various factors, such as expected neutrino rates, flavour composition, energy spectrum, predicted backgrounds, and in-situ measurements using a nuclear emulsion detector and radiation monitors [49], TI18 emerged as the most favourable location for the detector. Assuming a luminosity of $250\,\mathrm{fb}^{-1}$ in LHC Run 3, a detector with a mass of 830 kg located in TI18 could observe and study approximately two thousand high-energy neutrino interactions [49].

Neutrinos at the LHC are produced in proton-proton interactions through prompt leptonic W and Z decays, b and c decays, and subsequent decays of pions and kaons [61]. Tau neutrinos and anti-neutrinos are exclusively produced from heavy-hadron decays, while ν_es and $\bar{\nu}_e$s mostly come from charmed hadron decays, with a small contamination from kaons at low energies where the interaction cross-section with the detector is lower. Muon neutrinos and anti-neutrinos have a significant contribution from pion and kaon decays. In the explored η range, ν_μs from π and K decays have a softer energy spectrum, which allows distinguishing between the components from charm and π/K decays through the neutrino-energy measurement. Figure 1.2 illustrates the flux of different neutrino and anti-neutrino types in the (η, E_ν) plane. The main objectives of SND@LHC in the analysis of neutrinos during LHC Run 3 are summarised in the following sections.

1.1 Charmed-hadron production in pp collisions

Figure 1.3 displays the energy spectra of incoming neutrinos and anti-neutrinos in the pseudo-rapidity range from 7.2 to 8.4, which is covered by the SND@LHC detector, normalised to $250\,\mathrm{fb}^{-1}$. Approximately 1700 charged-current (CC) and 550 neutral current (NC) neutrino interactions are expected in the target volume, mainly predominantly muon neutrinos (72 %) and electron neutrinos (23 %) [61]. Electron neutrinos and anti-neutrinos interacting in SND@LHC mostly originate from the decay of charmed hadrons produced in the pp collisions at the LHC. The measurement of their flux in the experiment's acceptance can therefore offer

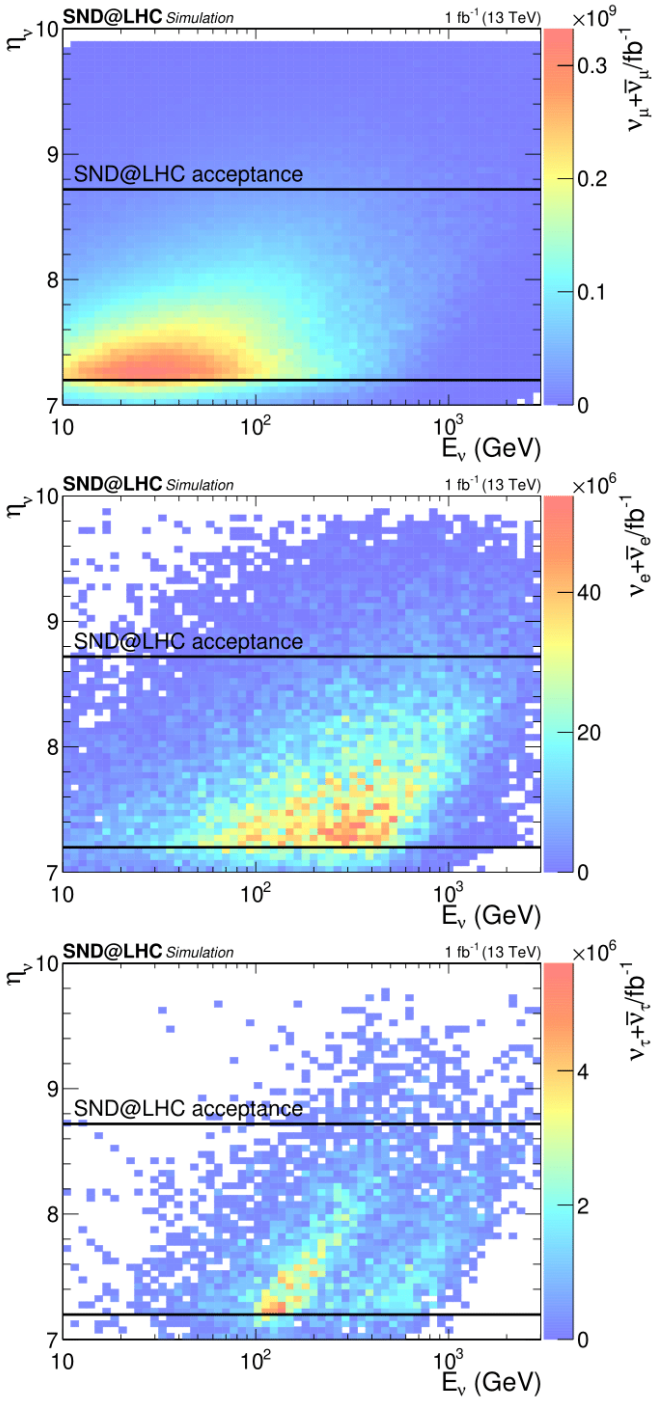

Figure 1.2: Neutrino and anti-neutrino flux as a function of ν energy E_ν and pseudo-rapidity η_ν for muon (top), electron (middle) and tau (bottom) neutrinos [58].

insight into the heavy-quark production in an unexplored domain. Hence, SND@LHC has the potential to measure charmed-hadron production indirectly through the observation of electron neutrinos and anti-neutrinos. However, up to now, charmed-hadron production in pp collisions has been studied at the LHC at lower pseudo-rapidity values. The LHCb experiment has precisely measured charm and beauty production at $\eta < 4.5$ [40].

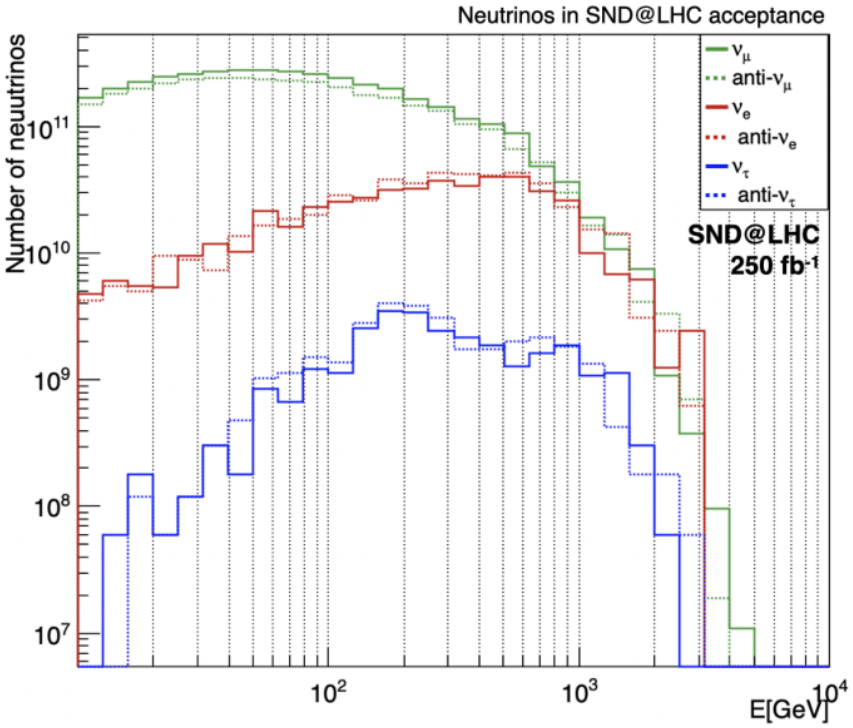

Figure 1.3: Energy spectrum of the different types of incoming neutrinos and anti-neutrinos as predicted by the DPMJET/FLUKA simulation, normalized to $250\,\mathrm{fb}^{-1}$ [61].

The cross-section measurements for $pp \to \nu_e X$ and the ν_e flux are used to estimate [58] the yield of charmed hadrons that produce neutrinos in the SND@LHC pseudo-rapidity range. A pseudo-experiment is generated to observe the expected number of ν_e and $\bar{\nu}_e$, and an unfolding procedure is applied to extract the reconstructed energy spectrum free from resolution and reconstruction efficiency effects. Assuming the SM predictions for ν_e and $\bar{\nu}_e$ charged-current cross-sections, this procedure allows for the extraction of the energy spectrum and the total yield of electron neutrinos produced in the LHC pp interactions in the pseudo-rapidity range of $7.2 < \eta < 8.4$. The geometrical acceptance of the SND@LHC detector is accounted for the different charmed

hadron species decaying into ν_e and $\bar{\nu}_e$. To study the correlation between the electron neutrino and the parent charmed hadron, a simulation with POWHEG [18] and PYTHIA8 [19] was performed.

Considering the uncertainties in the correlation between the yield of charmed hadrons in a given pseudo-rapidity region and the neutrinos in the measured η region, it was evaluated [61] that the measurement of the charmed-hadron production in pp collision can be done with a statistical uncertainty of about $5\,\%$. The systematic error of $35\,\%$ is the primary contributor to the uncertainty. According to the simulation, developed by the CERN EN-STI team [58], $10\,\%$ of the ν_e and $\bar{\nu}_e$ that interact in the detector arise from kaon decays, specifically from $K^0 s$ decays, and have energies below 200 GeV. Therefore, assuming that the deep-inelastic charged-current cross-section of the electron neutrino follows the SM prediction, electron neutrinos can be used to investigate the production of charm in the pseudo-rapidity range of SND@LHC. However, before this can be achieved, the instrumental effects must be unfolded, and the contribution of K must be subtracted. Data can be used to measure the $pp \rightarrow \nu_e X$ cross-section with an accuracy of $15\,\%$ [58], dominated by the systematic uncertainty of the unfolding procedure.

Furthermore, the measurement of charmed hadrons enables the determination of the corresponding open charm production in the same rapidity window, given the linear correlation between the parent charm quark and the hadron, as illustrated in Figure 1.4. Neutrinos in the SND@LHC acceptance come from charmed hadrons either in the same pseudo-rapidity or with smaller/larger η. At the LHC, the dominant partonic process for associated charm production is the scattering of two gluons, which produces a $c\bar{c}$ pair [12]. The average lowest momentum fraction (x) of interacting gluons probed by SND@LHC is around 10^{-6} [58]. Extracting the gluon PDF at such low values of x, where it is completely unknown, could provide valuable information for future experiments that probe the same low x range. Moreover, this could reduce uncertainties in the flux of very-high-energy (PeV scale) atmospheric neutrinos produced in charm decays, which is then applied to scope astrophysical sources with neutrinos [39, 59].

1.2 Lepton flavour universality test in neutrino interactions

The emulsion technology developed by the OPERA experiment [20, 32, 44] in a hybrid detector has demonstrated its capability to identify all three neutrino flavours. As the same technology has been implemented in the SND@LHC

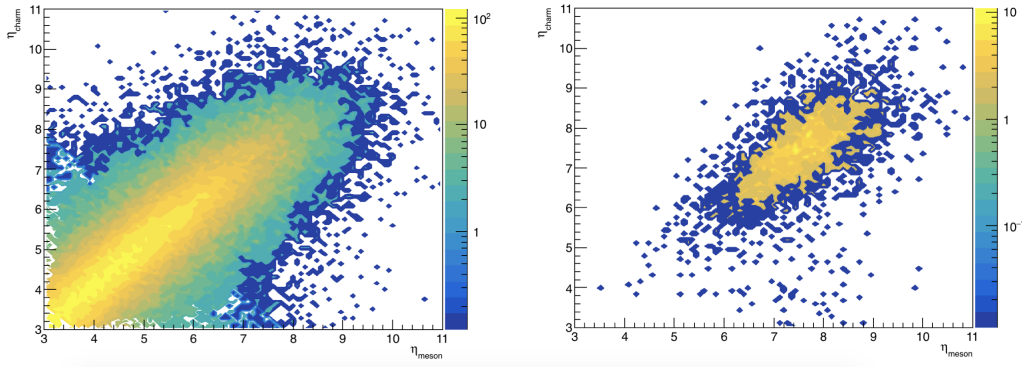

Figure 1.4: (Left) Correlation between pseudo-rapidities of the parent charm and the charmed hadron. (Right) Only events where the neutrino is in the SND@LHC acceptance are selected [58].

detector, it provides an opportunity to test Lepton Flavour Universality (LFU) in the neutrino sector by measuring the ratio of ν_e/ν_μ and ν_e/ν_τ interactions. From the observed decay rates of muons and tau leptons, it is found that the strength of the weak interaction is the same for all lepton flavours [29].

The location of SND@LHC allows for the interception of the neutrino flux component that originates from the decays of c and b quarks, which provides access to tau neutrinos through the decays of D_s mesons. The production of both ν_e and ν_τ primarily occurs via semi-leptonic and fully leptonic decays of charmed hadrons. In the pseudo-rapidity range of interest, tau neutrinos are essentially only produced in $D_s \to \tau\nu_\tau$ and the subsequent τ decays. From the results of PYTHIA Monte Carlo simulations, approximately $8\,\%$ of ν_τs comes from beauty hadron decays [58]. Conversely, electron neutrinos are produced in the decay of all ground-state charmed hadrons, primarily D^0, D, D_s and Λ_c. Therefore, the ν_e/ν_τ ratio depends solely on charm hadronisation fractions and decay branching ratios. The systematic uncertainties due to the charm-quark production mechanism cancel out, and the ratio becomes sensitive to the $\nu-$nucleon interaction cross-section ratio of the two neutrino species. Hence, it can be considered a test of the lepton flavor universality in neutrino interactions. The ν_e to ν_τ ratio (R_{13}) can be written in terms of the known branching ratios convoluted with the charmed hadron species. Such quantities with the tilde symbol refer to expected values in the SND@LHC acceptance [58]:

$$R_{13} = \frac{N_{\nu_e+\bar{\nu_e}}}{N_{\nu_\tau+\bar{\nu_\tau}}} = \frac{\sum_i \tilde{f_{c_i}} \tilde{Br}(c_i \to \nu_e X)}{\tilde{f_{D_s}} \tilde{Br}(D_s \to \tau\nu_\tau)}, \tag{1.1}$$

where $\tilde{f_{c_i}}$ are the charmed hadron fractions and $\tilde{Br}(c_i \to \nu_e X)$ are the branching ratios of each charm species, which include also the contribution from the

subsequent τ decay. The estimate of the branching ratios has a systematic uncertainty of about $22\,\%$ while the statistical uncertainty is dominated by the low statistics of the ν_τ sample [61], which corresponds to a $30\,\%$ accuracy.

The situation is different for $\nu_e s$ when compared to $\nu_\mu s$. The muon neutrino and electron neutrino spectra in the SND@LHC acceptance are shown in Figure 1.5. The component from heavy-quark decays is represented as the filled area. The muon-neutrino flux is heavily contaminated by muon neutrinos from π and k decays; hence the production mechanism cannot be considered the same. However, the contamination dominates at low energies and remains relatively flat at the level of $35\,\%$ for $E > 600GeV$, as observed by inspecting Figure 1.5. Therefore, the ν_e to ν_μ ratio (R_{12}) can be used as a test of LFU for $E > 600GeV$, where the contamination of ν_μ and $\bar{\nu_\mu}$ from pions/kaons ($\omega_{\pi/k}$) is uniform. In this case [58]

$$R_{12} = \frac{N_{\nu_e+\bar{\nu_e}}}{N_{\nu_\mu+\bar{\nu_\mu}}} = \frac{1}{1+\omega_{\pi/k}}. \tag{1.2}$$

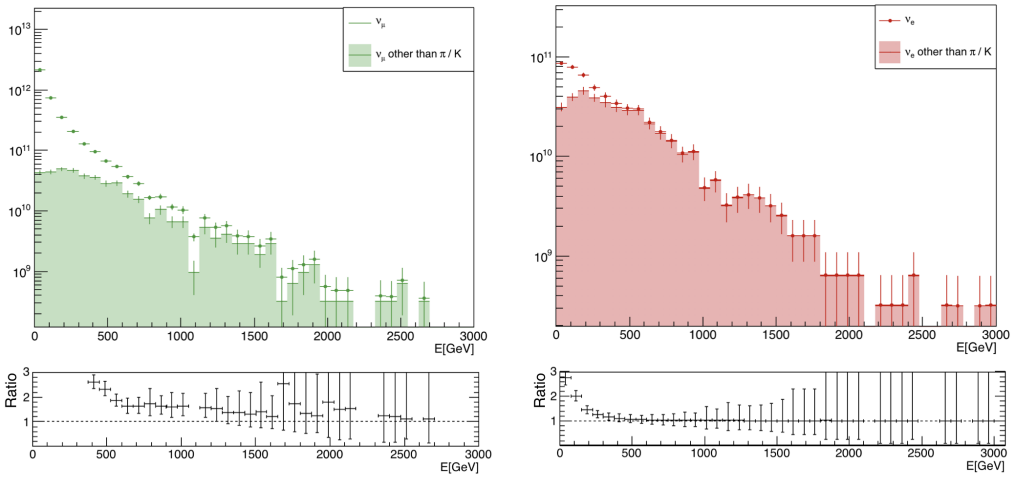

Figure 1.5: Energy spectrum of muon (left) and electron (right) neutrinos and anti-neutrinos in SND@LHC acceptance [58]. Filled areas represent the component coming from charm decays.

The ratio R_{12} is not affected by systematic uncertainties in the weighted branching fractions and charmed-hadron fractions since charmed hadrons decay almost equally into ν_e and ν_μ. The uncertainties are due to π and k production in the SND@LHC acceptance and to their propagation through the machine elements along the beamline. The simulation of the light-meson production yield in the forward region is constrained by results published by the LHCf Collaboration [25]. The charged meson propagation through the LHC machine is

simulated with FLUKA [34] and shows excellent agreement with measurements performed around the beamline. As a result, the ν_e/ν_μ ratio provides a test of the lepton flavour universality with an uncertainty of $15\,\%$, with an equal $10\,\%$ statistical and systematic contribution [61].

1.3 Measurement of the NC/CC ratio

Having the capability to distinguish charged-current (CC) and neutral-current (NC) neutrino interactions, it becomes feasible to measure the ratio between NC and CC interactions as an internal consistency test. The neutrino flavour can be identified in CC interactions by observing the corresponding charged lepton produced in the final state. Conversely, the NC process is flavour-insensitive. In the approximation that the differential ν and $\bar{\nu}$ fluxes as a function of energy are equal, the NC/CC cross-section ratio can be expressed as:

$$P = \frac{\sum_i \sigma_{NC}^{\nu_i} + \sigma_{NC}^{\bar{\nu}_i}}{\sum_i \sigma_{CC}^{\nu_i} + \sigma_{CC}^{\bar{\nu}_i}}. \tag{1.3}$$

This ratio is equal to the ratio of observed interactions, and the convolution with the flux cancels out in the ratio.

At the high energies of the LHC neutrinos, deep-inelastic scattering is the dominant interaction mechanism [58], and the scattering off nuclei can be approximated as the incoherent sum over protons and neutrons. By summing over neutrinos and anti-neutrinos, the ratio between NC and CC deep-inelastic interaction cross-sections at a given energy can be expressed as a function of the Weinberg angle (θ_W) [37]:

$$P = \frac{1}{2}\left\{1 - 2\sin^2(\theta_W) + \frac{20}{9}\sin^4(\theta_W) - \lambda(1 - 2\sin^2(\theta_W))\sin^2(\theta_W)\right\}. \tag{1.4}$$

Here, λ represents the dependence on the unequal number of protons and neutrons in the target. Thus, measuring the ratio between NC and CC interactions can be used to determine the Weinberg angle.

SND@LHC plans to measure this ratio as a consistency test of the Standard Model, instead of measuring the Weinberg angle directly since it's already known with a precision of $1\,\%$ [2, 3]. The statistical uncertainty on the NC/CC ratio for observed events is expected to be lower than $5\,\%$, associated with the number of NC observed interactions, while the systematic uncertainty on the unfolded ratio is about $10\,\%$ [61].

1.4 Neutrino-induced charm production

At the energies of SND@LHC, high-energy neutrino interactions produce charmed hadrons at the level of about 10 % of the total rate [58], making them a valuable means for investigating charm physics. In contrast to colliding beams, neutrino interactions can produce charmed hadrons through quasi-elastic and diffractive scattering processes, turning them in a unique tool for studying exclusive charm physics [11]. Figure 1.6 illustrates the Feynman diagrams for the production of charmed hadrons in neutrino and anti-neutrino interactions.

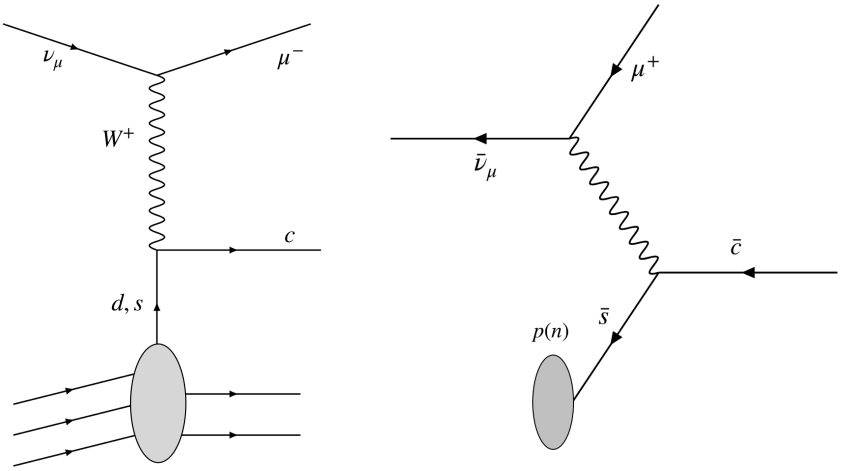

Figure 1.6: Charm production in neutrino (left) and anti-neutrino (right) charged-current interactions [58].

The nuclear emulsion technology offers an unmatched possibility to identify charmed hadrons without the need for kinematical cuts by observing a two-vertex topology. The CHORUS experiment [24], which used nuclear emulsions, recorded the largest neutrino flux and detected 2013 charm candidates from ν_μ and 32 from $\bar{\nu_\mu}$. A tau-neutrino candidate with charmed-hadron production was reported by the OPERA experiment [54]. However, no charm candidate has ever been reported from electron-neutrino interactions. The measurement of the relative yield of charm production in muon and electron neutrino and anti-neutrino interactions will update previous studies on charm physics and explore previously inaccessible channels. The right panel of Figure 1.6 shows that charmed-hadron production in anti-neutrino interactions selects the anti-strange quark in the nucleon. Therefore, SND@LHC measurements can be used to determine the s-quark content of the nucleon and provide essential information for many precision tests of the Standard Model.

Table 1.1 summarises the primary physics objectives of Run 3 using the SND@LHC detector for neutrino interaction analyses. The proposed measurements, along with their estimated uncertainties, are reported.

Measurement	Uncertainity	
	Stat.	Sys.
$pp \to \nu_e X$ cross-section	5 %	15 %
Charmed hadron yield	5 %	35 %
ν_e/ν_τ ratio for LFU test	30 %	22 %
ν_e/ν_μ ratio for LFU test	10 %	10 %
NC/CC ratio	5 %	10 %
Observation of high-energy ν_τ		

Table 1.1: Measurements proposed by SND@LHC in the analyses of neutrino interactions with Run 3 data .

1.5 Feebly Interacting Particles

One of the main challenges in particle physics today is to determine the microscopic identity and cosmological origin of dark matter (DM). During the last decades [51], a significant experimental effort has focused on DM masses around 100 GeV. This is motivated by the observation that particles in this mass range predicted by supersymmetry or other weak-scale theories automatically lead to a particle density in excellent agreement with the observed DM density. Such particles are referred to as Weakly Interacting Massive Particles (WIMPs), a particle interacting with baryonic matter with couplings comparable to the weak interaction. Recently, there has been growing interest in widening the scope of these searches. The lack of discoveries of weak-scale particles that could act as mediators in primordial annihilation processes has changed the emphasis, since the choice of masses around 100 GeV was completely driven by specific model considerations, especially related to supersymmetry. A more generic WIMP, which annihilates into gauge bosons via ordinary weak interactions, prefers larger masses, in the GeV–TeV range. The increasing interest in understanding the nature of DM has led to a rising experimental effort by the scientific community in both direct and indirect searches. Complementary approaches, such as the direct observation of accelerator-produced dark matter via scattering off electrons, have been proposed, as with the SHiP experiment at the CERN SPS [37, 47].

One alternative research direction that is currently gaining a surge of interest [51] is the search for Feebly Interacting Particles (FIPs), a new family of particles which are either very light, but only rarely produced in collisions among ordinary particles, or have very long lifetimes, thus travelling macroscopic distances. The hypothetical existence of FIPs is a valid open question in particle physics today, also motivated by theoretical models for DM. In the presence ofhidden sectors with a structure as rich as the SM, it is not unrealistic to expect new particles behaving as FIPs. This attention is also stimulated by the lack of any discovery in various direct detection dark matter experiments that have reached unprecedented levels of precision, as well as in collider experiments that have collected large data samples analyzed with increasingly sophisticated techniques. The sensitivity at masses lower than 10 GeV is scarce because of the difficulty in detecting the corresponding very soft recoils, given the expected non-relativistic nature of galactic dark matter. Current cosmic direct-detection experiments searching for elastic nuclear recoils lose sensitivity to particles with masses below a few GeV [52, 56]. Therefore, accelerator-based experiments at the intensity frontier represent an alternative and appealing path in this pursuit [42]. In a fixed-target experiment at an accelerator, the candidate dark matter particle is ultra-relativistic, and hence, the experimental challenges in its detection are different and less demanding than for experiments searching for dark matter originating in the galaxy. Of greater significance, collisions delivered by accelerators offer a general source of feebly coupled particles.

The SND@LHC experiment is capable of conducting model-independent direct searches for FIPs [61] by combining a search for a recoil signature with time-of-flight (TOF) measurement to reject neutrino interactions that may act as background. FIPs can be produced in pp scattering at the LHC interaction point, propagate to the detector, and decay or scatter inside it. The hybrid nature of the apparatus, which combines emulsion trackers and electronic detectors, makes it possible to distinguish the scattering of massive FIPs and neutrinos with a significance that depends on the particle mass [61]. A recent study [60] summarized SND@LHC's sensitivity to physics beyond the Standard Model by considering the scatterings of light dark matter particles χ via leptophobic $U(1)_b$ mediator V, as well as decays of Heavy Neutral Leptons, dark scalars, and dark photons. The excellent spatial resolution of nuclear emulsions and the muon identification system make SND@LHC well-suited to search for neutral mediators decaying into two charged particles. The search via scattering off nucleons provides the world-leading sensitivity to the process in a wide region of the parameter space, as shown in Figure 1.7.

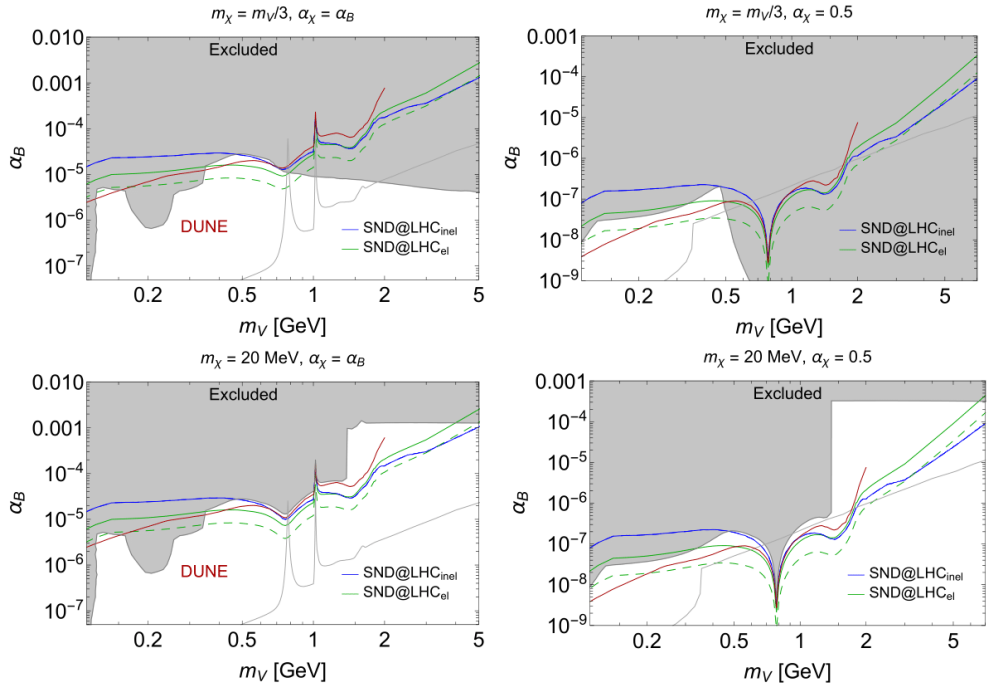

Figure 1.7: Sensitivity of the SND@LHC experiment to the leptophobic portal (2σ CL) for both elastic scattering off protons (green line) and deep-inelastic scattering (blue line) [60]. The grey region is already excluded by other researches.

Chapter 2

Detector layout

SND@LHC is a fixed target neutrino experiment at CERN, located in the TI18 tunnel, about 480 m downstream of the ATLAS interaction point (IP1), as shown in Figure 2.1. This location is ideally suited to shield the detector from most of the activity of IP1 by 100 m of rock. In Figure 2.2 LHC magnets for the deflection of charged particles produced in the LHC collisions are also shown.

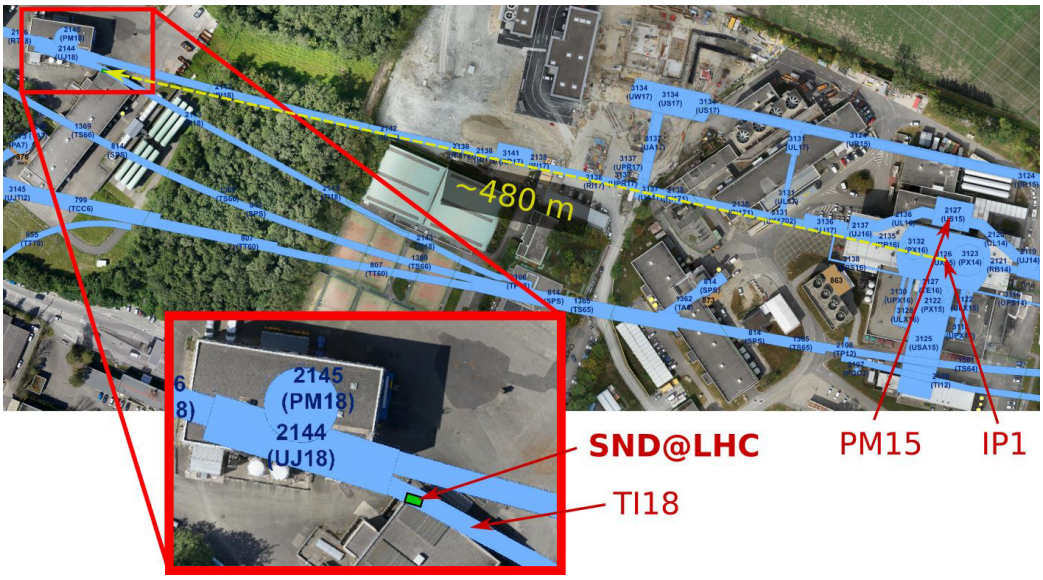

Figure 2.1: The location of the SND@LHC experiment in the TI18 tunnel.

The detector is designed to make measurements with LHC neutrinos in the unexplored pseduo-rapidity range $7.2 < \eta < 8.4$, identifying all the neutrino flavours with high efficiency, and to search for Feebly Interacting Particles (FIPs) directly through their scattering off atoms in the neutrino target. The charged-lepton identification and the measurement of the neutrino energy are essential

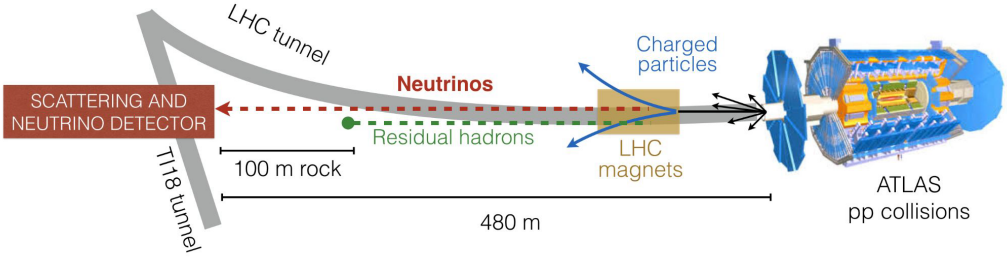

Figure 2.2: Schematic view of TI18 rock shielding and LHC magnets.

to distinguish among the three flavours in neutrino CC interactions and to point the corresponding neutrino source. These features were thus the main drivers in the design of the SND@LHC apparatus, that had also to account for geometrical constraints of the selected location.

A good solution, as demonstrated by the OPERA experiment [20], is a hybrid detector that combines nuclear emulsion technology and electronic detectors. Such an apparatus comprises three detector elements [61]:

- a neutrino target and vertex detector with good enough resolution to disentangle the neutrino-interaction vertex from the one of the tau-lepton decay;
- a calorimetric system to measure both the electromagnetic and hadronic energy with a good time resolution;
- a muon system to identify the muon produced in ν_μ CC interactions and in the muonic decay of the tau lepton. Geometrical constraints prevent adding a magnetised volume that would allow to separate neutrinos from anti-neutrinos.

This section gives a detailed description of the sub-systems of the SND@LHC detector, which includes the veto, the vertex detector and electromagnetic calorimeter, the muon system and hadronic calorimeter. The apparatus begins upstream with the veto system that tags events with charged particles entering the detector from the front. It is followed downstream by the target region, a mass of about $830\,\mathrm{kg}$ instrumented with five walls of Emulsion Cloud Chambers (ECC), each followed by a Scintillating Fibre (SciFi) plane. The ECC technology alternates emulsion films, acting as tracking devices with micrometric accuracy, with passive material acting as neutrino target. The SciFi detectors predict the location of the neutrino interactions in the emulsion walls,

provide the time stamp to the events reconstructed in the emulsion and complement the emulsion chamber for the calorimetric measurement of electromagnetic showers with a total of 85 radiation lengths X_0 [61].

Veto and target system are contained in a borated polythylene/actrylic box which has the dual function of acting as a neutron shield from low energy neutrons and maintaining controlled temperature and humidity levels in order to guarantee optimal conditions for emulsion films. The target system is followed downstream by a muon system, performing as a hadronic calorimeter and a muon identification system. It consists of eight iron slabs making up 9.5 interaction lengths λ_{int} in total, each followed by one or two planes of scintillating bars. The layout of the detector, with the exclusion of the neutron shield, can be seen in Figure 2.3.

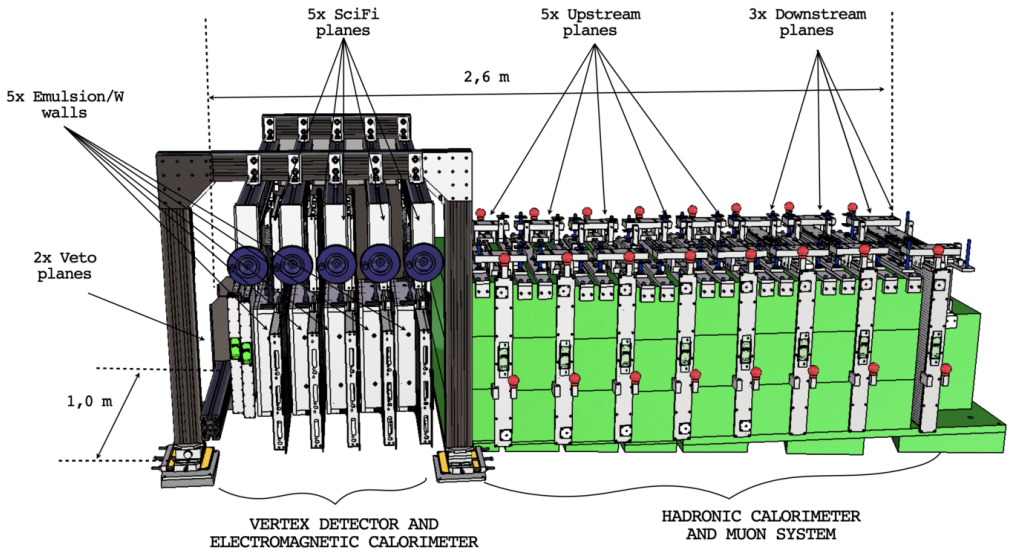

Figure 2.3: Layout of the SND@LHC experiment [61].

The detector exploits all the available space in the TI18 tunnel to cover the desired range in pseudo-rapidity. Figure 2.4 shows the top and side views of the detector positioned inside the tunnel. In the side view it can be noticed that the floor is inclined. The size of the tunnel, the tilted slope of the floor, and the distance of tunnel walls and floor from the nominal collision axis, imposed several constraints to the detector design. Recently, in February 2023, three concrete walls were installed in order to shield the detector and the electronic racks against neutrons and secondary hadrons associated with beam 2[1]. A chicane solution was chosen to allow free passage of personnel and material, as shown in Figure 2.5.

[1]Beam 2 is the counter clockwise circulating beam in LHC [10].

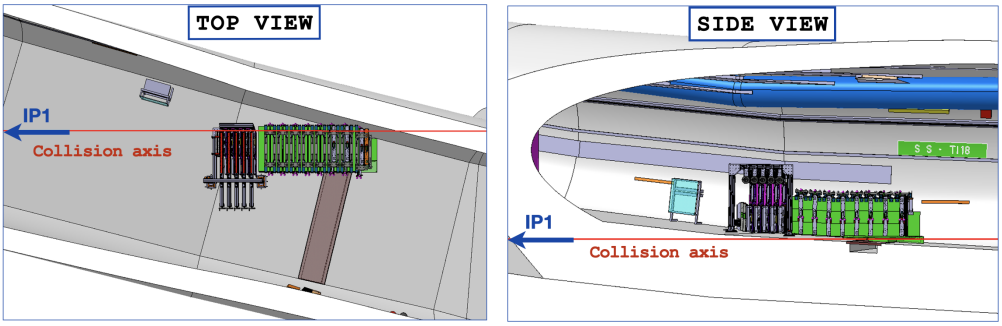

Figure 2.4: Top and side views of the SND@LHC detector in the TI18 tunnel [61].

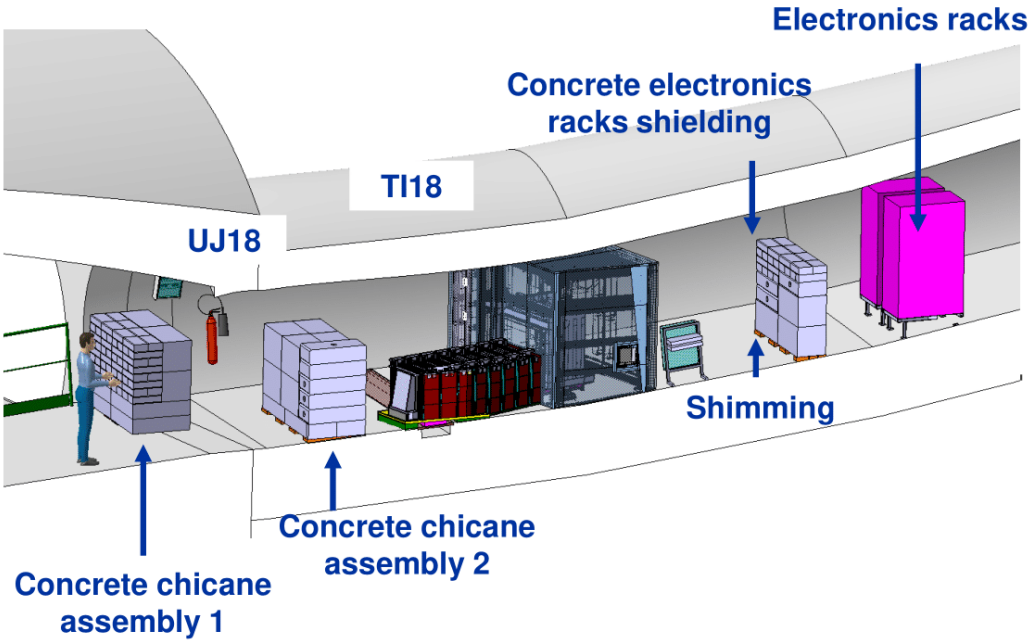

Figure 2.5: Schematic view of concrete shield blocks at the detector in the TI18 tunnel.

The detector layout was therefore optimised in order to find the best compromise between geometrical constraints and the following physics requirements [61]: a good calorimetric measurement of the energy requiring about $10\,\lambda_{int}$, a good muon identification efficiency requiring enough material to absorb hadrons, a transverse size of the target region having the desired azimuthal angular acceptance. The energy measurement and the muon identification set a constraint on the minimum length of the detector. With the constraints from the tunnel, such requirements determine the overall flux intercepted and therefore the total number of observed interactions.

2.1 Veto system

The veto system aims to identify charged penetrating particles entering the detector acceptance, mostly muons coming from IP1. It is located upstream of the target region and comprises two parallel planes of stacked plastic scintillating bars read out on both ends by silicon photomultipliers (SiPMs) as shown in Figure 2.6.

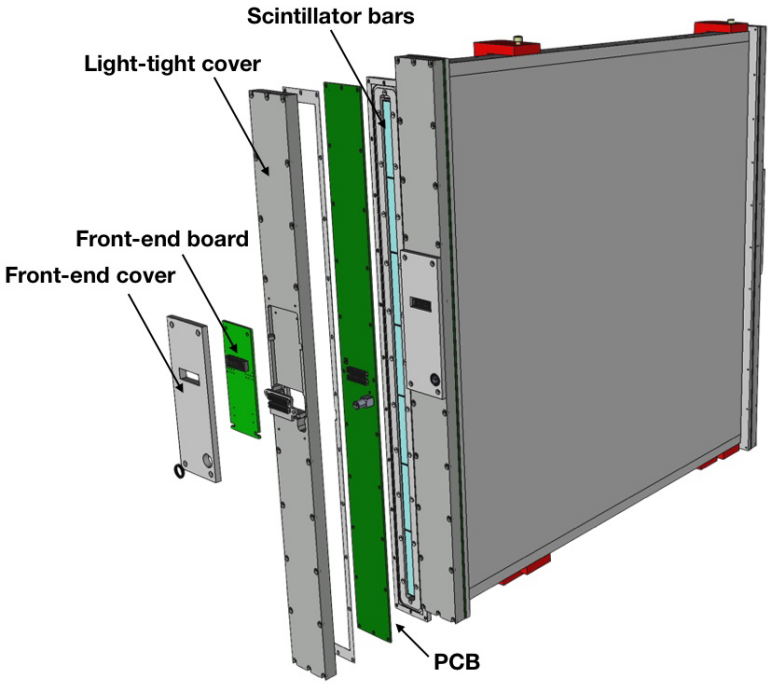

Figure 2.6: A rendering of the veto system illustrating the different components of the frames [61].

One plane consists of seven $1 \times 6 \times 42\,\mathrm{cm}^3$ stacked bars of EJ-200 scintillator [69]. EJ-200 is found to have the right combination of light output, attenuation length ($3.8\,\mathrm{m}$) and fast timing (rise time of $0.9\,\mathrm{ns}$ and decay time of $2.1\,\mathrm{ns}$). The emission spectrum peaks at$425\,\mathrm{nm}$, closely matching the SiPMs spectral response. The number of photons generated by a minimum-ionising particle crossing $1\,\mathrm{cm}$ scintillator is of the order of 10^4.

Bars are wrapped in aluminized Mylar foil to ensure opacity and isolate them from light in adjacent bars. Each bar end is read out by eight Hamamatsu S14160-6050HS ($6 \times 6\,\mathrm{mm}^2$, $50\,\mu\mathrm{m}$ pitch) SiPMs [65]. The SiPMs are mounted on a custom built PCB that covers all seven bars on each end of a plane. Each individual SiPM signal is read out by the front-end (FE) boards, from which a DAQ board collects the digitized signals. A CAEN mainframe, which is shared with the muon system, houses low voltage and high voltage power supplies. The stacked bars for each plane are housed in an aluminum frame. An aluminum cover on each end is used to ensure light tightness and also acts as a heat sink for the FE board, which is placed in a groove in the cover on the side opposite to the PCB.

The two frames of the veto system are held together by a small support structure. This in turn is attached to the support of the target region within $1\,\mathrm{mm}$ accuracy, as shown in Figure 2.7. A vertical shift of $2\,\mathrm{cm}$ between the two frames allows for $100\,\%$ coverage of the target region, compensating for inefficiency due to the dead area between bars introduced by wrapping material ($\sim 60\,\mu\mathrm{m}$) and variations in bar height ($\sim 250\,\mu\mathrm{m}$). The DAQ board is mounted on the support frame directly in front of the veto planes.

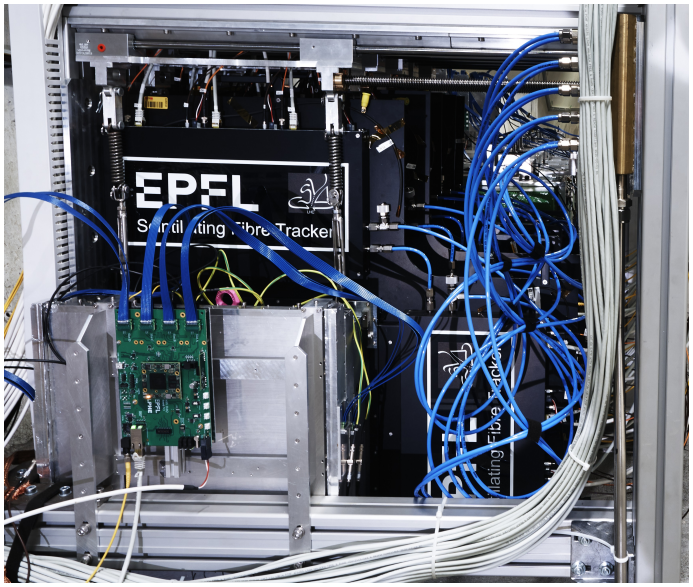

Figure 2.7: Front view of the veto system in the target region [63].

2.2 Target and vertex detector

The emulsion target is designed according to the Emulsion Cloud Chamber (ECC) technology, that makes use of nuclear emulsion films interleaved with passive layers to build up a tracking device with sub-micrometric spatial and milliradian angular resolution, as demonstrated by the OPERA experiment [20]. It is capable of detecting short-lived charmed hadrons [31] and tau leptons [44] by disentangling their production and decay vertices. It is also suited for FIP detection through the direct observation of their scattering off electrons or nucleons in the passive plates. The ECC technology alternates $1\,\mathrm{mm}$-thick tungsten plates as the neutrino target with $\sim 300\,\mu\mathrm{m}$-thick emulsion films, acting as a vertex detector with micrometric resolution, measuring the trajectory of all the charged particles produced in a neutrino interaction. The fine segmentation of active films interleaving tungsten plates is motivated by the longitudinal resolution required to observe the tau lepton track.

The emulsion films are replaced after an integrated luminosity of about $25\,\mathrm{fb}^{-1}$, thus it is essential to keep the combinatorial background in the association of track segments sufficiently low. Furthermore, such a segmentation also makes the emulsion-tungsten ECC a high-sampling electromagnetic calorimeter with more than three active layers every radiation length X_0, essential for electron identification and discrimination against neutral pion decays [45]. The layout of the target was optimised to cover the desired pseudo-rapidity region, maximizing the azimuthal angular acceptance. The surface of the emulsion is large enough to contain the event in the brick, with reduced number of bricks per wall to minimise the dead area, altogether with the ease of emulsion production and scanning process.

2.2.1 Target walls

Nuclear emulsion films are the most compact, thinnest and lightest three-dimensional tracking detectors with sub-micrometric position and milliradian angular resolution. They consist of a high concentration of very fine silver halide grains, dipped in a thin layer of gelatine. Charged ionizing particles cause chemical alterations in the grains, and such silver ions transform into silver atoms, darkening after the film development.

A nuclear emulsion film has two sensitive layers ($70\,\mu\mathrm{m}$-thick) on both sides of a transparent plastic base ($190\,\mu\mathrm{m}$-thick). By connecting the two hits (micro-tracks) generated by a charged particle on both sides of the base, the slope of the track can be measured with milliradian accuracy. The whole detector contains $\sim$ 1200 emulsion films, for a total of $44\,\mathrm{m}^2$. Those are currently produced by the Nagoya University in Japan and by the Slavich Company in

Russia [61]. Tungsten is used as target material in order to maximise the interaction rate per unit volume. Its small radiation length ($\sim 3.5\,\mathrm{mm}$) allows for good performance in the electromagnetic shower reconstruction in the ECC. Moreover, the low intrinsic radioactivity makes tungsten a suitable material for an emulsion detector.

The emulsion target is made of five walls with a sensitive transverse size of $384 \times 384\,\mathrm{mm}^2$. Each wall consists of four cells, called bricks, as illustrated in Figure 2.8. Each brick is composed of 60 emulsion films (or 57, depending on the emulsion manufacturer) with a transverse size of $192 \times 192\,\mathrm{mm}^2$, interleaved with 59 (or 56 respectively) 1 mm-thick tungsten plates. The total thickness of the resulting brick is $\sim 78\,\mathrm{mm}$, making $\sim 17 X_0$, with a mass of $41.5\,\mathrm{kg}$. The overall target mass with five walls of 2×2 bricks amounts to $\sim 830\,\mathrm{kg}$.

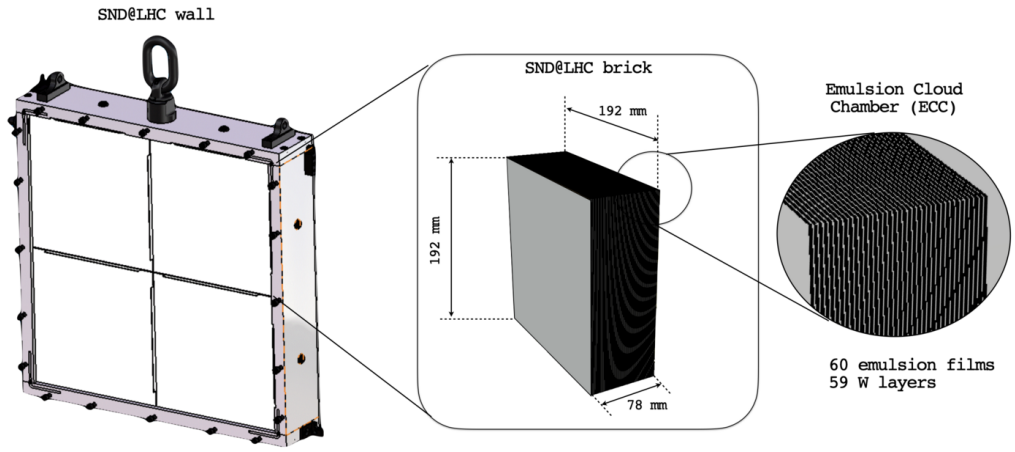

Figure 2.8: An emulsion wall is composed of four bricks, each consisting of 60 emulsion films interleaved with 59 tungsten plates [61].

An ECC wall is contained in an aluminum box that hosts the four bricks, which are assembled one after the other by piling up 60 emulsion films and 59 tungsten plates, in dark room condition. The box is then closed with 8 small aluminium plates that keep the necessary pressure to avoid relative displacements between emulsion films in all directions, and with 20 screws sealing the cover that ensures the light tightness. The walls are then transported to the TI18 tunnel by means of custom trolleys and, once there, inserted into the mechanical structure of SND@LHC. The different phases of the wall assembly, transportation and installation are described in Figure 2.9.

(a) (b) (c)

Figure 2.9: Target wall during the assembly with tungsten plates and emulsion films (a), on the transportation trolley (b) and suspended from the mechanical structure (c) [61].

2.2.2 Neutron shield and cold box

The interaction of proton beams with the residual gas inside the LHC beam pipe produces low energy neutrons, with a spectrum ranging from a few meV to a few hundreds of MeV, about half of them being thermal neutrons. The neutron flux expected in the TI18 tunnel is predominantly produced by beam 2 that passes by TI18 while moving towards IP1. In order to shield the emulsion target from thermal neutrons, a box made of $4\,\mathrm{cm}$-thick $30\,\%$ borated polyethylene and $5\,\mathrm{cm}$-thick acrylic layers was built around the target region, as shown in Figure 2.10. Doors on the upstream side and the corridor side of the detector provide easy access for maintenance and for emulsion wall replacements. The box acts also as an insulation chamber. For the long-term stability of emulsion films, a cooling system was installed to keep the temperature of the target at $(15 \pm 1)\,^{\circ}\mathrm{C}$ and the relative humidity in the range 40 to $50\,\%$.

2.2.3 Target mechanics

The mechanical structure of the SND@LHC target was designed to have a single support structure for both the five emulsion/tungsten walls and the five SciFi planes. It is made of a vertical rectified aluminum plate, that guarantees a fine mechanical alignment of target walls, and of five aluminum horizontal profiles, each sustaining a target wall, as shown in Figure 2.11.

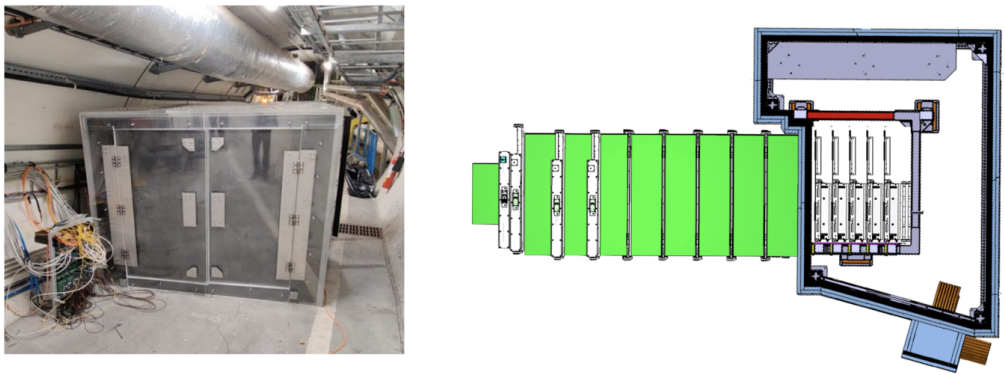

Figure 2.10: Neutron-shielded box surrounding the target region. On the left a picture of the assembled shield taken from upstream, and on the right the top view of a schematic drawing [61].

Figure 2.11: Mechanical support of the target system after the installation (left) and fully loaded with wall boxes and SciFi planes (right) [61].

I have personally taken part in the whole target replacement procedure. The five walls were assembled in two days in the dark room (Figure 2.12), then they were subsequently transported with the use of trolleys to the experiment location (Figure 2.13). Once there (Figure 2.14), I followed the extraction of dummy walls (Figure 2.15) and the installation of the five instrumented walls. Each wall box was placed into the loading position with the transportation trolley, it was then suspended to the structure, translated, secured and aligned to the final position (Figure 2.16). The ritual picture of the installation procedure successfully completed is shown in Figure 2.17.

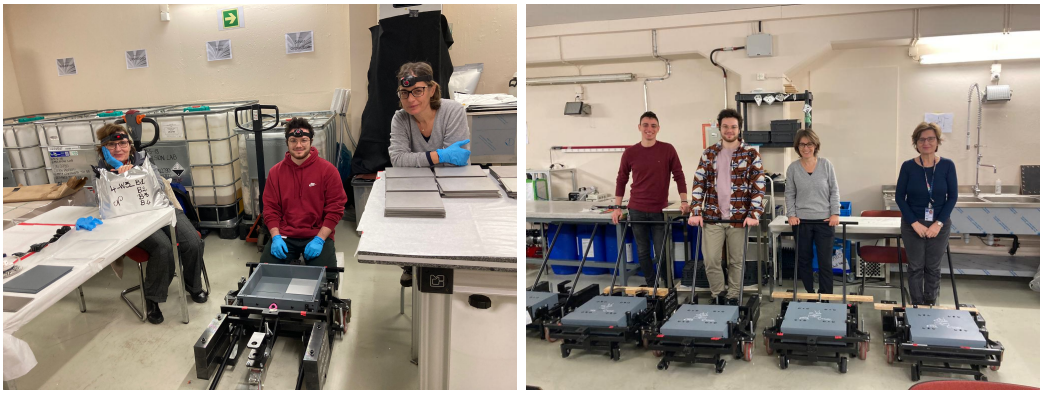

Figure 2.12: Photos taken before (left) and after (right) the wall assembly in the dark room.

Figure 2.13: Transportation of the five trolleys to the ATLAS cavern access (left) and inside the tunnel to TI18 (right).

Figure 2.14: Photo of myself at the detector location for the very first time.

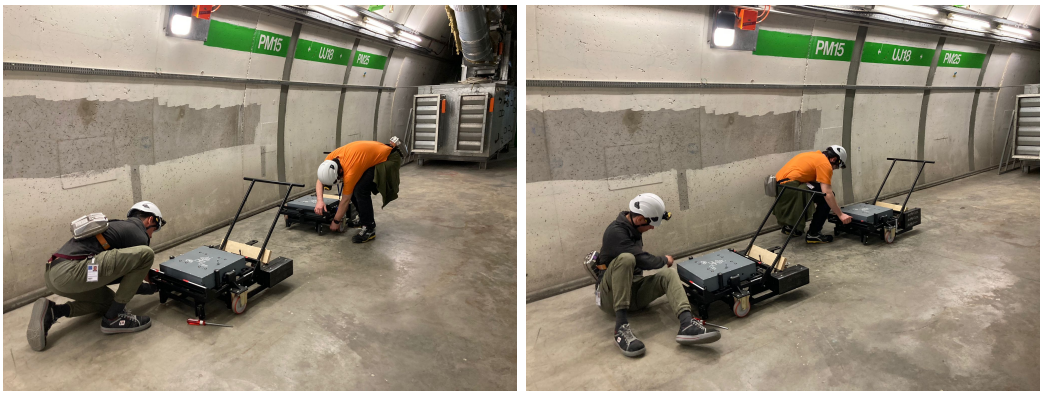

Figure 2.15: Securing the removed walls to the trolley to be transported back on the surface.

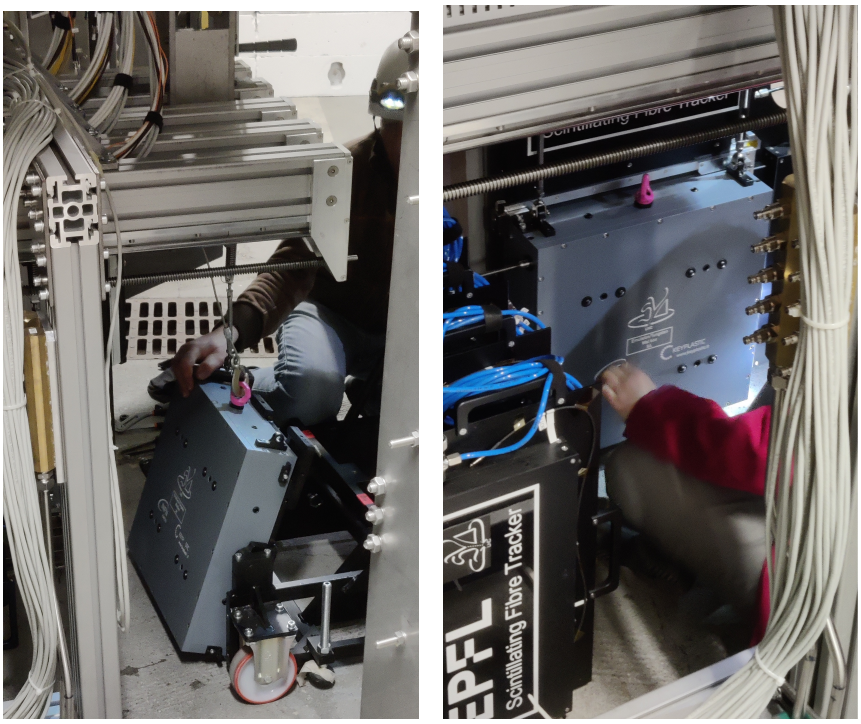

Figure 2.16: Installation of a wall to the target position.

Figure 2.17: Photo of the personnel involved in the target replacement at the detector location in TI18.

2.3 Target Tracker and electromagnetic calorimeter

The Target Tracker system consists of five scintillating fibre (SciFi) planes with active area of $40 \times 40\,\mathrm{cm}^2$ interleaving the five target walls. The SciFi technology is well suited to cover large surfaces in a low track density environment[2], where a $\sim 100\,\mu\mathrm{m}$ spatial resolution is required. The SciFi is meant to assign a timestamp to neutrino interactions reconstructed in the ECC walls and to provide an energy measurement of electromagnetic showers. The five target walls ($\sim 17\,X_0$ each) interleaved with SciFi tracker modules, form a coarse sampling calorimeter. An electron produced at the primary vertex will see on average about 40 X_0 in the target. Such a fine sampling of the target region provides high performance in the event matching between emulsion and electronic detectors, and in the calorimetric measurement of electromagnetic and hadronic showers.

The SciFi modules for SND@LHC, shown in Figure 2.18, are closely following the design of the modules built for LHCb. The double-cladded polystyrene scintillating fibres from Kuraray (SCSF-78MJ), with a diameter of $250\,\mu\mathrm{m}$, are blue emitting fibres with a decay time of $2.8\,\mathrm{ns}$ [61]. The fibres are arranged in six densely-packed staggered layers, forming fibre mats of $1.35\,\mathrm{mm}$ thickness, $399 \times 133\,\mathrm{mm}^2$ surface, with less than $500\,\mu\mathrm{m}$ dead zones. A picture of the cross section of such a mat is shown in Figure 2.19. A polycarbonate end-piece is glued to each end of the fibre mat and one side is brought in direct contact with the epoxy entrance window of a photo-detector.

Figure 2.18: The $5\,xy$ SciFi tracker planes setup [61].

[2]The expected rate of tracks from the ATLAS impact point is about $0.8\,\mathrm{Hz/cm}^2$ at peak luminosity [61].

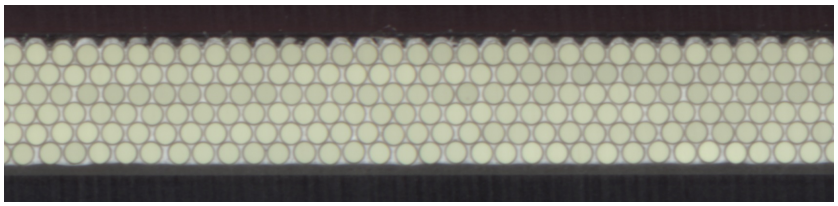

Figure 2.19: The fibre mat composed of six layers of fibres glued [61].

The readout consists of photo-detectors (S13552 SiPM multichannel arrays by Hamamatsu) at the end of the fibre module, connected to the FE board via PCB panels [61]. The array used has an active channel area of $0.25 \times 1.625\,\mathrm{mm}^2$, with large pixels of $62.5 \times 57.5\,\mu\mathrm{m}^2$, leading to an array of 26×4 pixels per channel. The SiPM multichannel array is optimised for low light-intensity detection. A single plane time resolution is $\sim 250\,ps$.

The mechanical alignment between the SciFi planes and the emulsion boxes is ensured with mechanical precision pins, constraining the relative position between the two objects. Because of the large number of tracks from high-momentum muons traversing the target, an accurate offline spatial alignment between SciFi planes can be obtained by using the tracks themselves.

2.4 Hadronic calorimeter and muon system

Downstream of the target region the hadronic calorimeter and muon system is located, shown in Figure 2.20. Its primary purpose is to identify passing-through muons. Moreover, together with the SciFi, it makes up a non-homogenous hadronic calorimeter for the measurement of the energy of the hadronic jet produced in the neutrino interaction and hence for the neutrino energy. The muon detector consists of eight iron walls, each with dimension $80 \times 60 \times 20\,\mathrm{cm}^3$ and a mass of $750\,\mathrm{kg}$ for a total of $9.5\,\lambda_{int}$, interleaved with the same number of planes made of scintillator bars. This adds up to an average total of $11\,\lambda_{int}$ for a shower originating in the target region, thus providing a good coverage of the hadronic showers.

The system is further divided in two sections. In the first five upstream layers (US), $6\,\mathrm{cm}$-thick horizontal scintillating bars are used. The three most downstream layers (DS) are made of fine-grained horizontal and vertical scintillating bars, in order to improve the identification efficiency of muons originating in neutrino interactions. The eight iron walls of the muon system, together with a smaller iron block at the end, are by themselves providing the support for the mechanical structure holding the eight muon detector planes.

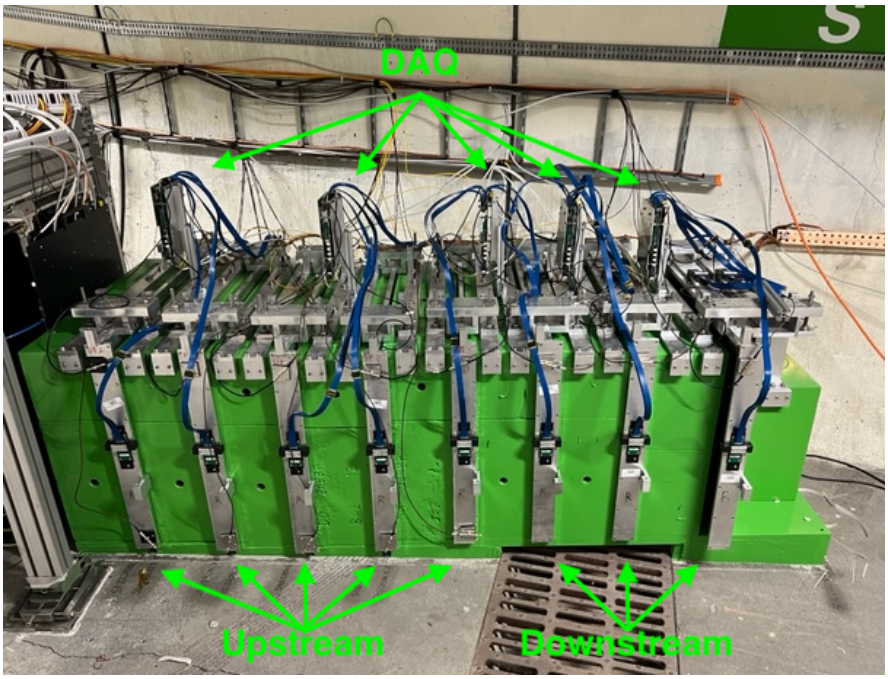

Figure 2.20: Picture of the hadronic calorimeter and muon system installed in TI18 [61].

2.4.1 Upstream system

The first five US layers are similar to the veto planes, albeit with different dimensions. Each layer consists of ten stacked bars of EJ-200, each bar having dimensions $1 \times 6 \times 82.5\,\mathrm{cm}^3$. The length was chosen to be longer than the iron blocks to allow the FE to be placed outside the gap between them, reducing overall length of the muon system along the collision axis. The bars are wrapped in aluminized Mylar foil in the same fashion as the veto system.

Every bar end is viewed by eight SiPMs: six Hamamatsu S14160-6050HS ($6 \times 6\,\mathrm{mm}^2$, $50\,\mu\mathrm{m}$ pitch) and two Hamamatsu S14160-3010PS [64] ($3 \times 3\,\mathrm{mm}^2$, $10\,\mu\mathrm{m}$ pitch) SiPMs. The SiPMs are arranged on a custom PCB, which is read out by a front-end board. The two smaller-size SiPMs are used to increase the dynamic range for each bar, which has to cover the low light yield generated by minimum ionizing particles and the large light yield in case of hadronic showers created in the target region or iron blocks. The latter can lead to large charged-particle fluxes through the bars, and hence to large signals, which can saturate the larger SiPMs but not the smaller ones. Bars and PCBs are housed in aluminum frames that provide light tightness.

2.4.2 Downstream system

Muon identification is completed with three high-granularity DS stations placed further downstream, providing the muon position with a resolution of better than $1\,\mathrm{cm}$. Each station consists of two planes of thin scintillating EJ-200 bars: one of 60 horizontal bars ($1 \times 1 \times 82.5\,\mathrm{cm}^3$ each), and one of 60 vertical bars ($1 \times 1 \times 63.5\,\mathrm{cm}^3$ each). The third station has an additional plane of vertical bars. Every horizontal bar is read out by one Hamamatsu S14160-6050HS SiPM on either end; verticals bar have one SiPM only on the top edge. Bars are individually wrapped in aluminized mylar foil, very tightly, minimising the light loss thanks to multiple reflections.

2.5 Detector installation and operation

The detector installation in TI18, including the iron blocks, cooling plants and the related electronics, was successfully carried out in November and December 2021, allowing the start of global commissioning by the end of December 2021. The neutron shield surrounding the target region was constructed in January and February 2022 and completed underground by March 15th. On April 7th, one-fifth of the target region was partially instrumented with emulsion films, as the very final step of the detector installation. A picture of the full detector installed in TI18 is shown in Figure 2.21.

The detector has been continuously taking cosmic ray data since the beginning of the 2022 and the LHC Run 3 data taking started on July 5th with the first stable beam at $6.8\,\mathrm{TeV}$ of 2022. There has been three target replacement during the year, until the last week of November 2022 when the data taking ended as well. In 2023 four more emulsion RUNs are planned, with the first being replaced on March 20th, with my partecipation. On April 21st the LHC received the first 2023 stable beam at $6.8\,\mathrm{TeV}$, getting into the second chapter of Run 3 proton physics.

Figure 2.21: Global view of the detector in TI18 [63].

Chapter 3

Software and Event Display

The offline software framework, sndsw, is based on the FairRoot framework [27], and makes use of the experience gained with the FairShip software suite, developed within the SHiP collaboration [35]. The reconstruction and analysis tools have been successfully applied to the SND@LHC use cases and further improved. Several simulation engines are available. Muons from IP1 simulated by FLUKA [34] and transported through the detector by Geant4 [9], muon deep inelastic scattering using Pythia6 [16], DPMJET3 [8] or Pythia8 [19] for neutrino production at IP1 and GENIE [23] for the neutrino interactions in the detector target. The detector geometry is implemented using the TGeo package of ROOT and used in the simulation by Geant4 as well as in the reconstruction. Electronic detectors and emulsion films are implemented as sensitive volumes. The Geant4 simulation stops with the deposition of energy in the sensitive detectors. The digitisation step takes this energy and simulates an electronic signal, taking into account the transformation to photons, the light propagation and absorption along the scintillating fibre or bar, the photodetection efficiency of the SiPMs and the response of the front-end. In addition, Geant4 had been used to investigate the neutron shielding performance of various materials.

An example of a display used during the detector commissioning including all electronic sub-systems is shown in Figure 3.1. Hits recorded in the electronic detectors are represented as triangles, with only the detector image in transparency on the background. Both the top view (xz projection) and the side view (yz projection) are illustrated. Since the scintillating bars of the veto system are horizontal only, the two red veto hits in Figure 3.1 can be seen exclusively in the side view. Conversely, the SciFi readout consists on SiPMs located on the horizontal and vertical orientations. In the last year, the event display underwent several improvements that will be described in this section.

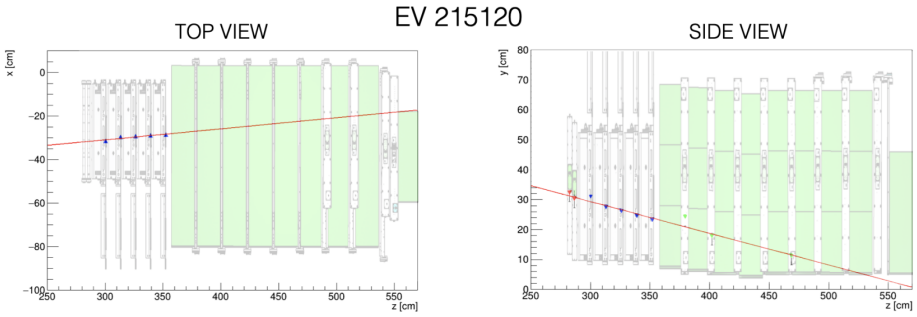

Figure 3.1: Event display showing the hits and the reconstructed track superimposed on the image of the detector layout.

3.1 Neutrino identification

Neutrinos are identified by the products of their scattering in the target. The identification of the neutrino flavour is performed in charged current interactions by distinguishing the charged lepton produced at the primary vertex. Electrons produced in neutrino scattering are identified by the observation of an electromagnetic shower induced inside the interaction brick. Electrons are distinguished from neutral pions thanks to the micrometric accuracy and fine sampling of the ECC, that is capable of observing the displaced vertex associated with the photon conversion. The left panel of Figure 3.2 shows a ν_e interaction in the OPERA emulsion cloud chamber. The electron produced at the primary vertex is clearly separated from the electromagnetic shower induced by the two photons produced by the π_0 decay.

Muon identification is relevant for both identifying ν_μ and ν_τ interactions. Charmed hadrons produced in ν_μ CC interactions constitute a background for the ν_τ search, if the primary muon is not identified. Muons are identified by the electronic detectors as the most penetrating particles, beyond the hadronic shower. Monte Carlo studies have shown [58] that $\sim 98.4\,\%$ of the muons produced in ν_μ CC interactions enter the muon system. Out of them, $\sim 91.5\,\%$ leave a hit in the last three planes of the muon identification system and can thus be identified.

The identification of τ lepton is based on purely topological criteria in the ECCs, through the observation of the tau decay vertex, together with the absence of any electron or muon at the primary vertex, following the technique developed by OPERA [22, 44]. Once the primary neutrino interaction vertex has been identified, secondary vertices, signatures of possible short lived particle decays, are searched for. This is done by a dedicated decay search procedure: tracks are defined as belonging to a secondary vertex if the impact parameter of the daughter track with respect to the primary vertex is larger than $10\,\mu\mathrm{m}$ [58]. The right panel of Figure 3.2 shows a ν_τ candidate detected in OPERA [30].

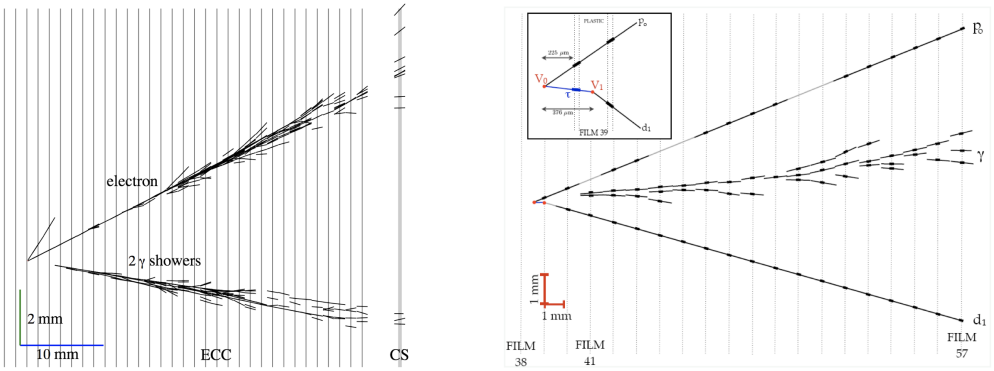

Figure 3.2: Display of reconstructed tracks in the OPERA emulsion detector for a ν_e (left) [28] and a ν_τ (right) [30] candidate event.

SND@LHC has the same granularity as in OPERA, alternating emulsion films with $1\,\mathrm{mm}$-thick passive material. This is motivated by the need to keep high tracking and vertexing performances in an environment with a high density of tracks. Event topologies that can be reconstructed in the SND@LHC ECC are illustrated in Figure 3.3. On top of that, in order to fully reconstruct and identify the neutrino event, the hybrid structure of the detector is exploited. A schematic representation of a ν_e and a ν_μ charged-current interaction in the electronic detectors is shown in Figure 3.4.

The occurrence of a neutrino interaction or a FIP scattering will be first detected by the target tracker and the muon system. Electromagnetic showers are expected to be absorbed within the target region and will therefore be identified by the target tracker, while muons in the final state will be reconstructed by the muon system. In addition, the combination of data taken from both systems will be used to measure the hadronic and the electromagnetic energy of the event.

3.2 Event Display

The urge to develop an accurate event display software became clear before the LHC Run 3 data, available from June 2022. The event display used during the Run 3 commissioning phase is illustrated in Figure 3.5. After having removed the sketchy detector picture on the background, the active volumes of the electronic detectors have been schematically drawn. The rectangular shapes represent the different sub-detectors, indicated with different colours, as well as the corresponding hit. The error bars of the veto and the Upstream System's hits intend to mimic the extension of the scintillating bars.

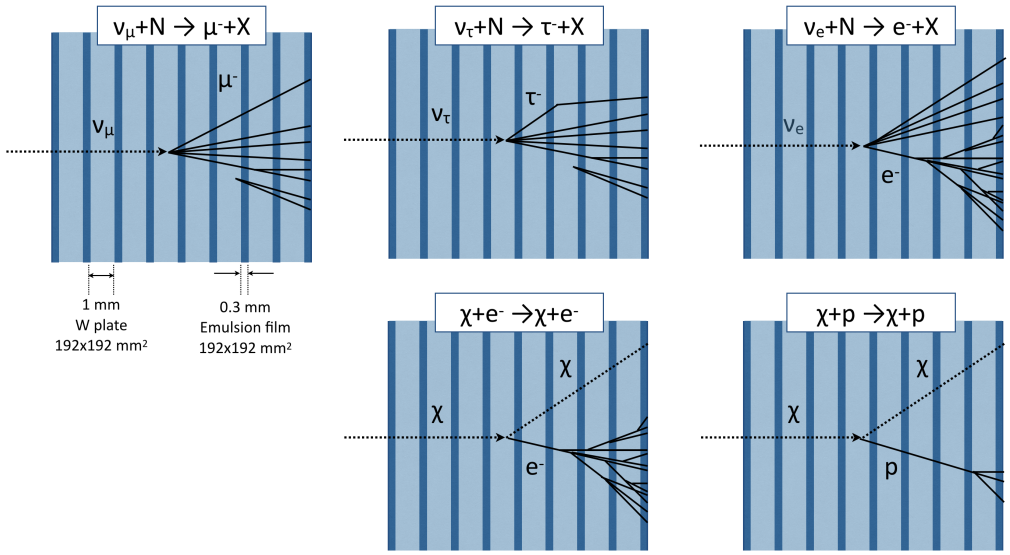

Figure 3.3: Illustration of simulated signal topologies that can be reconstructed in the SND@LHC emulsion target [58].

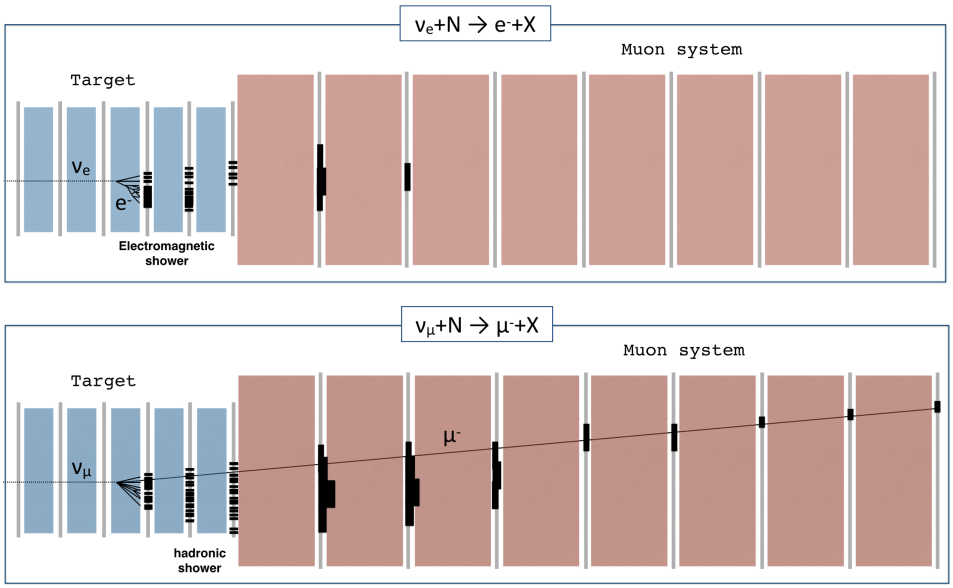

Figure 3.4: Schematic drawing of the reconstruction of a ν_e (top) and a ν_μ (bottom) simulated charged-current interaction in the SND@LHC detector [58].

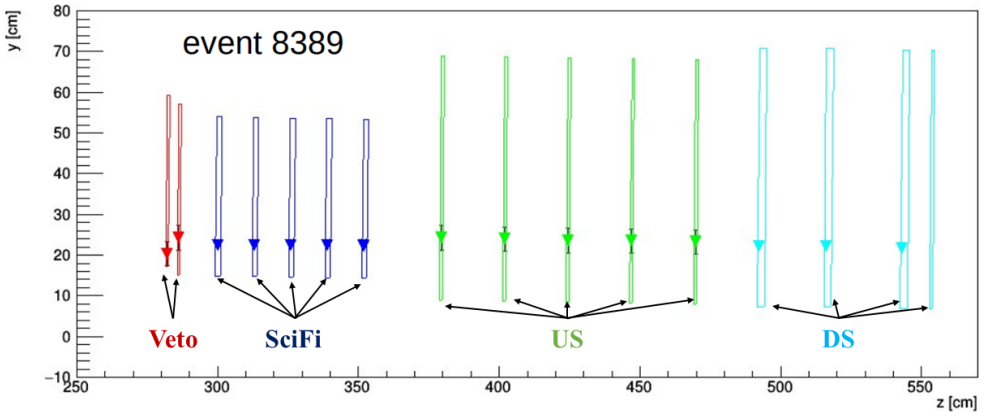

Figure 3.5: Event display (side view) of a simulated passing-through muon in SND@LHC.

The first part of the present thesis work was devoted to the development of an updated event display, which included both passive materials and a realistic implementation of the detector response. From the July 2022 it was adopted as official display for the SND@LHC Collaboration. An example of the devloped 2D display for a passing-through muon is shown in Figure 3.6. Following the TGeo file containing the geometry of the detector, several upgrades were impelemnted in order to easily visualize what happens inside the detector for each recorded event:

1. nine passive iron blocks in the muon system, coloured in green as in the real detector;
2. five target walls interleaved with the SciFi planes, coloured in grey as in the real detector;
3. aluminium frames over the veto and the muon system, coloured in light grey so as not to clutter the view;
4. seven horizontal scintillating bars in the veto, visible only in the side view;
5. ten horizontal scintillating bars in the upstream system, visible only in the side view;
6. sixty small horizontal scintillating bars in the downstream system, visible only in the side view;
7. sixty small vertical scintillating bars in the downstream system, visible only in the top view;

8. SciFi hits are drawn as blue circles, due to the fine granularity of the fibre modules readout;

9. veto, upstream and downstream hits are no longer drawn as points (triangles), but rather the whole active volume (scintillating bar) is highlighted in black (muon system) or red (veto);

10. info box in the bottom left corner of each view, including the experiment logo, the event identification and the timestamp converted in GMT time.

The tracking feature, whenever possible, is based on Hough transform [62].

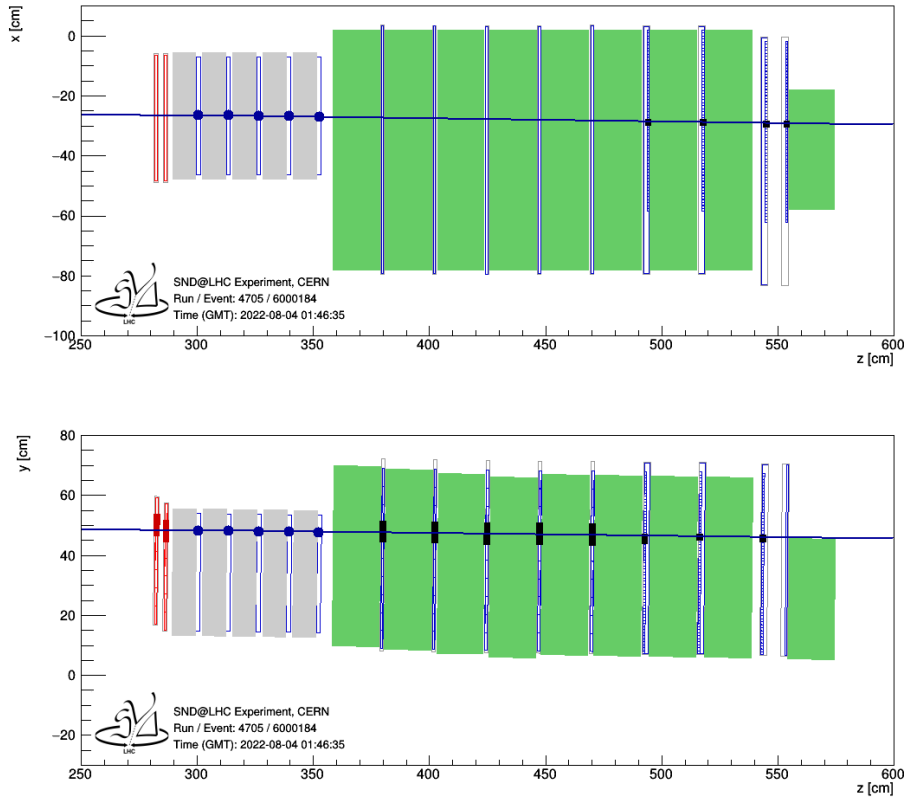

Figure 3.6: Official event display of SND@LHC. A penetrating muon event is displayed, firing all the electronic detectors.

The detector coordinate system in Figure 3.6 is arranged such that the origin of the axis correspond to the pp collision axis. Thus, the geometry lays on positive ascending y values and negative decreasing x coordinates. An event display of one of the eight muon neutrino candidates observed in 2022 Run is reported in

Figure 3.7. Electromagnetic showers can be seen in the SciFi, after the interaction occurred in the third target wall, and hadronic activity in the upstream system, along with a passing-through muon track in the Downstream System.

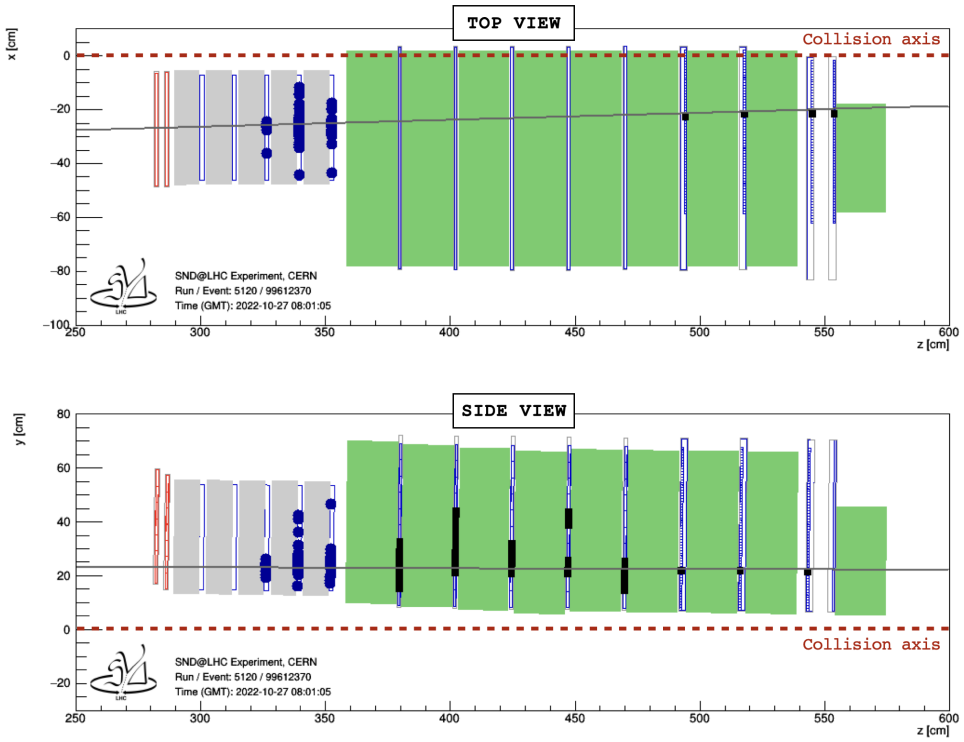

Figure 3.7: Event display of a candidate ν_μ interaction. Proton-proton collision axis is illustrated with the red dashed line.

Chapter 4

Data reconstruction

The event reconstruction is performed at first during the data taking using the response of the electronic detectors, and later incorporating the emulsion data, that are available after the extraction, development, scanning and analysis of emulsion films. The SND@LHC experiment has been taking data successfully during the proton physics run of 2022, from April to November. In the report shown in Figure 4.1 a total integrated luminosity of $39.0\,\mathrm{fb}^{-1}$ have been delivered at ATLAS in 2022, and $37.6\,\mathrm{fb}^{-1}$ ($\sim$ 96 %) have been recorded by SND@LHC electronic detectors. The emulsion target replacements are identified as "emulsion RUNs", and represented in Figure 4.1 with the coloured lines. The summary of the luminosity integrated in each emulsion RUN is reported in Figure 4.2, along with the instrumented target mass. The first LHC Run 3 stable beams at $6.8\,\mathrm{TeV}$ were delivered at the beginning of July 2022.

4.1 Emulsion scanning system

The emulsion readout is performed in dedicated laboratories equipped with automated optical microscopes, derived from the European Scanning System [13, 15], as the one shown in the left panel of Figure 4.3. The microscopes have been continuously upgraded, both in hardware and software [33, 38, 41]. The scanning speed, measured in terms of film surface per unit time, was significantly increased [41], more than a factor ten faster than before. R&D is still ongoing [48] to further increase it.

To make a scanning the emulsion film is placed on a movable stage around the surface (xy plane). The microscope moves along the whole thickness of the emulsion (z coordinate) in order to capture tomographic images at different depths of the emulsion layer, thus the three-dimensional structure of the track can be reconstructed. The lens of the microscope guarantees a sub-micron resolution and

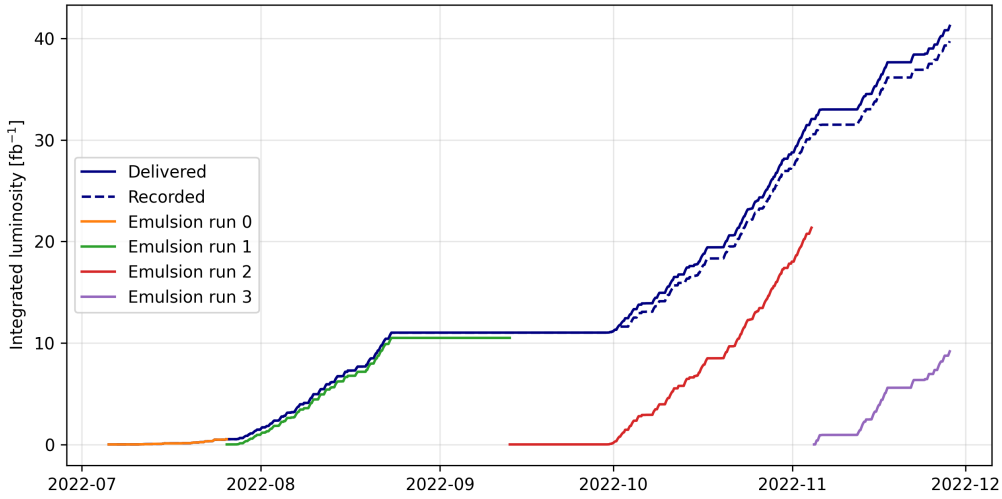

Figure 4.1: Integrated luminosity in ATLAS [68]. Dashed line is the luminosity recorded at the SND@LHC electronic detectors; emulsion RUNs exposure are reported as coloured lines. Values displayed are not corrected for a $6\,\%$ recent reduction.

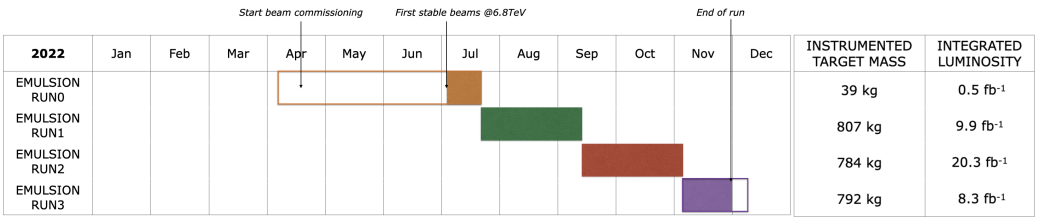

Figure 4.2: Emulsion RUNs replacement timeline. Details on instrumented mass and integrated luminosity of each RUN.

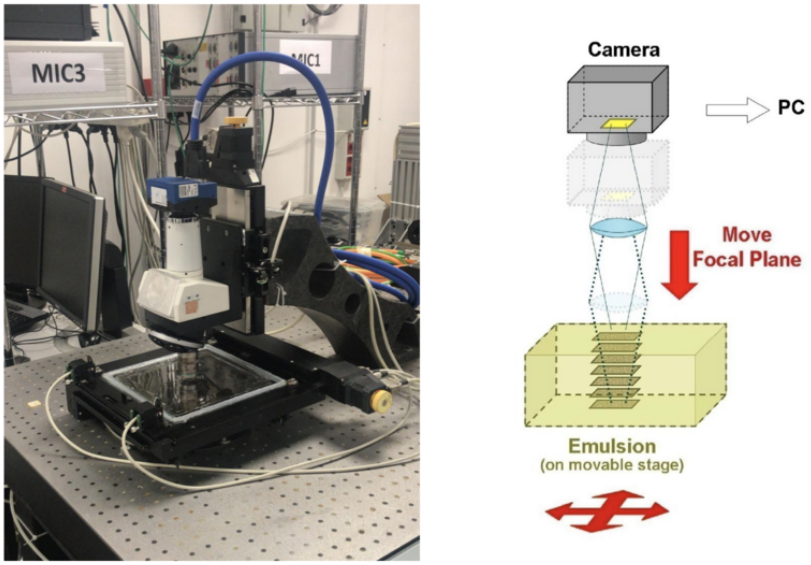

Figure 4.3: (Left) Optical microscope used for the SND@LHC emulsion film scanning. (Right) Schematic drawing of the scanning procedure [61].

allows for a scan of both sides of the emulsion film. In order to make the optical path homogeneous in the film, an immersion lens in an oil with the same refraction index of the emulsion is used. A single field of view is $800 \times 600\,\mu\mathrm{m}^2$. Larger areas are scanned by repeating the data acquisition on a grid of adjacent fields of view, starting from the bottom left corner of the film as the xy origin. The total emulsion film surface to be scanned in SND@LHC is expected to be about $44\,\mathrm{m}^2$ for each target replacement. Emulsion films are labeled by handwriting as in Figure 4.4:

1. Run number
2. Wall number
3. Brick number
4. Plate number
5. Film manufacturer

Currently, the emulsion are being scanned in five scanning stations in Europe: two microscopes are located in Naples, one in Bologna, one in Lebedev, and the last one has been recently installed in the CERN emulsion facility. RUN0 has been already completely scanned and processed in Naples. Films from other emulsion RUNs have been equally shared between all the laboratories, that are now performing the scanning and the analysis of RUN1 emulsion films.

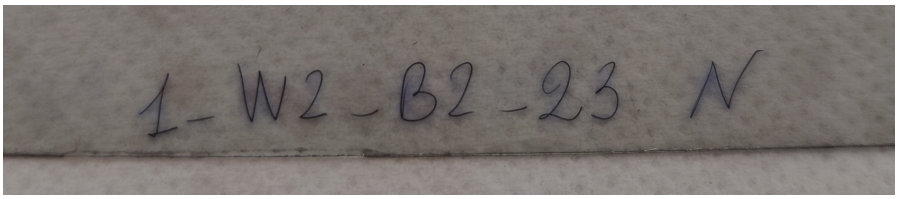

Figure 4.4: Label of the emulsion film. From left to right: RUN number, wall number, brick number, plate number, manufacturer.

4.2 Emulsion RUN0 reconstruction

The first months after the detector installation were characterized by the beam commissioning and scrubbing, with low integrated luminosity. Therefore, in order to optimize the nuclear emulsion usage, only one brick out of twenty was instrumented with 57 Nagoya emulsion films from April 7th to July 26th, the remaining ones being filled with tungsten only. A layout of this configuration, referred to as "Emulsion RUN0", is shown in Figure 4.5. The integrated luminosity of this exposure amounts to $0.5\,\mathrm{fb}^{-1}$. Such a choice was made so as to evaluate the performance and the limits of the data reconstruction, starting from the emulsion scanning, throughout the whole reconstruction algorithms. The Emulsion RUN0 was also used to test for the first time the effect of long-term contact of emulsion films with tungsten.

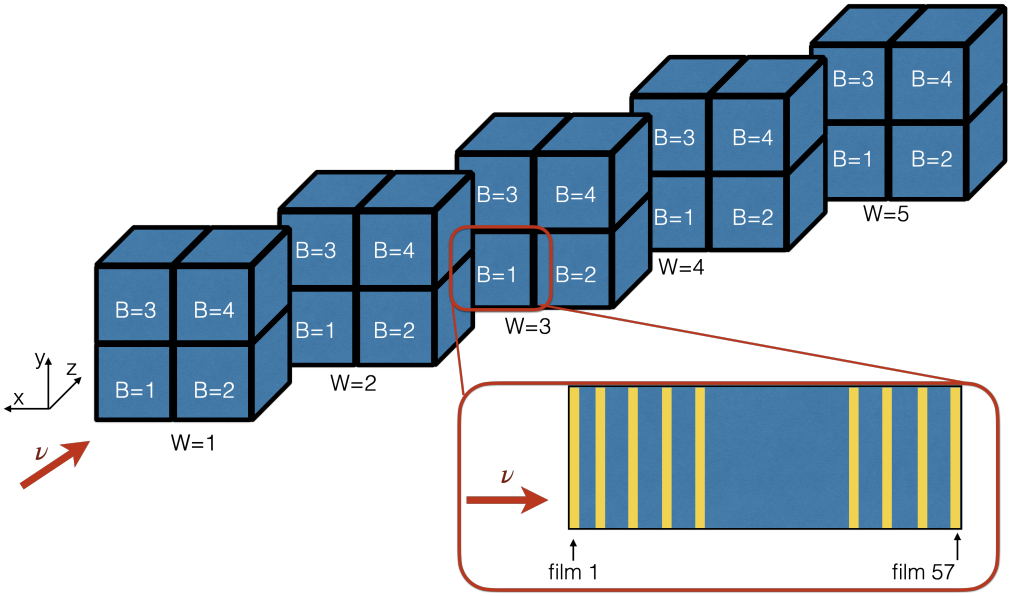

Figure 4.5: Layout of the SND@LHC emulsion target. The brick instrumented for RUN0 is highlighted, showing its inner films structure.

4.2.1 Linking

The reconstruction of the emulsion data starts during the scanning procedure. After digitizing the acquired images an image processor recognizes the grains as clusters, formed by groups of pixels of a given size and shape. Therefore, the track in the emulsion layer (usually referred to as *micro-track*) is obtained by connecting clusters belonging to different levels, as shown in the left panel of Figure 4.6. The offline reconstruction tools used are developed in FEDRA (Frame-work for Emulsion Data Reconstruction and Analysis) [17], an object-oriented tool based on C++ and developed in the ROOT [7] framework. Given that the emulsion films are formed by two emulsion layers, micro-tracks reconstructed in the two emulsion layers are linked together to form the *base-track* (or *segment*), representing the particle trajectory in a single film, as illustrated in the right panel of Figure 4.6.

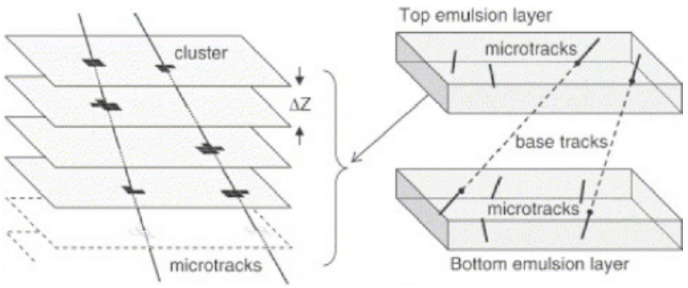

Figure 4.6: Schematic reconstruction of scanned emulsion information. (Left) Reconstruction of micro-tracks from digitized clusters. (Right) Reconstruction of base-tracks from two matched micro-tracks.

This procedure is therefore called *linking*, and it is divided in two steps. The first-linking evaluates the *shrinkage*, the angular corrections to apply to micro-tracks during the second-linking. Base-tracks are chosen according to a χ^2 minimization, using coordinates, angles and cluster number as input [67]. The emulsion films in this brick show uniform base-track density along the surface, as shown in Figure 4.7. The angles of the base-track are here referenced as their components in the xz (TX) and yz (TY) plane.

4.2.2 Alignment

Angles and positions of the base-tracks are provided in the local reference of each film, the z axis being centered in the middle of the plastic base. The reconstruction of particle tracks in the full volume requires connecting base-tracks in consecutive films. A global reference system for the whole brick is obtained by aligning pairs

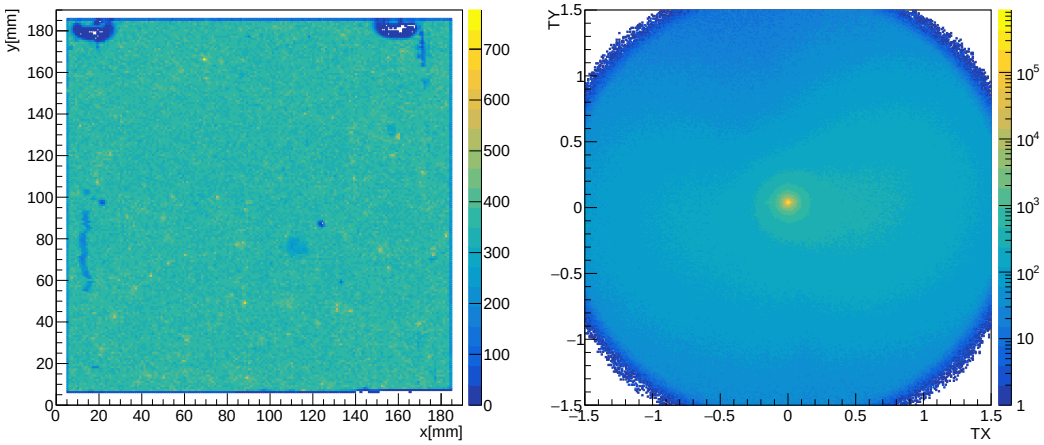

Figure 4.7: Two-dimensional spatial (left) and angular (right) distribution of base-tracks reconstructed in one of the films exposed in the Emulsion RUN0.

of consecutive films one with respect to the other, and this system is then used for track reconstruction in the whole brick. In order to define such a global reference system, a set of affine transformations is computed to account for the different reference frames used for data taken in different films. Penetrating muon tracks are mainly used for fine film-to-film alignment. It is convenient to optimize the alignment parameters on a small area first, then moving to the whole scanned area, usually with 3 alignment iterations.

4.2.3 Tracking

Once all emulsion films are aligned, track reconstruction merges the base-tracks in the brick's emulsion films, in order to reconstruct the trajectory of the particle in the target, usually referred to as *volume-track*. The employed algorithm is a Kalman Filter developed in FEDRA, and seeded on the base-tracks, that fits the best track estimation at given z for each measured (real) segment [67]. A 3D display of reconstructed tracks can be built, drawing the trajectories of the particles traversing the emulsion films. An example with 82 reconstructed tracks, starting from a surface of $1\,\mathrm{mm}^2$ around the emulsion film center, is shown in Figure 4.8.

One of the purposes of the track reconstruction is to identify neutrino interaction, ideally connecting the information obtained by the SciFi plane immediately downstream of the target wall. Therefore the alignment and the tracking procedures are performed backwards, so as to reconstruct events from the downstream signal to the interaction vertex. Vertex reconstruction is

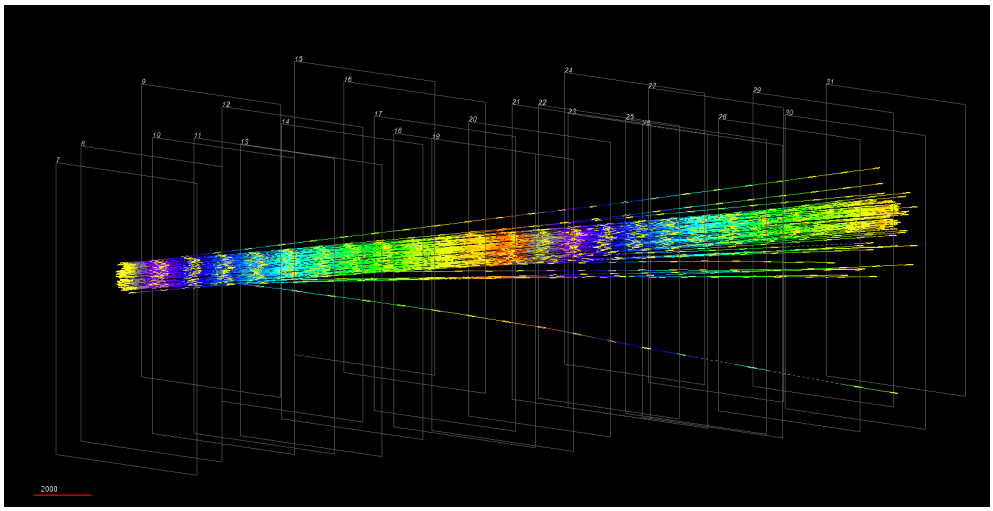

Figure 4.8: Track display in 25 films, starting from 1 mm^2 around the emulsion film center. The colors represent base-tracks in the different emulsion films of the target.

eventually performed through a Kalman Filter by connecting reconstructed tracks, based on angles and positions. The FEDRA reconstruction provides information on a χ^2 probability, along with the interaction point position and characterization.

4.2.4 Muon flux measurement

The proton collisions produce, among the other particles, penetrating muons, which arrive at the detector, placed at $480\,\mathrm{m}$ distance from ATLAS impact point. A precise measurement of this muon flux allows to validate Monte Carlo simulations and to accurately describe emulsion occupancy, providing input in planning next emulsion target replacements and data analysis.

Considering the data analyzed from 25 emulsion films of the RUN0 exposure, the number of associated segments in each track is shown in the left panel of Figure 4.9. Two components might be evinced: a random combinations contribution at low number of segments, decreasing into interrupted or absorbed tracks and, after a plateaux, a rising component due to penetrating tracks. Tracks with at least 18 segments are evaluated as particles passing through the target, in the guise of muons. The efficiency of each emulsion film can be measured by considering passing-through particles, expected to have segments in all films in the analyzed target section. Therefore, the ratio between found segments and expected segments is an estimation of the efficiency for each film, shown in the right panel of Figure 4.9, with an average of $(93.1 \pm 0.6)\,\%$.

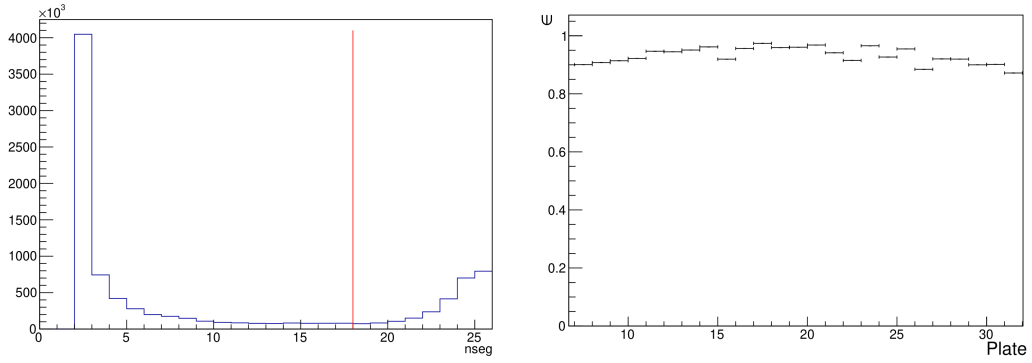

Figure 4.9: (Left) Number of segments reconstructed in the tracks, with the red line showing the required minimum number of segments. (Right) Efficiency of track reconstruction for each film.

The muon flux measurement was performed by assessing the reconstructed track density in $1 \times 1\,\mathrm{cm}^2$ cells over the entire film area, having corrected it by the probability to have at least 18 segments in 25 films, estimated with the cumulative binomial probability. A 2D map of such track density cells is shown in Figure 4.10, where 2 cells have been excluded each side so as not to account for reconstruction inefficiencies on the borders. An average density of $(7.7 \pm 0.6) \times 10^3\,\mathrm{cm}^{-2}$ was measured in the region represented within the red border. Given the luminosity integrated in the analysed sample, the resulting muon rate is $(1.5 \pm 0.1) \times 10^4\,\mathrm{fb}^{-1}/\mathrm{cm}^2$. This emulsion data is consistent with the independent measurements of the electronic detectors within 10%. The results are currently being used to validate Monte Carlo simulations of the muon flux produced at the LHC in the detector region.

4.2.5 Local reconstruction

A dedicated test of track reconstruction with tighter alignment constraint has been performed for the same 25-films sample in five small $1\,\mathrm{cm}^2$ areas, on the center of the emulsion films and the others in four equally spaced regions, referred as *quadrants*. Focusing on small areas for the determination of alignment parameters allows for reducing the effect of angular distortions and emulsion surface deformations. The left panel of Figure 4.11 shows the number of segments associated to reconstructed tracks for the four different quadrants. One could also look at the number of emulsion films crossed by a particle, without requiring to observe a base-track in each film. Such a information is visible in the right part of Figure 4.11, in which the majority of the tracks are clearly passing through all the 25 plates.

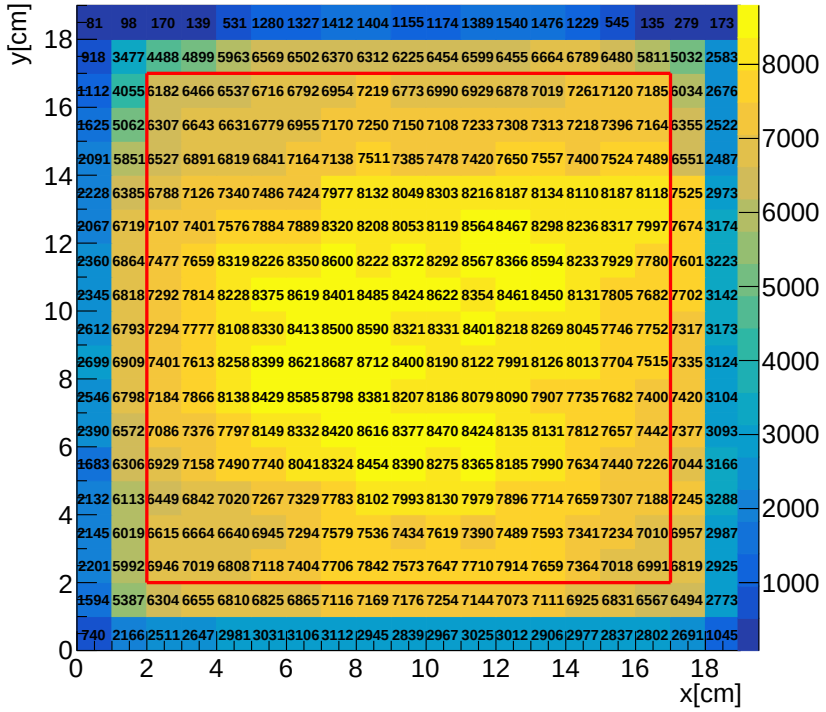

Figure 4.10: Position distribution of reconstructed tracks in $1 \times 1\,\mathrm{cm}^2$ cells, corrected for reconstruction efficiency. The red border represents the region considered for measuring the average density.

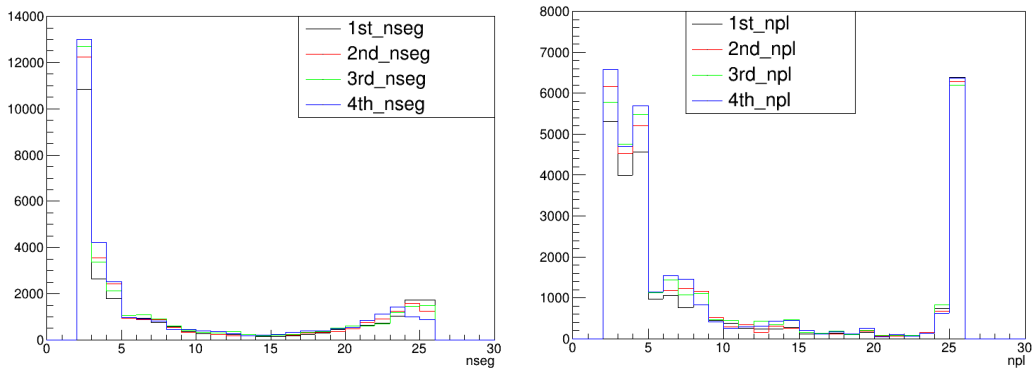

Figure 4.11: (Left) Number of segments reconstructed in the tracks, for the four small region analyzed. (Right) Number of films crossed by the reconstructed track.

Computing the residuals between position and angle of each base-track with a linear fit on the xz and yz planes leads to a measurement of the tracking resolution. Figure 4.12 and 4.13 show respectively the position and the angular residuals in both 2D spatial projections of the $1\,\mathrm{cm}^2$ area around the center. Resolutions are evaluated as the width of a two-model gaussian fit on the residual distributions. Values are reported in Table 4.1, nearly halving the values obtained from the global reconstruction. Resolutions measured for all the quadrants are rather similar.

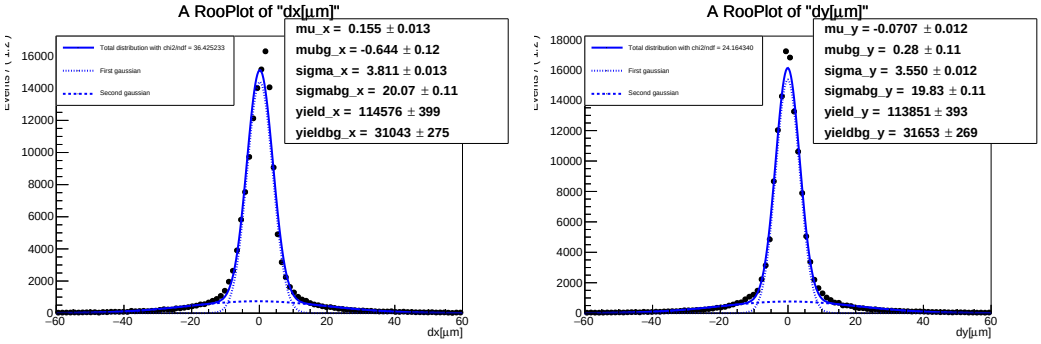

Figure 4.12: Position residual distributions. (Left) x component and (right) y component.

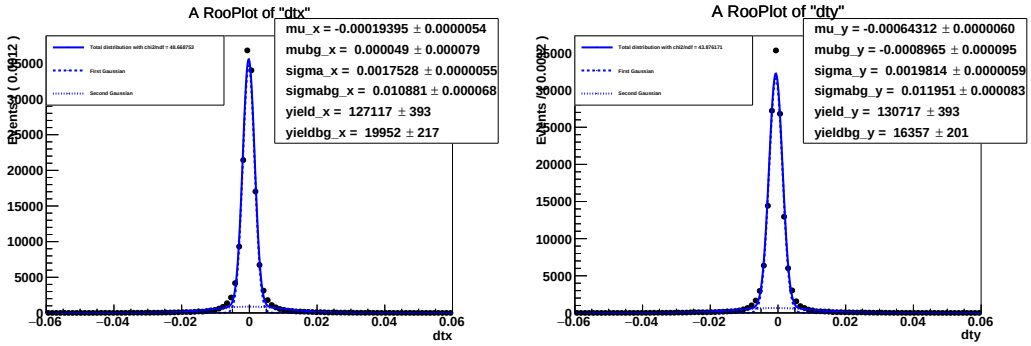

Figure 4.13: Angular residual distributions. (Left) xz projection and (right) yz projection.

Reconstruction	Position resolution		Angular resolution	
	σ_x	σ_y	σ_{tx}	σ_{ty}
Global	$5.9\,\mu m$	$7.3\,\mu m$	$2.7\,mrad$	$2.5\,mrad$
Local	$3.8\,\mu m$	$3.6\,\mu m$	$1.8\,mrad$	$2.0\,mrad$

Table 4.1: Position and angular resolutions measured with tracks reconstructed in the whole surface (global reconstruction) and in the $1\,cm^2$ area around the center of the film (local reconstruction).

4.3 Emulsion RUN1 scanning and reconstruction at CERN

In the early 2023 a new scanning laboratory was installed at CERN, in the building 162. Part of my thesis work has been carried out at CERN for two months, where I was assigned as the scanning station responsible. After having dealt with the system configuration and scanning tests at the new microscope, emulsion films scanning were regularly held. From my experience in the Naples laboratory, I was able to give instructions and train other personnel committed to the scanning process. Moreover, the data management phase on servers and its reconstruction was also handled by myself through a dedicated account for the laboratory.

The scanning and reconstruction of emulsion RUN1 films was firstly performed in Naples. Problematics arose from the high track density (~ 20 more than RUN0), hence a huge effort was made in order to optimize the software parameters. The use of GPU instead of CPU was also implemented to speed up the scanning.

The first compelling task to achieve in the new CERN scanning station was a consistency test with another laboratory. The parameters of RUN1 films scanning have been set equals to Naples microscopes ones. The base-tracks reconstruction between the two emulsion layers was performed in an innovative way, splitting the emulsion surface in $1 \times 1\,cm^2$ cells, with an overlapping region of $25\,\%$. The linking of such cells has been accomplished by parallelizing the process via HTCondor [66], a software system that creates a High-Throughput Computing (HTC) environment and effectively uses the computing power of machines connected over a network, sharing resources with distributed ownership.

Therefore, it was feasible to compare both the scanning and the linking performances of the two laboratories. As a matter of fact, it was recorded a significant speed up in the linking, being made on 18×18 parallel cells of $1\,cm^2$

instead of one surface of $18 \times 18\,\mathrm{cm}^2$[1]. Nonetheless, the algorithm for merging the individual cells delays the process, and hence it is currently under further improvement. The results of the linking are shown in Figure 4.14, where we can distinguish some of the cell structure in the left panel. After some basic cuts defining good quality segments, the base-tracks densities registered in both laboratories, and reported in Table 4.2, are consistent. In addition, a clear pattern of increasing density rising in y coordinate, due to the fact that muon flux increases as the distance from the beamline increases.

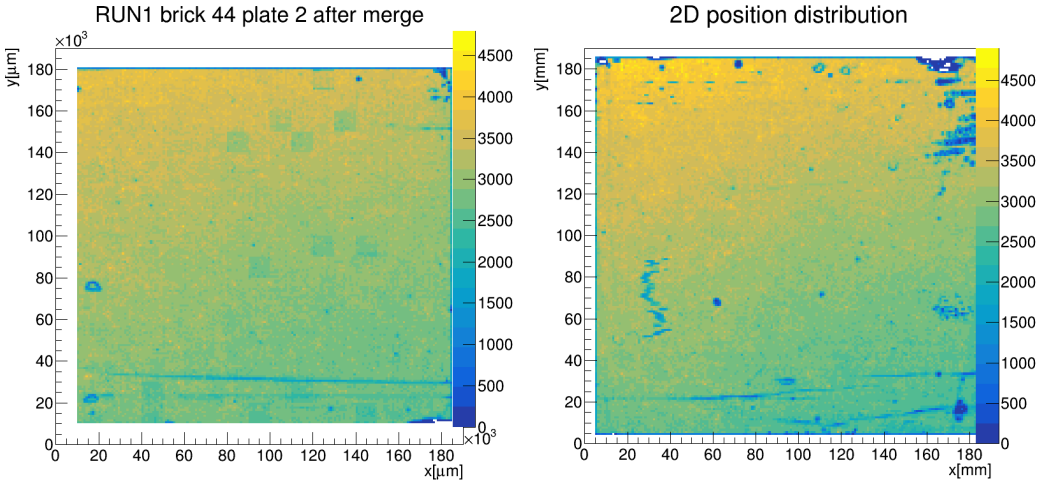

(a) 1_W4_B4_2 (b) 1_W2_B4_2

Figure 4.14: Comparison of two-dimensional position distribution of reconstructed segments in two different scanning laboratories, CERN (a) and Naples (b). Color scales are normalized to the same value.

4.4 Emulsion RUN2 scanning and reconstruction test

A striking test was made on RUN2 as well. The first scans of RUN2 films, performed at the CERN facility, gave a significant outcome, which can be foreseen in Figure 4.15. RUN2 collected $20.3\,\mathrm{fb}^{-1}$ of data, twice the RUN1 integrated luminosity. Considering that, the values reported in Table 4.2 imply that the segment density scales with the luminosity as expected.

[1]The outer $5 - 10\,\mathrm{mm}$ frame of the $192 \times 192\,\mathrm{mm}^2$ is not scanned due to the mechanical limit switches of the microscopes.

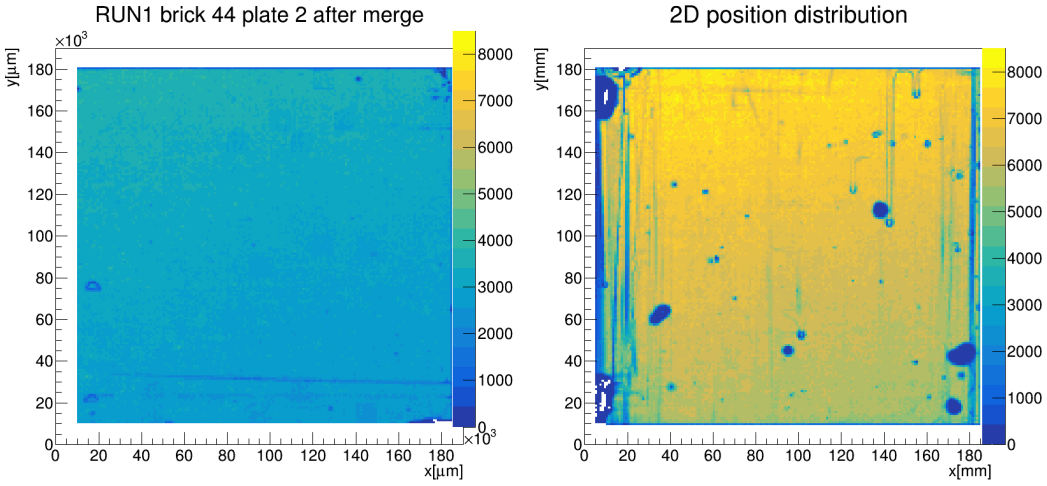

(a) 1_W4_B4_2 (b) 2_W3_B4_1

Figure 4.15: Comparison of two-dimensional position distribution of reconstructed segments in RUN1 (a) and RUN2 (b). Color scales are normalized to the same value.

Emulsion film	Scanning station	Base-track density (cm^{-2})	Base-track density normalized (cm^{-2}/fb^{-1})
1_W2_B4_2	Naples	311553	31470
1_W4_B4_2	CERN	305727	30881
2_W3_B4_1	CERN	604158	29761

Table 4.2: Reconstructed base-track density comparison between different scanning stations and RUNs.

Ultimately, Figure 4.16 shows the profiles of the x and y segment distributions for RUN0, RUN1, and RUN2. The base-track density scales consistently with the integrated luminosity. In the right panel it is also noticeable how the muon flux increases with the increasing y coordinate for the RUN1 (magenta line) and RUN2 (black line) brick 4.

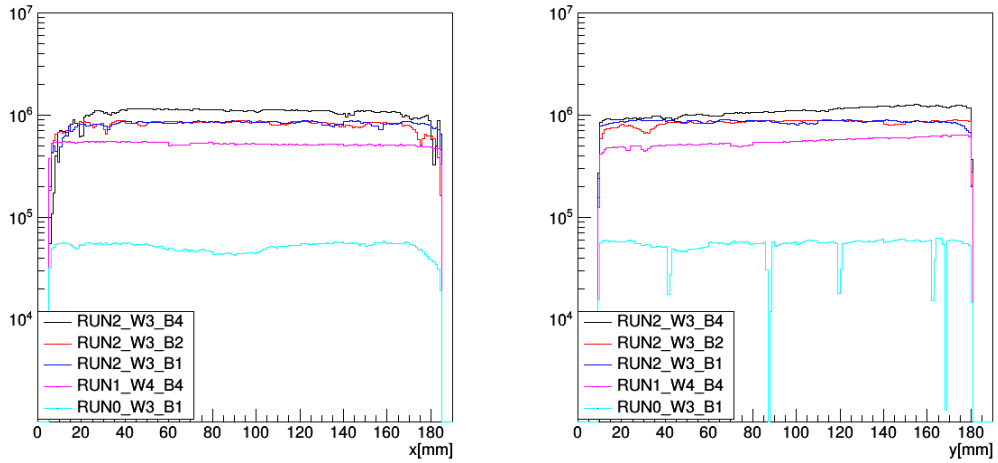

Figure 4.16: One-dimensional segment position distributions, (Left) x and (Right) y coordinates.

The described test on emulsion RUN2 was of great importance in view of the upcoming target RUNs, thus the maximum exposure time. It allowed for evaluating the current limits on scanning speed and reconstruction memory consumption, pointing a direction for the R&D improvements both in hardware and in software.

Chapter 5

Vertex reconstruction

The Emulsion Cloud Chamber of SND@LHC operates as a tracking device capable of detecting particles interacting in the target by distinguishing different topologies. The fine segmentation of active emulsion films interleaving tungsten plates enables a vertex detection with micrometric resolution. The main rask of the emulsion reconstruction is to identify neutrino interactions by measuring the trajectory of all the charged particles produced, thus reconstructing the interaction vertex. Vertex reconstruction is performed in FEDRA [17] with a Kalman Filter seeded on the segments of reconstructed tracks.

Nonetheless, the following study aims to characterize the background in order to optimize the rejection process, as less than one neutrino event is expected in the RUN0 exposure. Muon-induced interactions represent the main background. Undetected incoming muon track and the subsequent muon DIS or electromagnetic activity are able to produce the same neutrino signature, with a charged lepton (μ) and hadrons (X) in the detector acceptance. Moreover, neutral interactions might be resembled by muons coming from the decay in flight of neutral hadrons, being induced by muons outside the detector.

The first-ever vertex reconstruction in SND@LHC emulsion data has been performed considering the most 31 upstream emulsion films in the emulsion RUN0 brick, starting from plate 4 to plate 34. Figure 5.1 shows how complex is the search for neutrino vertices: about 80 vertices are reconstructed using volume-tracks starting in a $1 \times 1\,\mathrm{mm}^2$ surface. It is noticeable that a couple of vertices are reconstructed by extrapolating tracks outside of the sample volume.

Given the large amount of data contained in the brick, the reconstruction was divided in multiple processes, eventually merging the outcome. The emulsion film scanned surface is $180 \times 180\,\mathrm{mm}^2$. However, in order to perform the tracking avoiding time and computing consumption, tracks have been reconstructed in four different areas separately, arranged as in the left panel of Figure 5.2. Each *quadrant* is $96 \times 96\,\mathrm{mm}^2$, considering 5% surface overlap so as

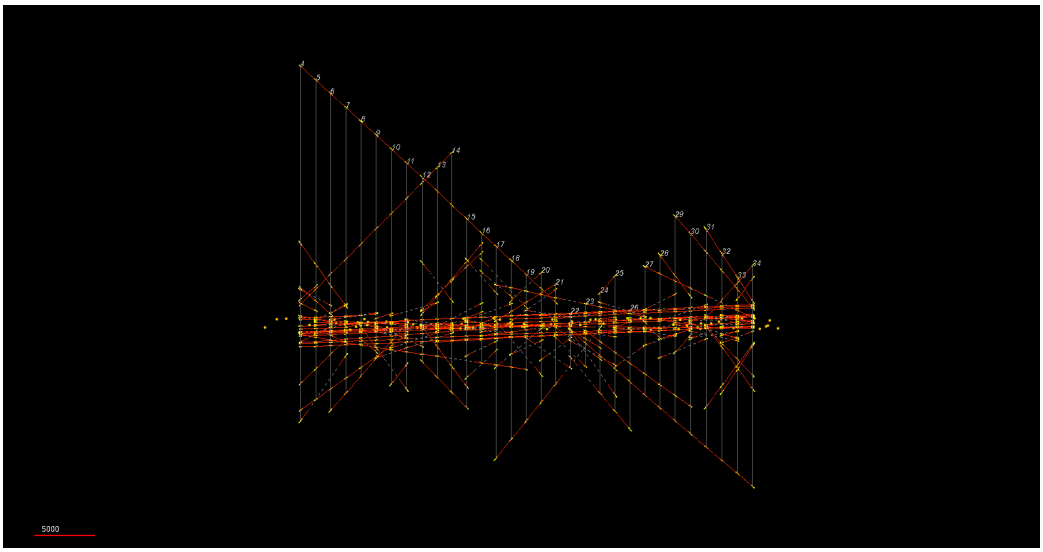

Figure 5.1: 3D display of vertices reconstructed in $1\,\mathrm{mm}^2$ in 31 films.

to take border effects into account. Tracks in the overlap region are taken once. Furthermore, the vertex reconstruction algorithm was performed dividing quadrants in *subquadrants* of $53 \times 53\,\mathrm{mm}^2$, as illustrated in the right panel of Figure 5.2. In the $10\,\%$ region overlap vertices are considered once.

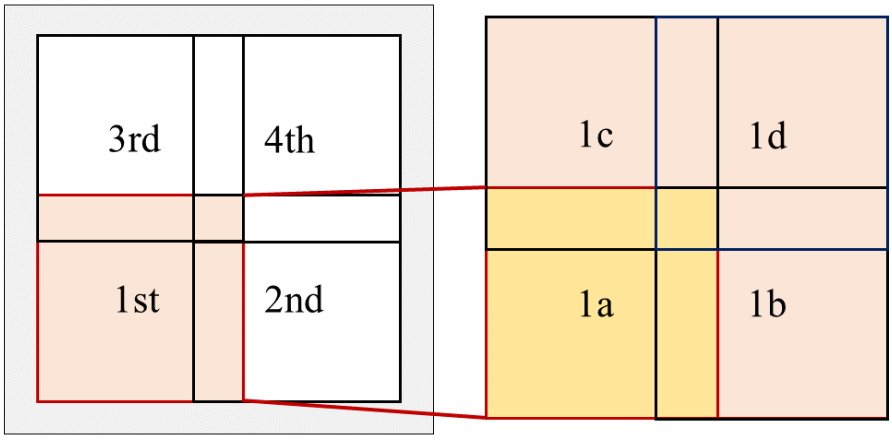

Figure 5.2: (Left) Illustration of an emulsion film divided in four tracking regions. (Right) Highlight of one region divided in turn in four vertexing areas.

5.1 Vertex selection

The overall number of vertices reconstructed in the sample is $\sim 3 \times 10^6$. Before analyzing them, several cuts based on vertex topologies are applied.

Vertex position In addition to vertices reconstructed inside the target volume, extrapolations of tracks might connect into a vertex outside the target. Therefore, the first selection cut concerns the fiducial volume where the neutrino interaction can occur. Transverse coordinates of the emulsion film are accounted for during the subquadrants merge. The z distribution of the reconstructed vertices is shown in Figure 5.3, with the vertical red lines defining the upstream and downstream surfaces of the analyzed volume. Only vertices lying inside the analyzed volume are considered.

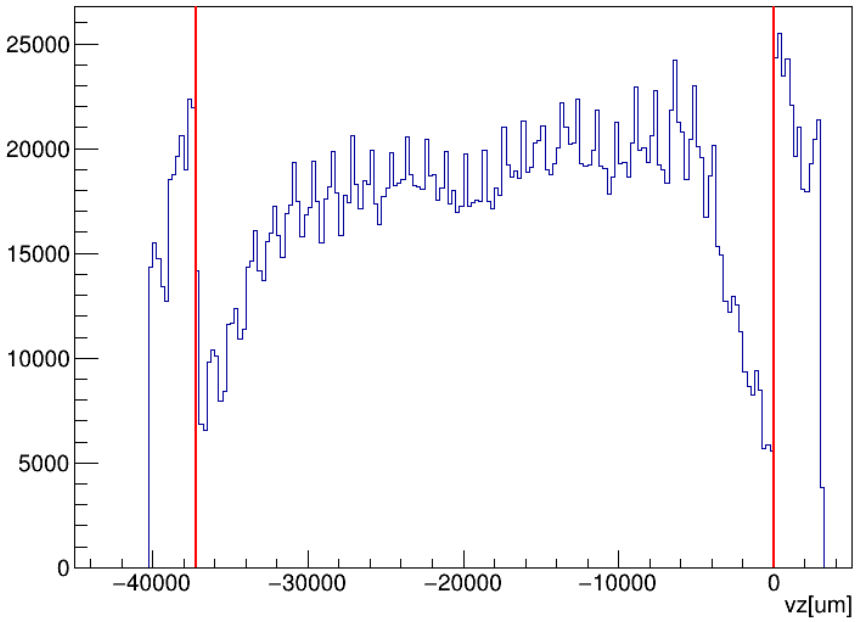

Figure 5.3: Reconstructed vertices position along the target z-axis. The volume of the analyzed sample is indicated with the two red lines.

Flag Vertex topologies in Figure 5.4 are identified by means of a flag [67]:

- flag 0 (3) identifies forward neutral vertices;
- flag 1 (4) identifies forward charged vertices;
- flag 2 (5) identifies backward neutral vertices;

with the flag in the parenthesis adding the information that vertex has at least one track in common with another vertex.

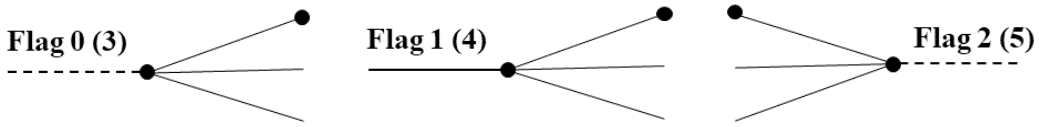

Figure 5.4: Vertex topologies. From left to right: neutral (linked), charged (linked), back neutral (linked).

Flags of reconstructed vertices are shown in Figure 5.5. Neutrino-like vertices are those with flag 0 or 3. Forward charged vertices (flag 1 or 4) can be attributed to a Deep Inelastic Scattering of muon in the target volume, as shown in Figure 5.6.

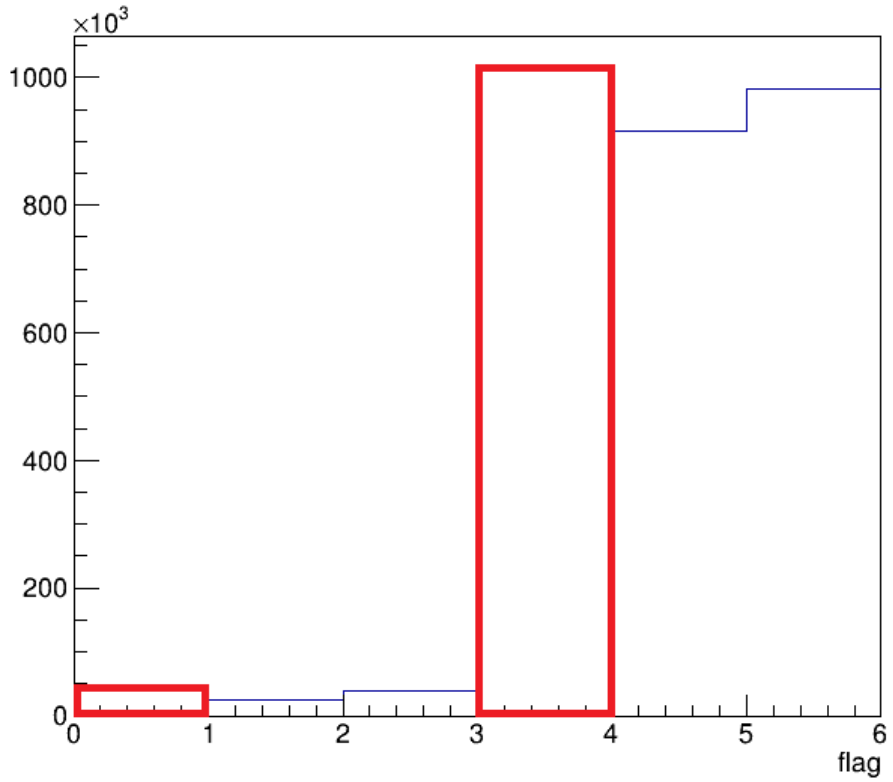

Figure 5.5: Flag distribution of the reconstructed vertices. Selected vertices are with flag 0 or 3.

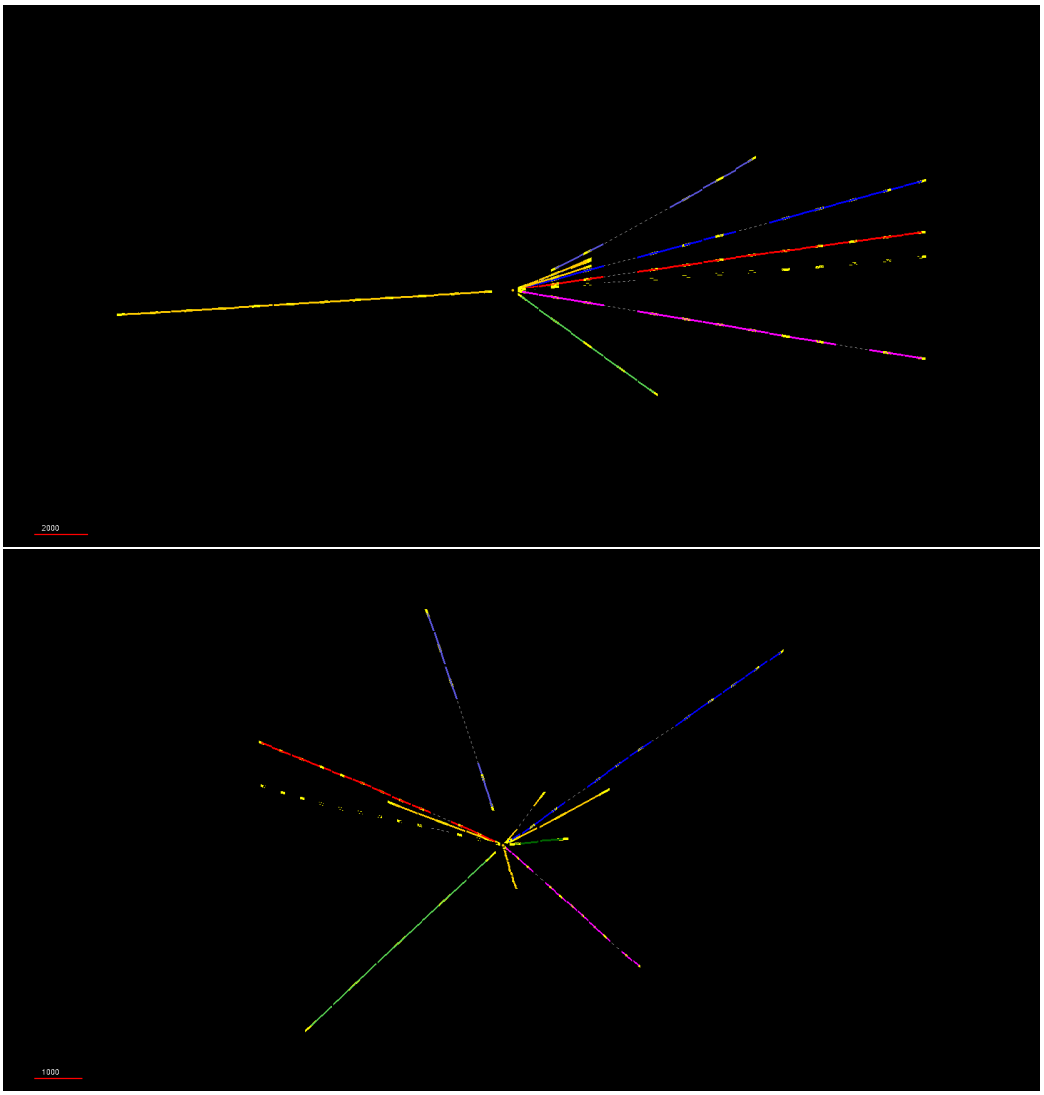

Figure 5.6: 3D vertex display of a RUN0 candidate muon DIS (top) y projection (bottom) z projection.

Vertex multiplicity Neutrinos interacting via Deep Inelastic Scattering in the target are expected to produce on average 5.8 tracks in the interaction vertex. Such high multiplicity is due to the mean energy of the DIS neutrinos. The multiplicity of reconstructed vertices in RUN0 data is reported in Figure 5.7. Vertices with less than three tracks are discarded based on Monte Carlo studies about muon DIS background. A large contribution to the low multiplicity vertices is likely due to combinatorial random association in a such high track-density environment. One of the vertices with high multiplicity is shown in Figure 5.8, and it might be interpreted as a high-energy hadronic shower.

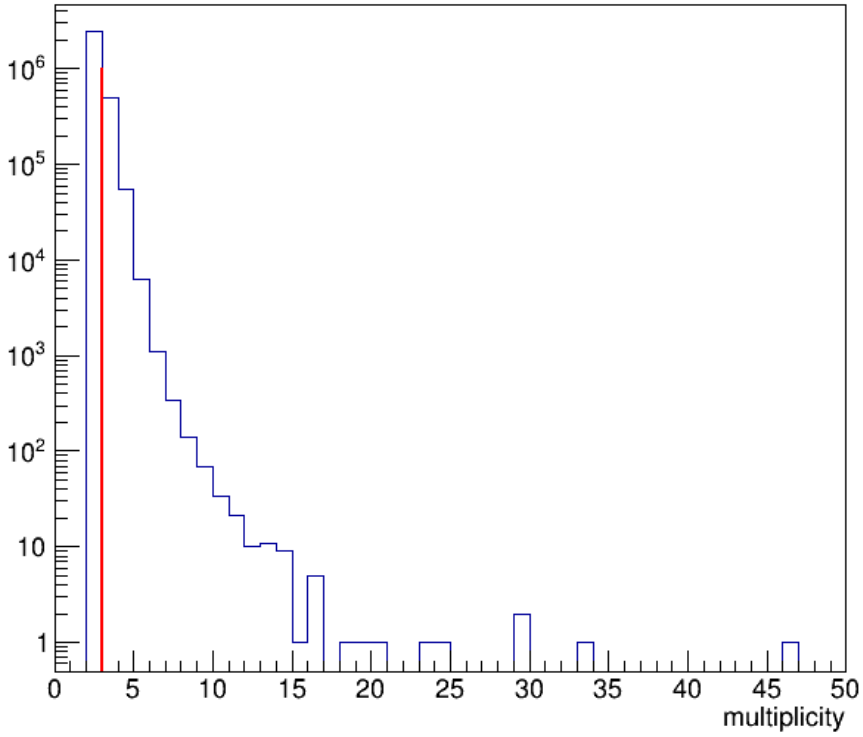

Figure 5.7: Vertex multiplicity. Selected vertices are with at least 3 tracks.

After having applied the discussed selections, ~ 80000 reconstructed vertices survive. A summary of the selection efficiencies is reported in Table 5.1, showing the rejection power of the described cuts. Selection efficiencies of Monte Carlo samples are also addressed: signal MC sample is composed of $\sim 1400\,\nu_\mu$ CC-DIS interaction, and background MC sample is provided with muons with a track density of $10^4\,\mathrm{cm}^{-2}$, according to the measured muon flux in Section 4.2.4. The FEDRA tracking and vertex reconstruction is performed in the whole target on Monte Carlo samples starting from simulated base-tracks, and the same vertex selection procedure is applied in order to compare simulations and data.

The main discrepancy between the total efficiency of data and simulated background might be ascribed to the multiplicity cut. The larger statistics of RUN0 reconstructed data and the sizeable contribution from the combinatorial random associations increase the multiplicity rejection, thus lowering the efficiency.

Selection	RUN0 data eff (%)	MC bkg eff (%)	MC signal eff (%)
All sample	3022809	13481	1374
Position	84.29 ± 0.02	76.0 ± 0.4	98.8 ± 0.3
Flag	33.21 ± 0.03	40.7 ± 0.5	99.8 ± 0.1
Multiplicity	9.45 ± 0.03	26.5 ± 0.7	88.3 ± 0.9
Total efficiency	2.646 ± 0.009	8.2 ± 0.2	87.8 ± 0.9

Table 5.1: Number of vertices in the analyzed samples and partial efficiencies for the three selections applied on RUN0 data, MC background and MC signal. Total efficiency is reported in the last raw.

5.2 Vertex characterization

The integrated luminosity of emulsion RUN0 exposure amounts to $0.5\,\mathrm{fb}^{-1}$, hence less than one neutrino event is expected. As a matter of fact, the purpose of the first emulsion target was to assess the FEDRA reconstruction algorithms for SND@LHC and to optimize them, in view of the subsequent emulsion RUNs replacements. Therefore, it is reasonable to regard the RUN0 reconstructed data as background only, thus characterizing it and evaluating the background rejection. In order to perform the validation, a comparison between RUN0 data and Monte Carlo background was performed for variables characterizing the vertex, considering the reconstruction of the mentioned MC sample only in the most 31 upstream films of the same brick of RUN0. Vertex selection is done in the similar way as described above.

The multiplicity of the selected vertices is shown in Figure 5.9. RUN0 data and MC background are superimposed in the left panel, resulting in a similar decreasing behaviour, except for high multiplicity owing to the low MC statistics. The right panel shows the expected distributions for the signal. A Monte Carlo ν_μ CC-DIS sample, reconstructed in the whole target, is considered. As mentioned, the peak is around $5 - 6$ tracks per neutrino vertex, with tails at higher multiplicities.

Figure 5.10 shows a 3D vertex display of one of the vertices selected in RUN0 data . Since the vertex is reconstructed in the 13th plate, no charged tracks

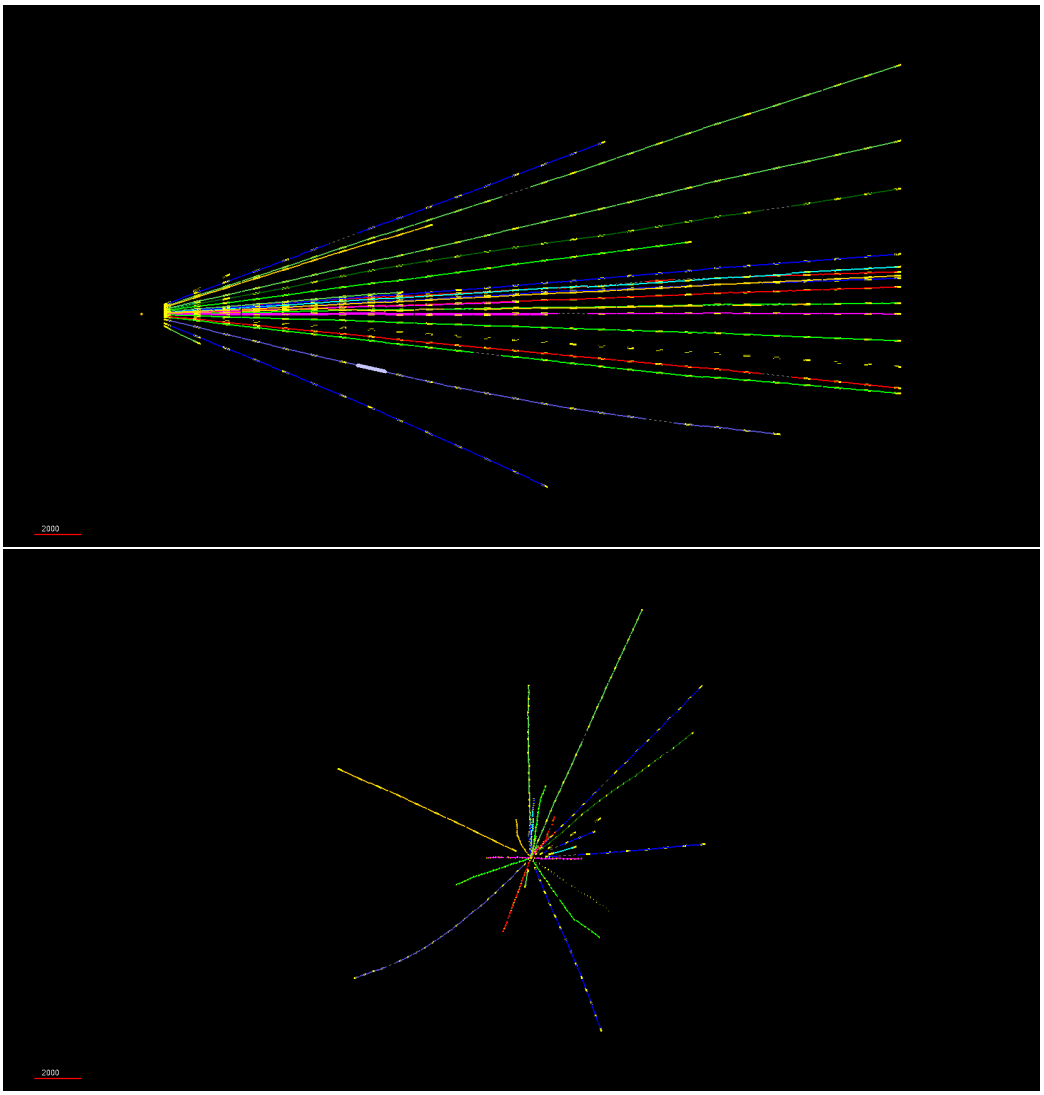

Figure 5.8: 3D vertex display of RUN0 with 29 reconstructed tracks (top) y projection (bottom) z projection.

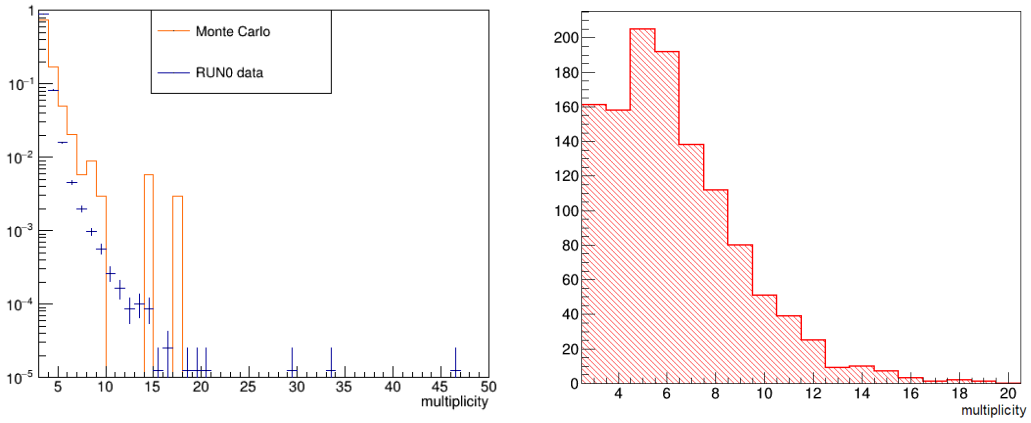

Figure 5.9: Multiplicity of selected vertices. (Left) MC background and RUN0 data are superimposed. (Right) MC signal.

are associated upstream. Five long tracks, two of them going through the end of the sample, emerge from Monte Carlo studies to be the signature of a neutrino CC interaction, producing a charged lepton and the hadronic component. The variables employed to analyze the selected vertices rely on tracks properties as well.

Number of segments Tracks are obtained by fitting segments (base-tracks) in consecutive films. Nevertheless, segments are not required to be consecutive. A maximum of three gaps are allowed to reconstruct a track as one. The left distribution in Figure 5.11 decreases smoothly, both for RUN0 data and MC background, as a consequence of random combinations of low segments reconstructed into tracks.

Number of crossed films The total number of films crossed by track represents the difference between the last and first film of the same track. In the right panel of Figure 5.11 a two-component behaviour become evident, as the long tracks coming from high-energy particles are bound to end in the last plate. Instead, random combination of segments, low energy particles and electromagnetic component lie on the low side of the distribution.

Fill Factor Ad hoc variable defined to normalize the number of segments to the number of films available from the vertex to the end of the brick:

$$\frac{n_{seg}}{n_{pl,ava}}. \tag{5.1}$$

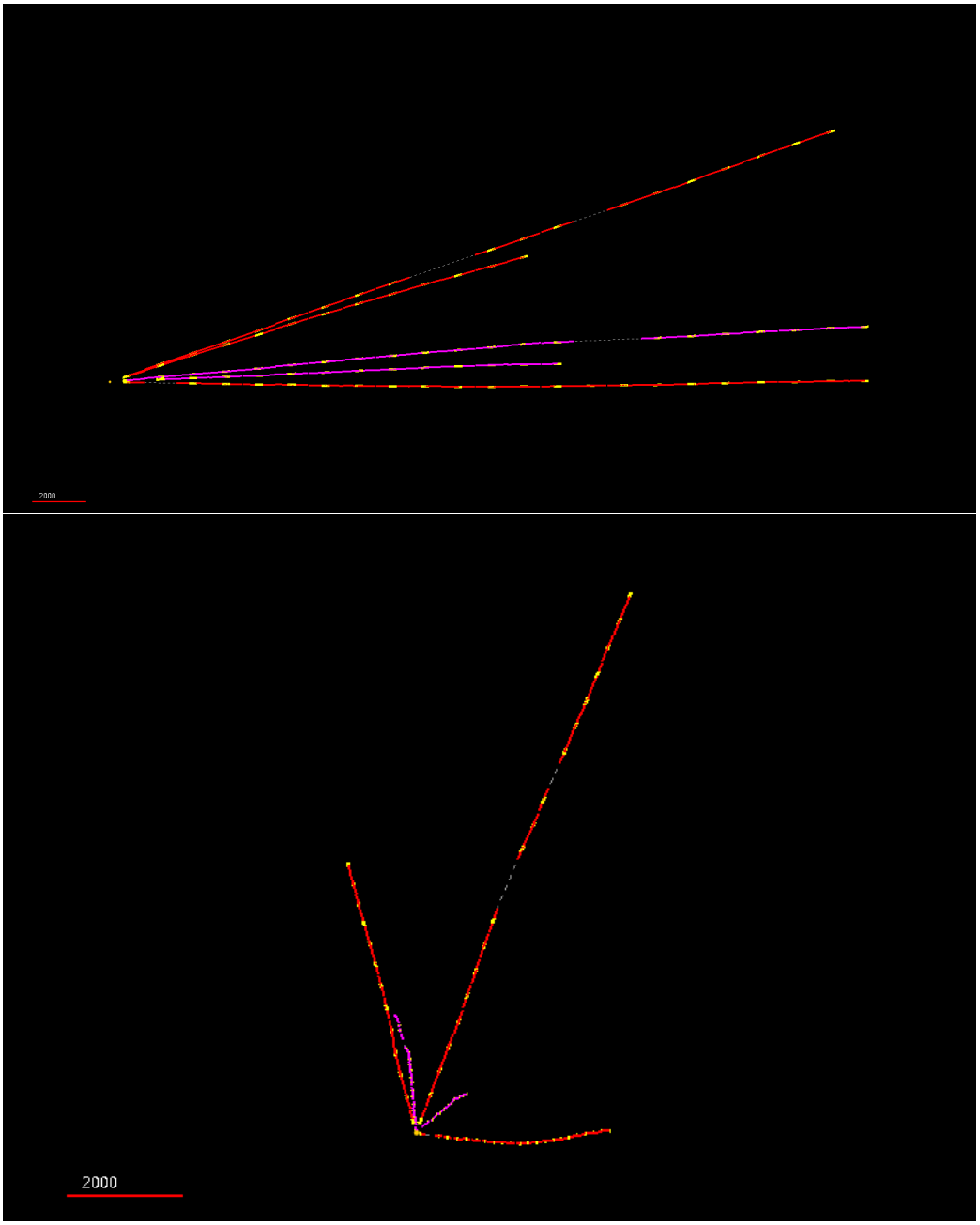

Figure 5.10: 3D vertex display of a RUN0 neutral-like interaction (top) y projection (bottom) z projection.

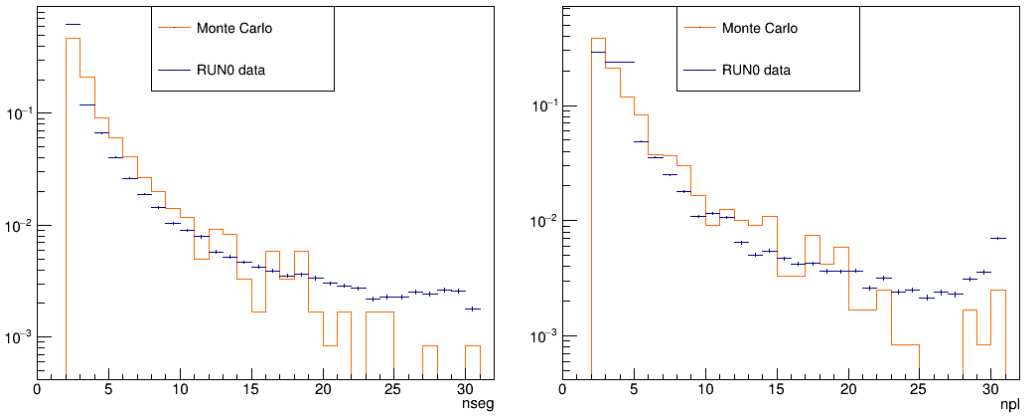

Figure 5.11: (Left) Number of segments reconstructed in each track. (Right) Number of crossed films by each tracks. MC background and RUN0 data are superimposed.

Tracks with fill factor equal to 1 reach the end of the brick with no gaps, whilst lower values are associated with interrupted or absorbed tracks, or a significant number of reconstruction gaps. Fill Factor of RUN0 data and MC background showed in the left panel of Figure 5.12 spreads the values almost uniformly, whereas the FF for MC signal in the right panel is well distributed to high values (> 0.5).

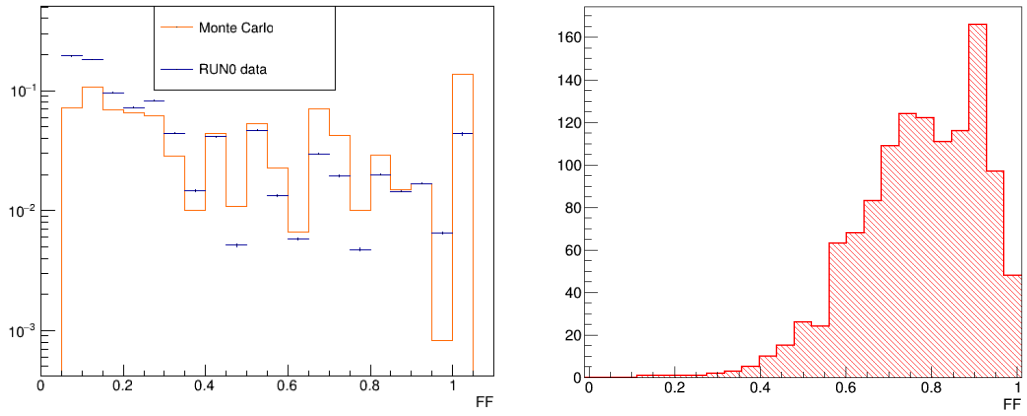

Figure 5.12: Fill Factor evaluated track by track. (Left) MC background and RUN0 data are superimposed. (Right) MC signal.

Impact Parameter The 3D spatial distance between tracks and vertex, evaluated track by track. The left plot of Figure 5.13 shows the data and MC

background impact parameter distributions that softly decrease following equal profiles. The MC signal on the right panel is well peaked below $5\,\mu\mathrm{m}$.

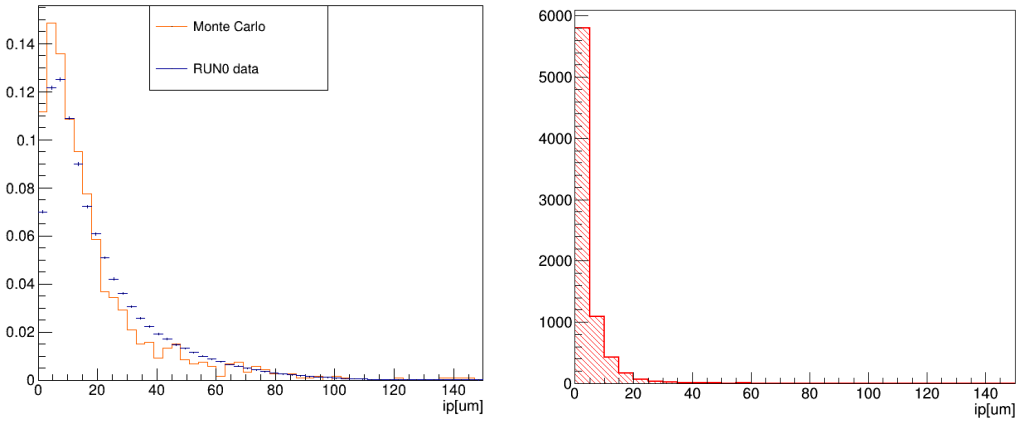

Figure 5.13: Impact parameter evaluated track by track. (Left) MC background and RUN0 data are superimposed. (Right) MC signal.

Vertex probability The probability is defined on the Kalman Filter χ^2, calculated from looping over tracks associated to the vertex, given the covariance matrices of the fitted segments. Random combinations populate the low probability bins in the left panel of Figure 5.14, leaving a small sample made of high-probability reconstructions over a flat distribution. The figure on the right shows the MC signal vertices with reconstructed probability very close to one.

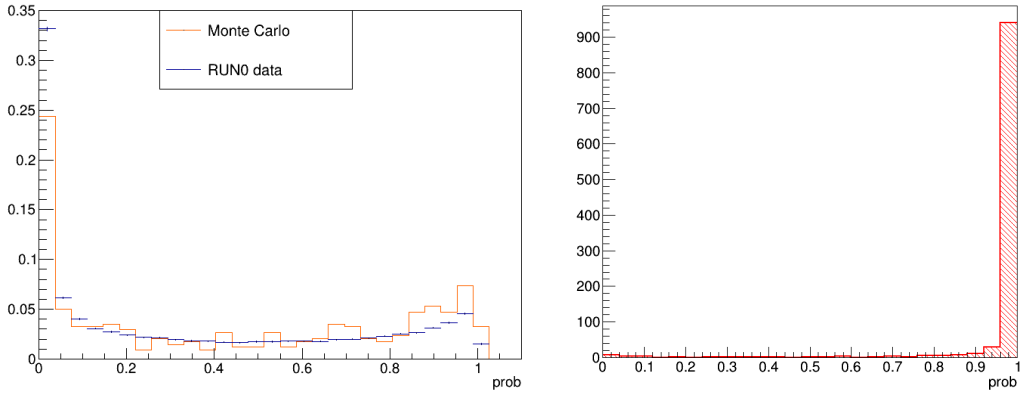

Figure 5.14: Vertex probability. (Left) MC background and RUN0 data are superimposed. (Right) MC signal.

5.3 Multivariate Discrimination with TMVA

The comparison between RUN0 data and Monte Carlo muon background manifested no particular discrepancy in the distributions analyzed individually, thus validating the quality and the characterization of the data as background only. A further step was to view the whole vertex characterization altogether, investigating the possible combinations of cuts that lead to a suitable background rejection. This approach is called *Multivariate Discrimination* or *Multivariate Analysis* (MVA) and it can be conducted exploiting the computer algorithms power with Machine Learning techniques. In applying the MVA to the RUN0 data we aim to reach a significant background suppression, discarding most of the reconstructed events. The vertices left as signal by the MVA could in principle be in-depth analyzed and inspected individually, looking at the displays and studying the topologies.

The Toolkit for Multivariate Analysis (TMVA) [21] provides a ROOT-integrated environment for the processing, evaluation and application of the most frequently adopted multivariate analysis methos in high-energy physics, including artificial neural network and boosted decision trees. The software package consists of object-oriented implementations in C++/ROOT for each of these machine learning techniques, and provides a common interface for the different multivariate methods. Each method is configurable, and all parameters can be tuned. The TMVA provides training, testing and performance evaluation algorithms and visualisation scripts.

5.3.1 Boosted Decision Trees

The MVA classifier chosen as the most suitable for the examined data is the Boosted Decision Tree (BDT). A decision tree is a binary tree structured classifier. A sequence of selection cuts are applied on given variables until a stop criterion is fulfilled. Each cut splits the phase space into nodes, each of which corresponds to a given number of observations classified as signal or as background. The boosting of a decision tree extends this concept from one tree to several trees which form a forest. The trees are derived from the same training ensemble by reweighting events, and are finally combined into a single classifier. The output of the BDT for a given event x is just the weighted average of the scores over the individual trees $T_m(x)$ [14]:

$$T(x) = \sum_{m=1}^{N_{tree}} \alpha_m T_m(x), \tag{5.2}$$

where $T_m(x) = 1$ if the set of variables for the *i-th* event lands that event on a signal leaf and $T_m(x) = -1$ if the set of variables for that event lands it on a

background leaf. The boost weight α_m is derived from the misclassification rate of the previous tree. Boosting stabilizes the response of the decision trees with respect to fluctuations in the training sample and is able to considerably enhance the performance of a single tree.

5.3.2 TMVA training on Monte Carlo

A BDT has been trained with $\sim$ 1200 MC signal ν_μ interaction events and a sample made of $\sim$ 1100 MC muon background. Partition of 70% training and 30% test sample was created. The input variables are shown in Figure 5.15 with the distributions of signal and background given to train the TMVA. After the training, the BDT output of the test sample is reported in Figure 5.16 achieving a strong discrimination of signal and background. Signal and background efficiencies are displayed in the left panel of Figure 5.17, including the signal purity and the significance as well. The optimal cuts are chosen according to the best significance value $S/\sqrt{S+B} = 30.76$, when cutting the BDT output at 0.0149, attaining:

$$\textit{Signal efficiency} = (96.38 \pm 0.01)\,\% \tag{5.3}$$

$$\textit{Background rejection} = (98.193 \pm 0.008)\,\%. \tag{5.4}$$

The ROC curve in the right panel of Figure 5.17 is the best plot to assess the overall discrimination performance. It shows the background rejection versus signal efficiency for the BDT (test sample). The efficiencies are obtained by cutting on the classifier outputs [21].

5.3.3 Background suppression of RUN0 data

Applying the BDT weighted from the MC training to the RUN0 data could help obtain the desired background suppression. Since the expected number of neutrino interaction in the $0.5\,\mathrm{fb}^{-1}$ exposure of RUN0 is less than one, the performance of the classifier are evaluated considering the analyzed sample as only background. As a matter of fact, the BDT output of the RUN0 data reported in Figure 5.18, with only 194 vertices passing the BDT value of 0.0149, achieving a rejection of $(99.757 \pm 0.003)\,\%$. The variables of such vertices are shown in Figure 5.19, prevailing with high Fill Factor and probability and low mean impact parameter.

The two vertices previously displayed in Figure 5.8 and 5.10 pass the selection, respectively with BDT values of 0.072 and 0.131. Another vertex with high BDT response of 0.167 is shown in Figure 5.20. The very similar topology reveals that the described MVA study makes use of input data that is not sufficient to fully discriminate signal from background. Both the variables and

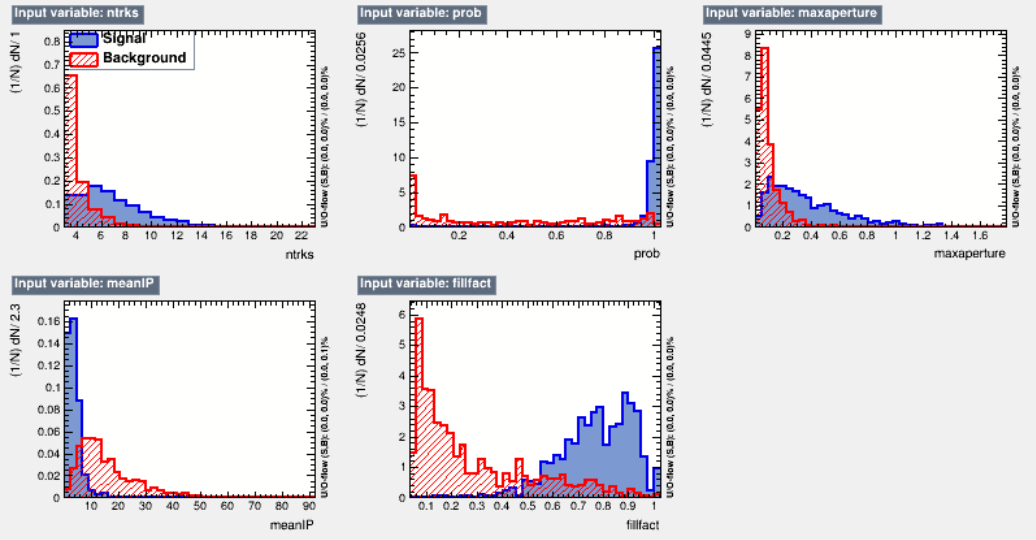

Figure 5.15: Plots of the signal and background MVA input variables (training sample) [21].

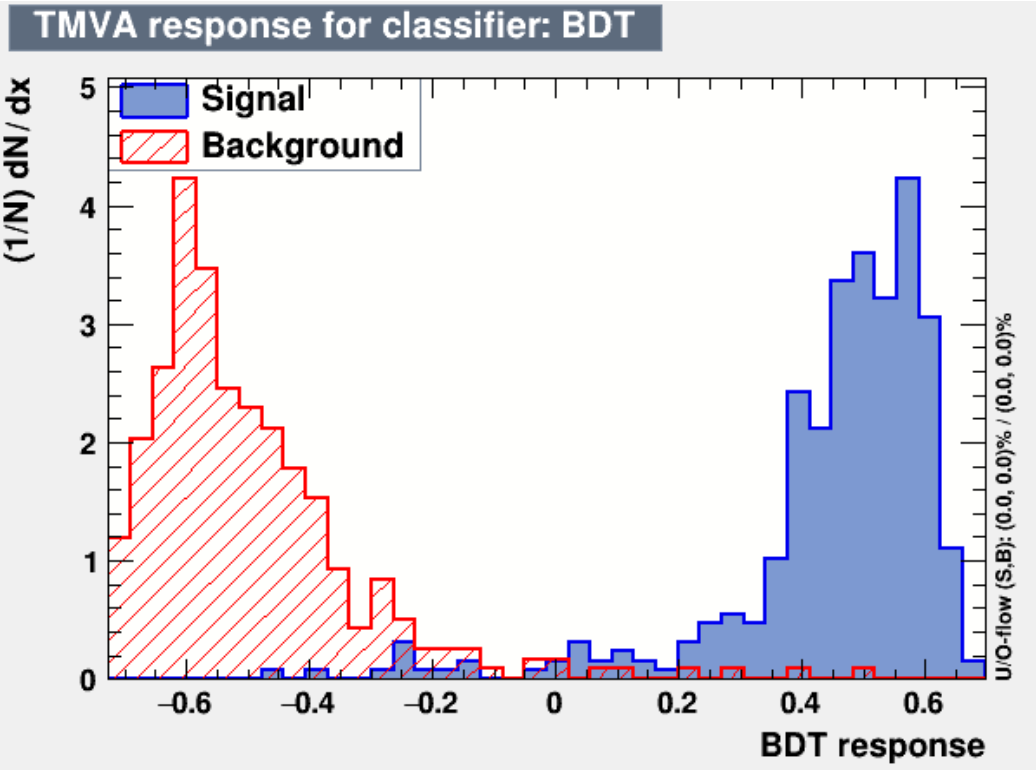

Figure 5.16: BDT response distributions of the test sample for signal and background [21].

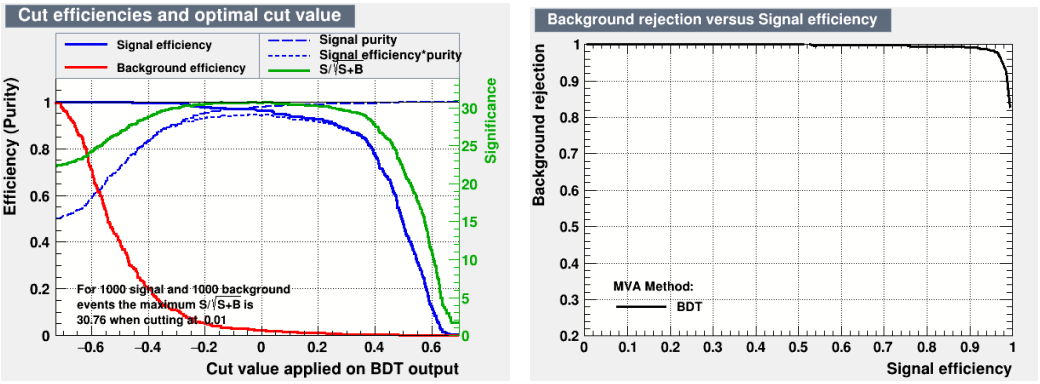

Figure 5.17: (Left) Signal and background efficiencies, obtained from cutting on the classifier outputs, versus the cut value [21]. (Right) BDT ROC curve.

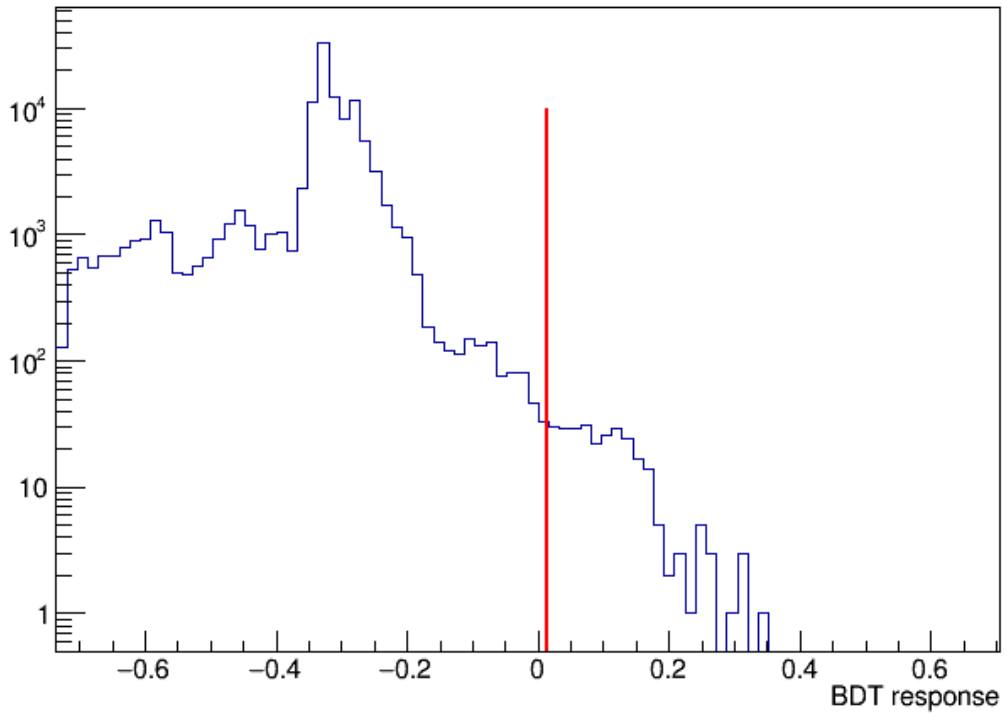

Figure 5.18: BDT response on the RUN0 data. The red line corresponds to the BDT cut.

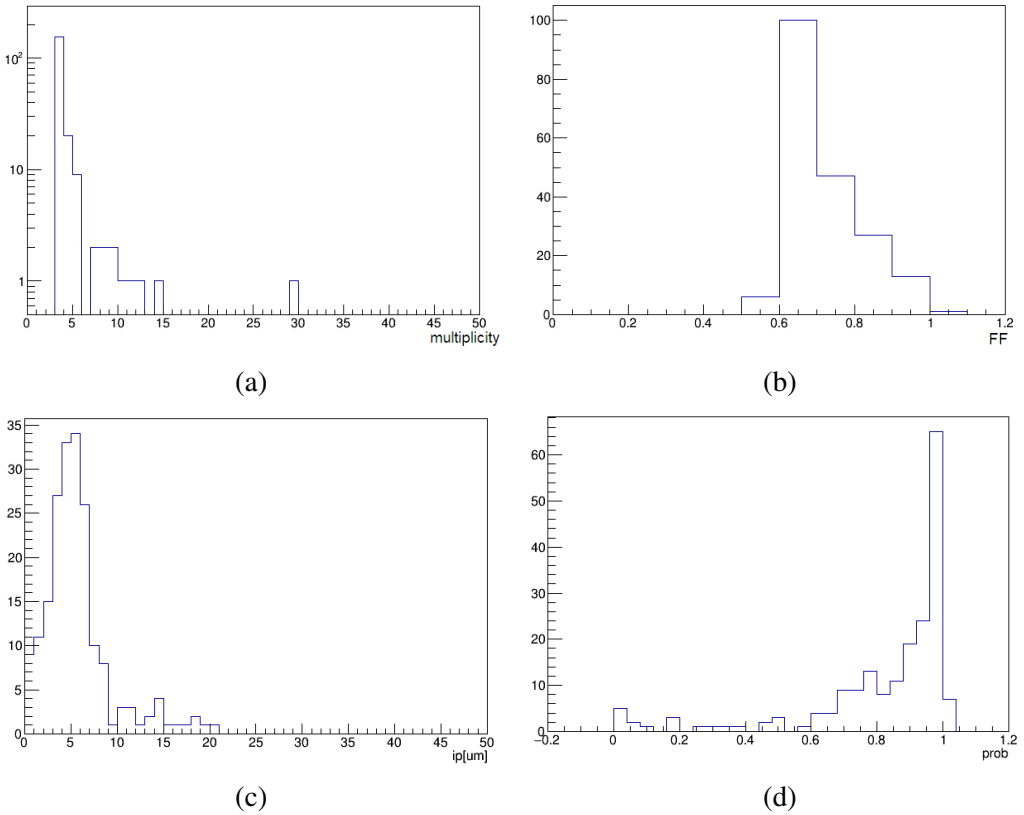

(a) (b)

(c) (d)

Figure 5.19: Distributions of the RUN0 vertices variables passing the BTD cut. Number of tracks (a); fill factor (b); mean impact parameter (c); Kalman Filter probability (d).

the statistics employed to train the BDT might have not been informative enough to distinguish different signatures. A complete reconstruction of the interactions in the target walls, taking into account electromagnetic showers and secondary linked vertices, is needed to fulfill the vertex identification.

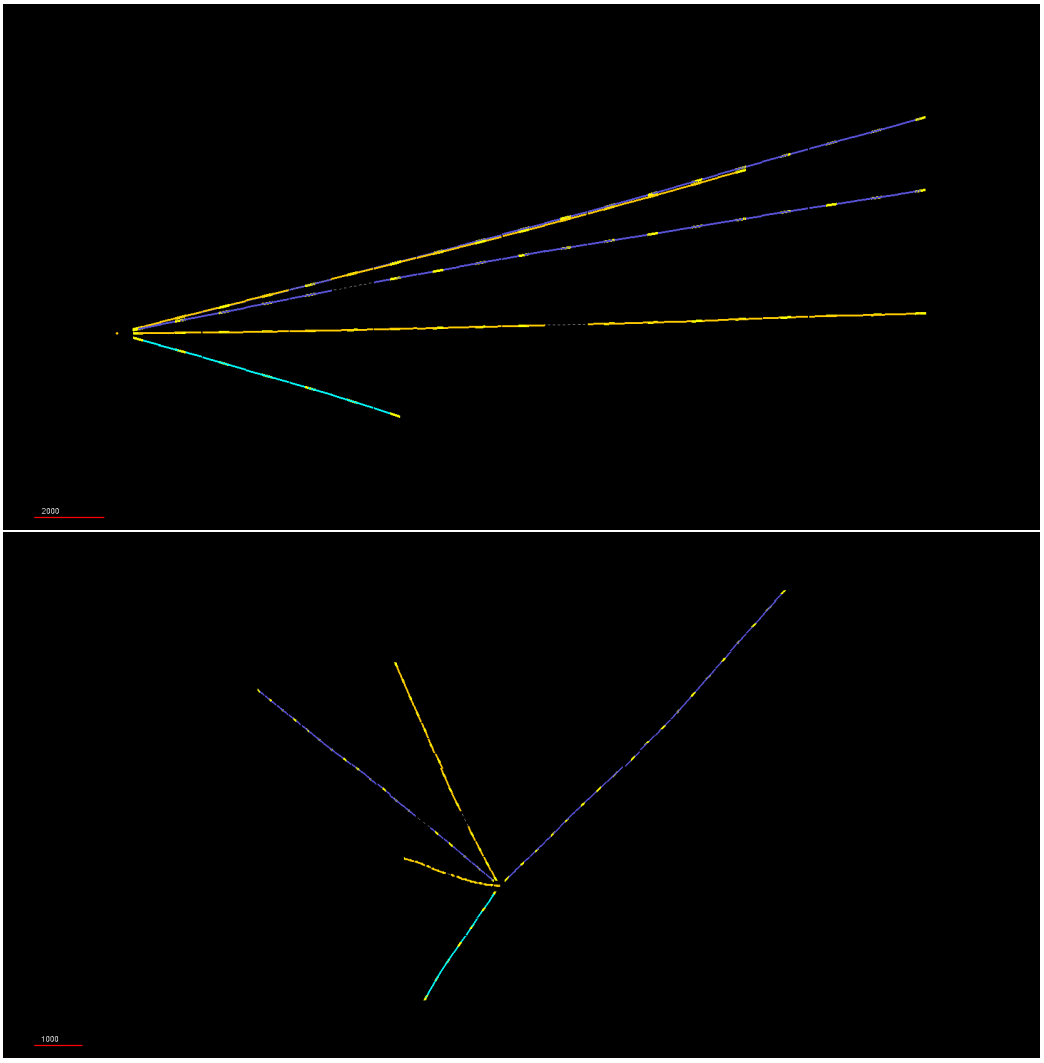

Figure 5.20: 3D vertex display of a neutral-like interaction passing the BDT cut (top) y projection (bottom) z projection.

Chapter 6

Event matching

The SND@LHC detector operates with hybrid technology, combining nuclear emulsion and electronic detectors, as described in Section 2. The target system exploits the micrometric precision of the five ECC walls to reconstruct the neutrino interaction vertex and the SciFi planes to provide the timestamp and the energy measurement of the event. Both detectors are needed to perform a full reconstruction of neutrino candidate events. This become a challenging task given the different nature of the systems: integrate all events in the exposure period, ideally corresponding to $25\,\mathrm{fb}^{-1}$, whereas the electronic detector records data event by event with a DAQ system. After each ECC exposure (emulsion RUNs) and reconstruction it is possible to match the two data types. Matching complexity consists in the association of the two data sets without exploiting the temporal information of the SciFi.

The matching with neutrino vertex candidates reconstructed in the target walls is performed by connecting tracks reconstructed in emulsions with the centre of gravity of electromagnetic and hadronic showers, reconstructed in the SciFi immediately downstream of the ECC where the interaction occurred. The large multiplicity of tracks produced in neutrino interactions and the high density of passing-through muons prevent a track-by-track matching between SciFi and ECC. The emulsion data can also be used to complement the target tracker system for the energy measurement of electromagnetic showers [61].

The strategy to evaluate the center of gravity (or barycenter) for both the SciFi and emulsion data was performed and optimized using Monte Carlo samples made of $\sim$ 3900 ν_μ ($\bar{\nu_\mu}$) and $\sim$ 1200 ν_e ($\bar{\nu_e}$) charged-current interactions in the target walls. The background is not taken into account in this phase of the study. Such requirements were fulfilled by studying the position of the interaction point, the pdg codes of the interacting particles and the mother/daughter relations between them. The simulation has been produced following the standard chain with the official sndsw software:

1. Neutrino fluxes are obtained from FLUKA simulation;
2. Genie generator is used for neutrino interaction simulation;
3. Particle are propagated in the detector with GEANT4;
4. Digitization step to reproduce the data structure.

6.1 SciFi barycenter

An important step in defining the barycenter of a signal event in SciFi was to study of the response of SciFi planes. In doing so, it is necessary to use the MC truth to identify the interaction position. Therefore we can focus on the SciFi plane immediately downstream of the wall where the neutrino interaction occurred. Digitized hits are used to define the barycenter of the signal released by charged particles. The digitization of the signal takes into account the SiPM readout of SciFi planes, coming either from the vertical module or the horizontal one. The two-dimensional distributions of the hits in Figure 6.1 are obtained by considering the fired channels in both directions, thus allowing for ghosts. Hits left by muon neutrino interaction and electron neutrino interaction reveal different signatures. In the right panel of the figure SciFi hits produced by a ν_μ interaction are reported, showing a spread probably due to large angle hadron tracks. Conversely, the right panel of Figure 6.1 illustrates a ν_e interaction event leaving signal in a wider but confined region, as a result of electromagnetic showers.

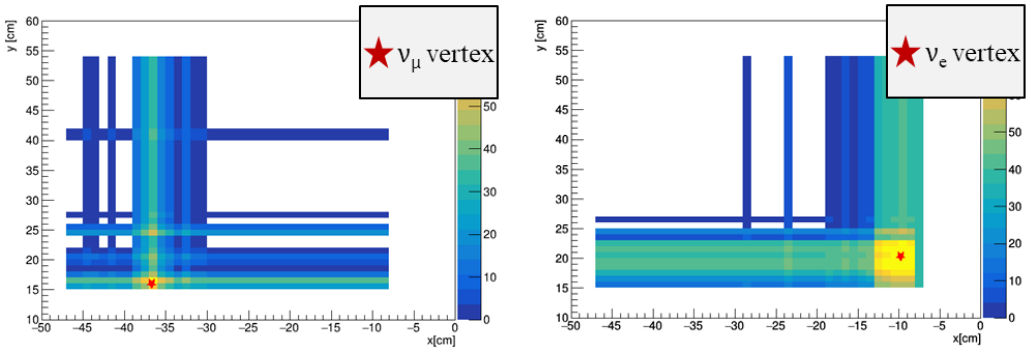

Figure 6.1: 2D map of digitized hits in SciFi. The red star points to the true MC (right) muon and (left) electron neutrino vertex position.

It is therefore more suitable to look separately at the one-dimensional distributions for x and y coordinates in Figure 6.2. The barycenter of SciFi hits is

evaluated as the mean value of the gaussian fit of the hit position in each coordinate.

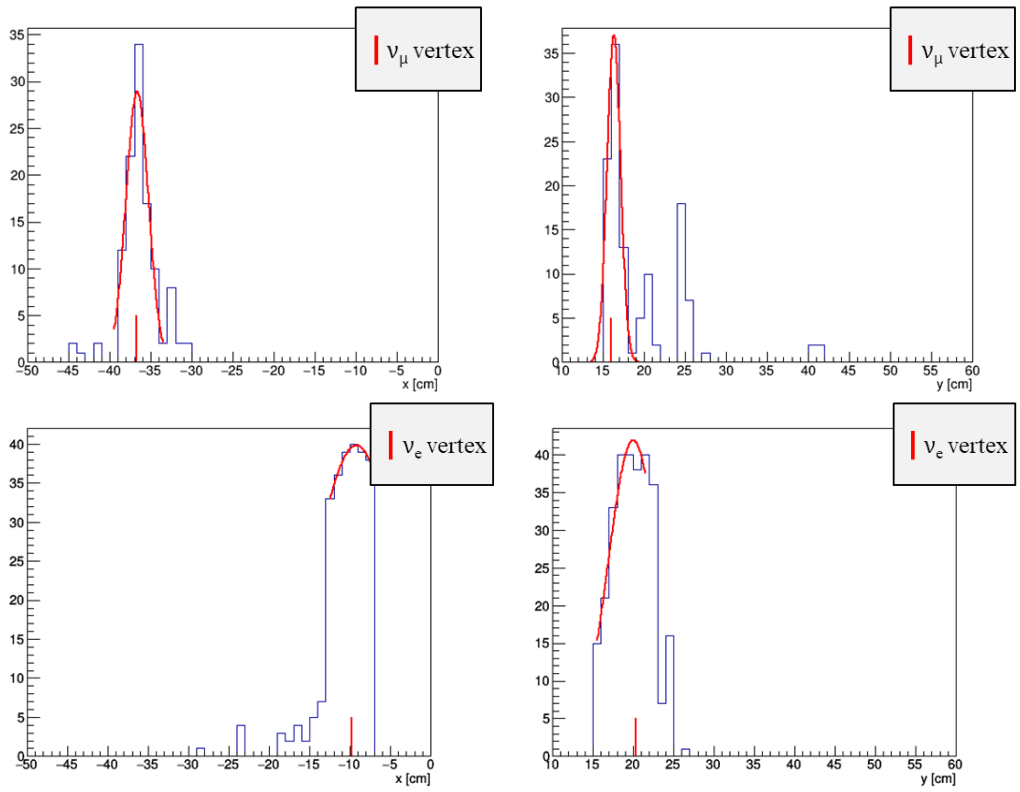

Figure 6.2: Position distributions of digitized hits in SciFi. The red lines indicate the true MC (top) muon and (bottom) electron neutrino vertex position.

A quality check is made by comparing the center of gravity with the true MC neutrino vertex. In order to evaluate the difference between SciFi barycenter position and neutrino vertex position, we need first to perform the projection of the neutrino vertex on the SciFi plane along the incoming neutrino direction, as illustrated in Figure 6.3. The residuals shown in Figure 6.4 and are defined as following:

$$X\ residual = scifi\_bar\_x - nu\_vertex\_x \tag{6.1}$$

$$Y\ residual = scifi\_bar\_x - nu\_vertex\_y, \tag{6.2}$$

where *scifi_bar* and *nu_vertex* indicate the coordinates of the SciFi barycenter and the neutrino vertex, respectively. The distributions are peaked around zero, with widths from gaussian fits of $\sigma_x = 0.530\,\mathrm{cm}$ and $\sigma_y = 0.498\,\mathrm{cm}$. This procedure is also useful to optimize the fits and the determination of the barycenters.

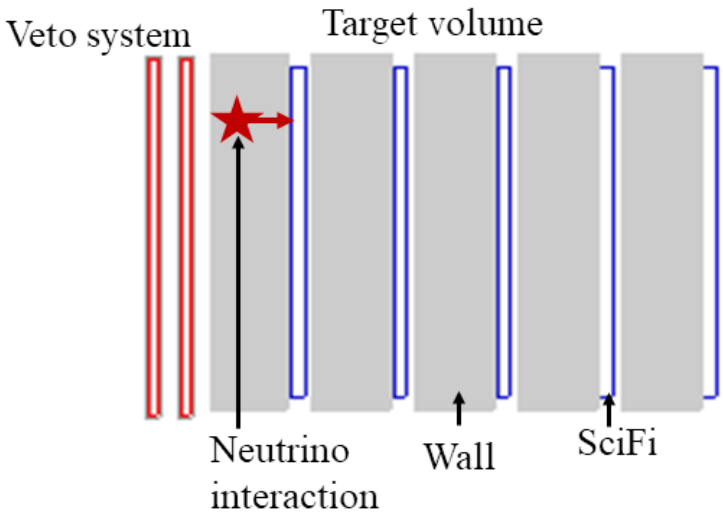

Figure 6.3: Schematic illustration of the prolongation of a neutrino vertex to the downstream SciFi plane.

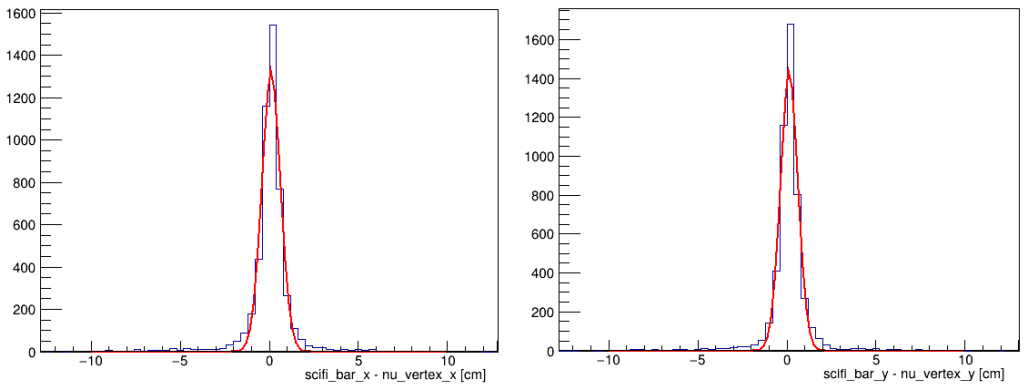

Figure 6.4: Residual distributions for SciFi. Measured barycenters are compared with the true MC neutrino interaction (left) x and (right) y position.

6.2 Emulsion barycenter

The definition of the emulsion barycenter is straightforward. Starting from simulated base-tracks in the target, tracks and vertices are reconstructed within the FEDRA workflow. Each vertex is associated with a MC event ID with an efficiency of $82.4\,\%$, such that ~ 4300 vertices with flag 0 or 3 are reconstructed and analyzed. Tracks coming from the primary vertex are projected on the most downstream emulsion film (60th) as shown in Figure 6.5, in order to be as close as possible to the SciFi plane.

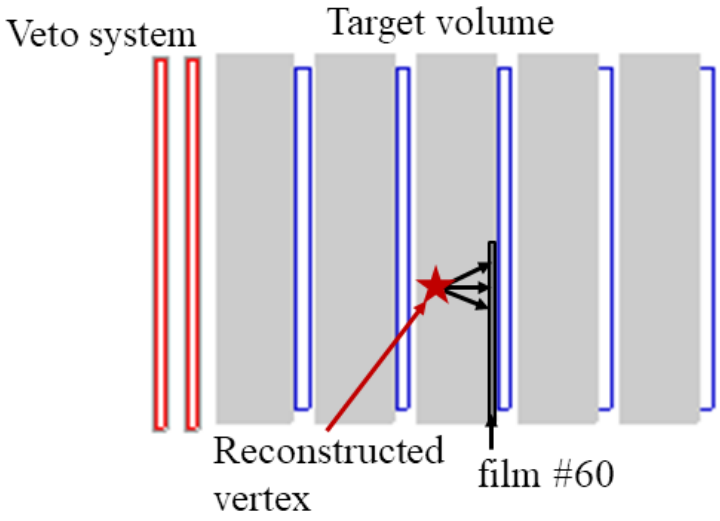

Figure 6.5: Schematic illustration of the prolongation of a reconstructed tracks in the emulsion to the most downstream plate.

On the last emulsion film hits for each projected track are considered, and the barycenter is defined as the center of gravity of the two-dimensional histogram in Figure 6.6. Residual are evaluated as follows:

$$X\ residual = eml\_bar\_x - nu\_vertex\_x \tag{6.3}$$

$$Y\ residual = eml\_bar\_x - nu\_vertex\_y, \tag{6.4}$$

where *eml_bar* indicates the coordinates of the emulsion tracks barycenter and *nu_vertex* the neutrino vertex position. The distributions in Figure 6.7 are peaked at zero, with widths from gaussian fits of $\sigma_x = 0.163\,\mathrm{cm}$ and $\sigma_y = 0.159\,\mathrm{cm}$, revealing the improved precision of the ECC.

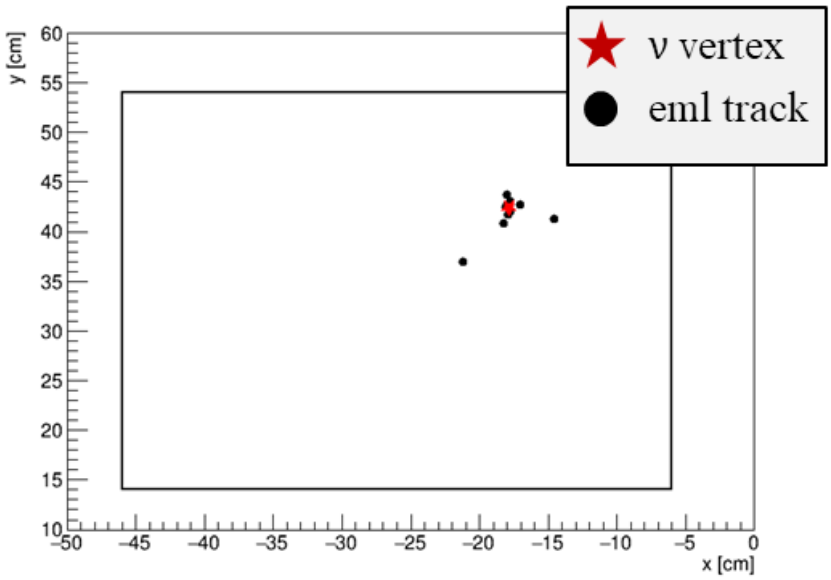

Figure 6.6: 2D position distribution of reconstructed tracks (projectetd) on the last plate. The red star points to the true MC muon neutrino vertex position.

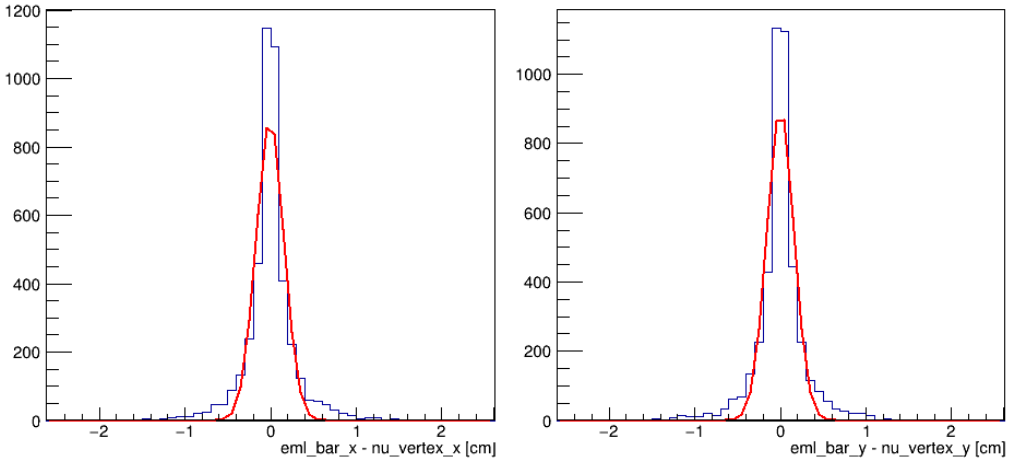

Figure 6.7: Residual distributions for emulsion. Measured barycenters are compared with the true MC neutrino interaction (left) x and (right) y position.

6.3 Matching efficiency

The matching efficiency is assessed by associating an emulsion barycenter with the nearest SciFi barycenter, based on a distance metrics. In order to visualize such a process, in Figure 6.8 ten events are displayed with different colours. In this case the association of the measured barycenter in SciFi and the emulsion tracks center of gravity would be straightforward.

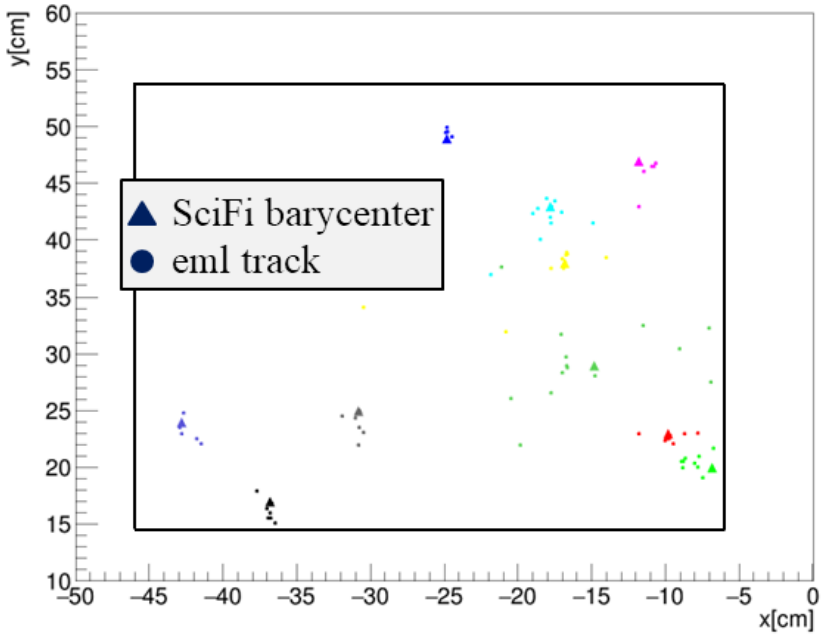

Figure 6.8: Example of 10 events matching. The triangles indicate the event barycenter in Scifi, and the dots represent the track distribution in the last emulsion plate.

Two lists of ordered emulsion events and SciFi events are taken separately, and the fraction of event IDs that are correctly matched is used as an estimate of the efficiency. About ten neutrino interactions are expected in each brick, hence 40 in each wall, assuming a replacement every $25\,\mathrm{fb}^{-1}$. Therefore, barycenters of 10 events at a time are matched, repeating over the full sample. This procedure is done again considering 40 events at a time. The average efficiencies are reported in Table 6.1 distinguishing the neutrino flavour.

This was the first attempt to perform the matching between SciFi digitized hits and neutrino interactions reconstructed in the emulsion target. Despite the early stage of the algorithm and the broad possibilities to improve it the results obtained are however satisfactory. The algorithm is ready to be applied to real data, after the identification of neutrino candidate events. Full event

Flavour	Events	10-set avg eff	40-set avg eff
$\nu_\mu\bar{\nu}_\mu$	3196	92 %	85 %
$\nu_e\bar{\nu}_e$	995	96 %	88 %
TOT	4191	93 %	86 %

Table 6.1: Matching efficiency averaged over sets of 10 and 40 events. Separated values for neutrino flavours are also reported.

reconstruction, taking into account electromagnetic and hadronic showers reconstructed in both sub-detectors, and energy calibration will be implemented to further develop the matching, one of the most challenging task of the SND@LHC experiment in reconstructing the neutrino interactions.

Conclusions

SND@LHC is a compact and stand-alone experiment, designed to perform neutrino measurements of all flavours at the high energies provided by the LHC. The detector is composed of ECC interleaved with electronic trackers, followed downstream by a muon system. The first emulsion target, referred as RUN0, was installed at the beginning of LHC Run 3, integrating a luminosity of $0.5\,\mathrm{fb}^{-1}$.

In the present thesis work the developing of the 2D Event Display for the Collaboration has been accomplished first. Data from 25 emulsion films of RUN0 has been then analyzed in the FEDRA framework, reconstructing the trajectory of muons traversing the target. A density of $(1.5 \pm 0.1) \times 10^4\,\mathrm{fb/cm}^2$ has been measured. This emulsion data is consistent with the independent measurements from the electronic detectors.

Thereafter a vertex reconstruction on the most 31 upstream films of RUN0 data has been performed, studying and inspecting them by means of several described properties. After a selection of the major interest vertices, some 3D displays are presented, showing for the first time interaction vertices in the SND@LHC target. Expecting less than one neutrino event in this first exposure, the analyzed sample was considered as background only. A MVA approach was tested on data, after having trained a BDT with Monte Carlo signal and background samples. As a result, a background suppression of $(99.757 \pm 0.003)\,\%$ was attained.

Lastly, a strategy for the matching of emulsion reconstructed data with the signal from electronic target tracker has been developed. Given the emulsion replacement at every $25\,\mathrm{fb}^{-1}$, a matching efficiency of 93% has been evaluated by associating the centers of gravity of emulsion tracks and digitized electronic hits for ν_μ and ν_e Monte Carlo signal interactions. The algorithm, with further implementations, will be soon tested on real data golden samples.

Bibliography

[1] Alvaro De Rújula and R Rückl. "Neutrino and muon physics in the collider mode of future accelerators". In: (1984). DOI: 10.5170/CERN-1984-010-V-2.571. URL: http://cds.cern.ch/record/1337790.

[2] J. V. Allaby et al. "A precise determination of the electroweak mixing angle from semileptonic neutrino scattering". In: *Zeitschrift für Physik C Particles and Fields* 36.4 (Dec. 1987), pp. 611–628. ISSN: 1431-5858. DOI: 10.1007/BF01630598. URL: https://doi.org/10.1007/BF01630598.

[3] A. Blondel et al. "Electroweak parameters from a high statistics neutrino nucleon scattering experiment". In: *Zeitschrift für Physik C Particles and Fields* 45.3 (Sept. 1990), pp. 361–379. ISSN: 1431-5858. DOI: 10.1007/BF01549665. URL: https://doi.org/10.1007/BF01549665.

[4] A. De Rújula, E. Fernández, and J.J. Gómez-Cadenas. "Neutrino fluxes at future hadron colliders". In: *Nuclear Physics B* 405.1 (1993), pp. 80–108. ISSN: 0550-3213. DOI: https://doi.org/10.1016/0550-3213(93)90427-Q. URL: https://www.sciencedirect.com/science/article/pii/055032139390427Q.

[5] François Vannucci. *Neutrino physics at LHC/SSC*. Tech. rep. Paris: Paris 6. Lab. Phys. Nucl. Théor. Hautes Enérg., 1993. URL: https://cds.cern.ch/record/253670.

[6] Janet M. Conrad, Michael H. Shaevitz, and Tim Bolton. "Precision measurements with high-energy neutrino beams". In: *Rev. Mod. Phys.* 70 (4 Oct. 1998), pp. 1341–1392. DOI: 10.1103/RevModPhys.70.1341. URL: https://link.aps.org/doi/10.1103/RevModPhys.70.1341.

[7] R Brun, F Rademakers, and S Panacek. "ROOT, an object oriented data analysis framework". In: (2000). URL: http://cds.cern.ch/record/491486.

[8] S. Roesler, R. Engel, and J. Ranft. "The Monte Carlo Event Generator DPMJET-III". In: *Advanced Monte Carlo for Radiation Physics, Particle Transport Simulation and Applications*. Springer Berlin Heidelberg, 2001, pp. 1033–1038. DOI: 10.1007/978-3-642-18211-2_166. URL: https://doi.org/10.1007%5C%2F978-3-642-18211-2_166.

[9] S. Agostinelli et al. "Geant4—a simulation toolkit". In: *Nuclear Instruments and Methods in Physics Research Section A: Accelerators, Spectrometers, Detectors and Associated Equipment* 506.3 (2003), pp. 250–303. ISSN: 0168-9002. DOI: https://doi.org/10.1016/S0168-9002(03)01368-8. URL: https://www.sciencedirect.com/science/article/pii/S0168900203013688.

[10] Oliver Sim Brüning et al. *LHC Design Report*. CERN Yellow Reports: Monographs. Geneva: CERN, 2004. DOI: 10.5170/CERN-2004-003-V-1. URL: https://cds.cern.ch/record/782076.

[11] Giovanni De Lellis, Pasquale Migliozzi, and Pietro Santorelli. "Charm physics with neutrinos". In: *Physics Reports* 399.5 (2004), pp. 227–320. ISSN: 0370-1573. DOI: https://doi.org/10.1016/j.physrep.2004.07.005. URL: https://www.sciencedirect.com/science/article/pii/S0370157304002984.

[12] Tanju Gleisberg et al. "SHERPA 1., a proof-of-concept version". In: *Journal of High Energy Physics* 2004.02 (Mar. 2004), p. 056. DOI: 10.1088/1126-6708/2004/02/056. URL: https://dx.doi.org/10.1088/1126-6708/2004/02/056.

[13] N. Armenise et al. "High-speed particle tracking in nuclear emulsion by last-generation automatic microscopes". In: *Nuclear Instruments and Methods in Physics Research Section A: Accelerators, Spectrometers, Detectors and Associated Equipment* 551.2 (2005), pp. 261–270. ISSN: 0168-9002. DOI: https://doi.org/10.1016/j.nima.2005.06.072. URL: https://www.sciencedirect.com/science/article/pii/S0168900205013240.

[14] Byron P. Roe et al. "Boosted decision trees as an alternative to artificial neural networks for particle identification". In: *Nuclear Instruments and Methods in Physics Research Section A: Accelerators, Spectrometers, Detectors and Associated Equipment* 543.2-3 (May 2005), pp. 577–584.

DOI: 10.1016/j.nima.2004.12.018. URL: https://doi.org/10.1016%5C%2Fj.nima.2004.12.018.

[15] L. Arrabito et al. "Hardware performance of a scanning system for high speed analysis of nuclear emulsions". In: *Nuclear Instruments and Methods in Physics Research Section A: Accelerators, Spectrometers, Detectors and Associated Equipment* 568.2 (2006), pp. 578–587. ISSN: 0168-9002. DOI: https://doi.org/10.1016/j.nima.2006.06.072. URL: https://www.sciencedirect.com/science/article/pii/S0168900206012198.

[16] Torbjörn Sjöstrand, Stephen Mrenna, and Peter Skands. "PYTHIA 6.4 physics and manual". In: *Journal of High Energy Physics* 2006.05 (May 2006), p. 026. DOI: 10.1088/1126-6708/2006/05/026. URL: https://dx.doi.org/10.1088/1126-6708/2006/05/026.

[17] V. Tioukov et al. "The FEDRA—Framework for emulsion data reconstruction and analysis in the OPERA experiment". In: *Nuclear Instruments and Methods in Physics Research Section A: Accelerators, Spectrometers, Detectors and Associated Equipment* 559.1 (2006). Proceedings of the X International Workshop on Advanced Computing and Analysis Techniques in Physics Research, pp. 103–105. ISSN: 0168-9002. DOI: https://doi.org/10.1016/j.nima.2005.11.214. URL: https://www.sciencedirect.com/science/article/pii/S0168900205022497.

[18] Stefano Frixione, Paolo Nason, and Carlo Oleari. "Matching NLO QCD computations with parton shower simulations: the POWHEG method". In: *Journal of High Energy Physics* 2007.11 (Nov. 2007), p. 070. DOI: 10.1088/1126-6708/2007/11/070. URL: https://dx.doi.org/10.1088/1126-6708/2007/11/070.

[19] Torbjörn Sjöstrand, Stephen Mrenna, and Peter Skands. "A brief introduction to PYTHIA 8.1". In: *Computer Physics Communications* 178.11 (2008), pp. 852–867. ISSN: 0010-4655. DOI: https://doi.org/10.1016/j.cpc.2008.01.036. URL: https://www.sciencedirect.com/science/article/pii/S0010465508000441.

[20] R Acquafredda et al. "The OPERA experiment in the CERN to Gran Sasso neutrino beam". In: *Journal of Instrumentation* 4.04 (Apr. 2009), P04018. DOI: 10.1088/1748-0221/4/04/P04018. URL: https://dx.doi.org/10.1088/1748-0221/4/04/P04018.

[21] A. Hoecker et al. *TMVA - Toolkit for Multivariate Data Analysis*. 2009. arXiv: physics/0703039 [physics.data-an].

[22] N. Agafonova et al. "Observation of a first candidate event in the OPERA experiment in the CNGS beam". In: *Physics Letters B* 691.3 (2010), pp. 138–145. ISSN: 0370-2693. DOI: https://doi.org/10.1016/j.physletb.2010.06.022. URL: https://www.sciencedirect.com/science/article/pii/S0370269310007537.

[23] C. Andreopoulos et al. "The GENIE neutrino Monte Carlo generator". In: *Nuclear Instruments and Methods in Physics Research Section A: Accelerators, Spectrometers, Detectors and Associated Equipment* 614.1 (2010), pp. 87–104. ISSN: 0168-9002. DOI: https://doi.org/10.1016/j.nima.2009.12.009. URL: https://www.sciencedirect.com/science/article/pii/S0168900209023043.

[24] A Kayis-Topaksu et al. "Measurement of charm production in neutrino charged-current interactions". In: *New Journal of Physics* 13.9 (Sept. 2011), p. 093002. DOI: 10.1088/1367-2630/13/9/093002. URL: https://dx.doi.org/10.1088/1367-2630/13/9/093002.

[25] O. Adriani et al. "Measurement of forward neutral pion transverse momentum spectra for $\sqrt{s} = 7$ TeV proton-proton collisions at the LHC". In: *Phys. Rev. D* 86 (9 Nov. 2012), p. 092001. DOI: 10.1103/PhysRevD.86.092001. URL: https://link.aps.org/doi/10.1103/PhysRevD.86.092001.

[26] J. A. Formaggio and G. P. Zeller. "From eV to EeV: Neutrino cross sections across energy scales". In: *Rev. Mod. Phys.* 84 (3 Sept. 2012), pp. 1307–1341. DOI: 10.1103/RevModPhys.84.1307. URL: https://link.aps.org/doi/10.1103/RevModPhys.84.1307.

[27] M Al-Turany et al. "The FairRoot framework". In: *Journal of Physics: Conference Series* 396.2 (Dec. 2012), p. 022001. DOI: 10.1088/1742-6596/396/2/022001. URL: https://dx.doi.org/10.1088/1742-6596/396/2/022001.

[28] N. Agafonova et al. "Search for $\nu\mu \rightarrow \nu$eoscillations with the OPERA experiment in the CNGS beam". In: *Journal of High Energy Physics* 2013.7 (July 2013), p. 4. ISSN: 1029-8479. DOI: 10.1007/JHEP07(2013)004. URL: https://doi.org/10.1007/JHEP07(2013)004.

[29] Mark Thomson. *Modern Particle Physics*. Cambridge University Press, 2013.

[30] N. Agafonova et al. "Evidence for $\nu_\mu \rightarrow \nu_\tau$ appearance in the CNGS neutrino beam with the OPERA experiment". In: *Phys. Rev. D* 89 (5 Mar. 2014), p. 051102. DOI: 10.1103/PhysRevD.89.051102. URL: https://link.aps.org/doi/10.1103/PhysRevD.89.051102.

[31] N. Agafonova et al. "Procedure for short-lived particle detection in the OPERA experiment and its application to charm decays". In: *The European Physical Journal C* 74.8 (Aug. 2014), p. 2986. ISSN: 1434-6052. DOI: 10.1140/epjc/s10052-014-2986-0. URL: https://doi.org/10.1140/epjc/s10052-014-2986-0.

[32] N. Agafonova et al. "Discovery of τ Neutrino Appearance in the CNGS Neutrino Beam with the OPERA Experiment". In: *Phys. Rev. Lett.* 115 (12 Sept. 2015), p. 121802. DOI: 10.1103/PhysRevLett.115.121802. URL: https://link.aps.org/doi/10.1103/PhysRevLett.115.121802.

[33] A. Alexandrov et al. "A new fast scanning system for the measurement of large angle tracks in nuclear emulsions". In: *Journal of Instrumentation* 10.11 (Nov. 2015), P11006. DOI: 10.1088/1748-0221/10/11/P11006. URL: https://dx.doi.org/10.1088/1748-0221/10/11/P11006.

[34] Giuseppe Battistoni et al. "Overview of the FLUKA code". In: *Annals of Nuclear Energy* 82 (2015). Joint International Conference on Supercomputing in Nuclear Applications and Monte Carlo 2013, SNA + MC 2013. Pluri- and Trans-disciplinarity, Towards New Modeling and Numerical Simulation Paradigms, pp. 10–18. ISSN: 0306-4549. DOI: https://doi.org/10.1016/j.anucene.2014.11.007. URL: https://www.sciencedirect.com/science/article/pii/S0306454914005878.

[35] SHiP Collaboration et al. *A facility to Search for Hidden Particles (SHiP) at the CERN SPS*. 2015. arXiv: 1504.04956 [physics.ins-det].

[36] D. Marfatia, D.W. McKay, and T.J. Weiler. "New physics with ultra-high-energy neutrinos". In: *Physics Letters B* 748 (2015), pp. 113–116. ISSN: 0370-2693. DOI: https://doi.org/10.1016/j.physletb.2015.07.002. URL: https://www.sciencedirect.com/science/article/pii/S0370269315005122.

[37] Sergey Alekhin et al. “A facility to search for hidden particles at the CERN SPS: the SHiP physics case”. In: *Reports on Progress in Physics* 79.12 (Oct. 2016), p. 124201. DOI: 10.1088/0034-4885/79/12/124201. URL: https://dx.doi.org/10.1088/0034-4885/79/12/124201.

[38] A. Alexandrov et al. “A new generation scanning system for the high-speed analysis of nuclear emulsions”. In: *Journal of Instrumentation* 11.06 (June 2016), P06002. DOI: 10.1088/1748-0221/11/06/P06002. URL: https://dx.doi.org/10.1088/1748-0221/11/06/P06002.

[39] Atri Bhattacharya et al. “Prompt atmospheric neutrino fluxes: perturbative QCD models and nuclear effects”. In: *Journal of High Energy Physics* 2016.11 (Nov. 2016), p. 167. ISSN: 1029-8479. DOI: 10.1007/JHEP11(2016)167. URL: https://doi.org/10.1007/JHEP11(2016)167.

[40] The LHCb collaboration. “Measurements of prompt charm production cross-sections in pp collisions at $$ \sqrt{s} = 13$$TeV”. In: *Journal of High Energy Physics* 2016.3 (Mar. 2016), p. 159. ISSN: 1029-8479. DOI: 10.1007/JHEP03(2016)159. URL: https://doi.org/10.1007/JHEP03(2016)159.

[41] Andrey Alexandrov et al. “The Continuous Motion Technique for a New Generation of Scanning Systems”. In: *Scientific Reports* 7.1 (Aug. 2017), p. 7310. ISSN: 2045-2322. DOI: 10.1038/s41598-017-07869-3. URL: https://doi.org/10.1038/s41598-017-07869-3.

[42] Marco Battaglieri et al. *US Cosmic Visions: New Ideas in Dark Matter 2017: Community Report*. 2017. DOI: 10.48550/ARXIV.1707.04591. URL: https://arxiv.org/abs/1707.04591.

[43] The IceCube Collaboration. “Measurement of the multi-TeV neutrino interaction cross-section with IceCube using Earth absorption”. In: *Nature* 551.7682 (Nov. 2017), pp. 596–600. ISSN: 1476-4687. DOI: 10.1038/nature24459. URL: https://doi.org/10.1038/nature24459.

[44] N. Agafonova and Anonymous. “Erratum: Final Results of the OPERA Experiment on ν_τ Appearance in the CNGS Neutrino Beam [Phys. Rev. Lett. 120, 211801 (2018)]”. In: *Phys. Rev. Lett.* 121 (13 Sept. 2018), p. 139901. DOI: 10.1103/PhysRevLett.121.139901. URL: https://link.aps.org/doi/10.1103/PhysRevLett.121.139901.

[45] N. Agafonova et al. "Final results of the search for $\nu\mu \rightarrow \nu$e oscillations with the OPERA detector in the CNGS beam". In: *Journal of High Energy Physics* 2018.6 (June 2018), p. 151. ISSN: 1029-8479. DOI: 10.1007/JHEP06(2018)151. URL: https://doi.org/10.1007/JHEP06(2018)151.

[46] Markus Ackermann et al. "Astrophysics Uniquely Enabled by Observations of High-Energy Cosmic Neutrinos". In: (2019). DOI: 10.48550/ARXIV.1903.04334. URL: https://arxiv.org/abs/1903.04334.

[47] C Ahdida et al. *SHiP Experiment - Progress Report*. Tech. rep. Geneva: CERN, 2019. URL: https://cds.cern.ch/record/2654870.

[48] Andrey Alexandrov, Giovanni De Lellis, and Valeri Tioukov. "A Novel Optical Scanning Technique with an Inclined Focusing Plane". In: *Scientific Reports* 9.1 (Feb. 2019), p. 2870. ISSN: 2045-2322. DOI: 10.1038/s41598-019-39415-8. URL: https://doi.org/10.1038/s41598-019-39415-8.

[49] N Beni et al. "Physics potential of an experiment using LHC neutrinos". In: *Journal of Physics G: Nuclear and Particle Physics* 46.11 (Oct. 2019), p. 115008. DOI: 10.1088/1361-6471/ab3f7c. URL: https://dx.doi.org/10.1088/1361-6471/ab3f7c.

[50] Mauricio Bustamante and Amy Connolly. "Extracting the Energy-Dependent Neutrino-Nucleon Cross Section above 10 TeV Using IceCube Showers". In: *Phys. Rev. Lett.* 122 (4 Jan. 2019), p. 041101. DOI: 10.1103/PhysRevLett.122.041101. URL: https://link.aps.org/doi/10.1103/PhysRevLett.122.041101.

[51] European Strategy For Particle Physics Preparatory Group. *Physics Briefing Book*. 2019. DOI: 10.48550/ARXIV.1910.11775. URL: https://arxiv.org/abs/1910.11775.

[52] Marc Schumann. "Direct detection of WIMP dark matter: concepts and status". In: *Journal of Physics G: Nuclear and Particle Physics* 46.10 (Aug. 2019), p. 103003. DOI: 10.1088/1361-6471/ab2ea5. URL: https://doi.org/10.1088%5C%2F1361-6471%5C%2Fab2ea5.

[53] Henso Abreu et al. "Detecting and studying high-energy collider neutrinos with FASER at the LHC". In: *The European Physical Journal C* 80.1 (Jan. 2020). DOI: 10.1140/epjc/s10052-020-7631-5. URL: https://doi.org/10.1140/epjc/s10052-020-7631-5.

[54] N. Agafonova et al. "First observation of a tau neutrino charged current interaction with charm production in the OPERA experiment". In: *The European Physical Journal C* 80.8 (Aug. 2020), p. 699. ISSN: 1434-6052. DOI: 10.1140/epjc/s10052-020-8160-y. URL: https://doi.org/10.1140/epjc/s10052-020-8160-y.

[55] C A Argüelles et al. "New opportunities at the next-generation neutrino experiments I: BSM neutrino physics and dark matter". In: *Reports on Progress in Physics* 83.12 (Nov. 2020), p. 124201. DOI: 10.1088/1361-6633/ab9d12. URL: https://doi.org/10.1088%5C%2F1361-%5C%2Fab9d12.

[56] Kyrylo Bondarenko et al. "Direct detection and complementary constraints for sub-GeV dark matter". In: *Journal of High Energy Physics* 2020.3 (Mar. 2020). DOI: 10.1007/jhep03(2020)118. URL: https://doi.org/10.1007%5C%2Fjhep03%5C%282020%5C%29118.

[57] SND Collaboration. *Scattering and Neutrino Detector at the LHC*. Tech. rep. Geneva: CERN, 2020. URL: https://cds.cern.ch/record/2729015.

[58] C Ahdida et al. *SND@LHC - Scattering and Neutrino Detector at the LHC*. Tech. rep. Geneva: CERN, 2021. URL: http://cds.cern.ch/record/2750060.

[59] Yu Seon Jeong et al. "Neutrinos from charm: forward production at the LHC and in the atmosphere". In: *PoS* ICRC2021 (2021), p. 1218. DOI: 10.22323/1.395.1218.

[60] Alexey Boyarsky et al. "Searches for new physics at SND@LHC". In: *Journal of High Energy Physics* 2022.3 (Mar. 2022), p. 6. ISSN: 1029-8479. DOI: 10.1007/JHEP03(2022)006. URL: https://doi.org/10.1007/JHEP03(2022)006.

[61] LHC Collaboration. *SND@LHC: The Scattering and Neutrino Detector at the LHC*. 2023. arXiv: 2210.02784 [hep-ex].

[62] SND@LHC Collaboration. "Measurement of the muon flux at SND@LHC". In: (2023).

[63] SND@LHC Collaboration. *SND@LHC: Scattering and Neutrino Detector at the LHC*. [Online; accessed March 25, 2023]. URL: https://snd-lhc.web.cern.ch/detector-gallery.

[64] Hamamatsu. *S14160-3010PS*. [Online; accessed April 4, 2023]. URL: https://www.hamamatsu.com/eu/en/product/optical-sensors/mppc/mppc_mppc-array/S14160-3010PS.html.

[65] Hamamatsu. *S14160-6050HS*. [Online; accessed March 25, 2023]. URL: https://www.hamamatsu.com/eu/en/product/optical-sensors/mppc/mppc_mppc-array/S14160-6050HS.html.

[66] Apache License. *HTCondor Software Suite*. [Online; accessed April 11, 2023]. URL: https://htcondor.org/index.html.

[67] TWiki collaboration platform. *Basic workflow*. [Online; accessed April 17, 2023]. URL: https://twiki.cern.ch/twiki/bin/view/SndLHC/FedraWorkflow.

[68] TWiki collaboration platform. *SND@LHC Luminosity report*. [Online; accessed April 11, 2023]. URL: https://snd-lhc-monitoring.web.cern.ch/luminosity/.

[69] ELJEN TECHNOLOGY. *EJ-200*. [Online; accessed March 25, 2023]. URL: https://eljentechnology.com/products/plastic-scintillators/ej-200-ej-204-ej-208-ej-212.